UNIVERSITY OF CALIFORNIA SAN DIEGO

Tropical-Extratropical Climate Interactions on Seasonal-to-Decadal Timescales

A dissertation submitted in partial satisfaction
of the requirements for the degree
Doctor of Philosophy

in

Oceanography

by

Dillon J. Amaya

Committee in charge:

Arthur J. Miller, Co-Chair
Shang-Ping Xie, Co-Chair
Sarah T. Gille
Joel R. Norris
David G. Victor

2019

The Dissertation of Dillon J. Amaya is approved, and it is acceptable in quality and form for publication on microfilm and electronically:

_____

_____

_____

_____
Co-Chair

_____
Co-Chair

University of California San Diego

2019

DEDICATION

To my parents, who cultivated my curiosities from the beginning.

TABLE OF CONTENTS

LIST OF ABBREVIATIONS

AGCM……...Atmospheric General Circulation Model
AMM……Atlantic Meridional Mode
AMO……Atlantic Multidecadal Oscillation
nATMO……North Pacific Atmosphere-Only
CMIP5……Phase 5 of the Coupled Model Intercomparison Project
CP……...Central Pacific
CTI……Cold Tongue Index
D20……Depth of the 20˚C isotherm
DJF……December, January, February
EC……...Expansion Coefficient
EMCA……Extended Maximum Covariance Analysis
ENSO……...El Niño-Southern Oscillation
EOF……Empirical Orthogonal Function
EP……...Eastern Pacific
EUC……Equatorial Undercurrent
GMST……Global Mean Surface Temperature
GMSST……Global Mean Sea Surface Temperature
ITCZ……Intertropical Convergence Zone
JJA……June, July, August
MAM……March, April, May
MCA……Maximum Covariance Analysis
MMS……Meridional Mass Streamfunction
NAO……North Atlantic Oscillation
NH……...Northern Hemisphere
NPO……North Pacific Oscillation
nPOGA……...North Pacific Ocean Global Atmosphere
P – E……Precipitation minus Evaporation
PC……Principle Component
PDO……Pacific Decadal Oscillation
PMM……Pacific Meridional Mode
RCP……Retrospective Concentration Pathway
SAT……Surface Air Temperature
SDC……Summer Deep Convection
SFM……Seasonal Footprinting Mechanism
SH……Southern Hemisphere
SLP……...Sea Level Pressure
SON……September, October, November
SSH……Sea Surface Height
SST……Sea Surface Temperature
SSTA……Sea Surface Temperature Anomaly
TOA……...Top of the Atmosphere
WES……Wind-Evaporation-SST

LIST OF SYMBOLS

Δt ..... Change in time
ρ ..... Density of sea water
g ..... Gravitational acceleration
Q_{LH} ..... Latent heat flux
ϕ ..... Latitude
ψ ..... Meridional Mass Streamfunction
ψ_{500} ..... Meridional Mass Streamfunction at 500mb
v ..... Meridional wind component
h ..... Ocean mixed-layer depth
R ..... Pearson's correlation coefficient
P ..... Pressure
a ..... Radius of the Earth
α ..... Restoring coefficient
τ ..... Restoring timescale
F ..... Sensible heat flux to the ocean
C_p ..... Specific heat capacity at constant pressure
σ ..... Standard deviation
$t_{0.95}$ ..... t-statistic for a 95% confidence level
U10 ..... Zonal component of the 10m wind
Z_T ..... Zonal mean tropopause height

LIST OF FIGURES

LIST OF TABLES

ACKNOWLEDGEMENTS

My decision to pursue a career in science largely stems from my immense love of learning, my intense curiosity about the world and universe around me, and my desire to constantly challenge and better myself. I foster these traits as a direct result of the unceasing support and incredible patience of my teachers, coaches, and mentors. To Mrs. Fritchie, Mrs. Gray, David Hunt, Brett Jacobs, Suzanne Crews, Brandon Armstrong, Russell Clothier, Cara Satterfield, Don Conlee, and Deborah Thomas: though many of you will never read this dissertation, thank you for always allowing me to ask, "Why?" and "What if?" To Kim Lenger, Chris Adams, and Sonia Garcia: thank you for giving me a voice and for teaching me how to use it. To Philip Howk, Craig Lewis, Corey Lathrom, John Eglich, and Pete Hile: thank you for instilling in me the mental discipline required to see this through.

My committee members, co-authors, and professors were integral in refining the contents of this dissertation and to my graduate education as a whole. To Sarah Gille, Joel Norris, David Victor, Ian Eisenman, Greg Foltz, Mike McPhaden, Nick Siler, Yu Kosaka, Wenyu Zhou, and Yu Zhang: thank you for your thoughtful advice and contributions to my graduate studies.

Over the course of my PhD, my academic advisors have always given me the freedom and opportunity to explore my interests. More importantly, they gave me the chance to struggle and make mistakes. They knew that learning from these errors would be infinitely more valuable to my development than handing me the answer, and I'm a better scientist for it. They have been my biggest advocates and have opened more doors for me than I ever knew existed. To Art and Shang-Ping: thank you for your constant support and for always challenging me to approach science from new and exciting angles. You are both fantastic mentors, and you should be proud of the positive impact you've had on my life and the lives of your other students.

My time in San Diego has largely been defined by the many experiences and memories I've shared with my friends and peers over the years. To Mike DeFlorio, Alan Seltzer, Kate Durkin, Reuben Demirdjian, Bia Villas Bôas, Gui Castelão, Olavo Marques, Momme Hell, Stephen Holleman, Margaret Lindeman, Jacob Morgan, Carrie McIntosh, Mackenzie Elmer, Kim McComas, Julia Dohner, Jenny Miller, Indra McAlpine, John Love, Jim and Terrie Na, Eve Novak, John Crockett, Dave Stegman, Tim Parrot, Neil Malhotra, and many more: thank you, I simply would not have made it through this process without you.

I moved from Kansas City to College Station nearly a decade ago, and then from College Station to San Diego four years later. Each stop along the way has been so full of love and laughter thanks to the lifelong friendships I have been so fortunate to develop. To Mitch Kilpatrick, Cody Kuiper, Amanda Robinson, and Mariel Ruiz: My academic career has prevented me from seeing you more than once or twice a year, but every visit has accentuated your importance in my life. Thank you for making it so easy to pick up where we left off.

My family has been a source of unwavering love and support, and without them I would not have had the confidence to follow my passions. To Mom and Dad: you two have worked harder than anybody I have ever met, and without your sacrifices I would never have had the opportunity to experience this life—thank you. To Jake and Cole: thank you for always keeping me grounded and for always being there for me when I needed it most. Finally, to my incredible fiancée Jessica: thank you for constantly inspiring and motivating me to reach new heights. None of this would have been possible without you.

Chapter 2, in full, is a reprint of the material as it appears in Amaya, D. J., S.-P. Xie, A. J. Miller, and M. J. McPhaden (2015), Seasonality of tropical Pacific decadal trends associated with

the 21st century global warming hiatus, Journal Geophysical Research Oceans. The dissertation author was the primary investigator and author of this paper.

Chapter 3, in full, is a reprint of the material as it appears in Amaya, D. J., N. Siler, S.-P. Xie, and A. J. Miller (2018), The interplay of internal and forced modes of Hadley Cell expansion: lessons from the global warming hiatus, Climate Dynamics. The dissertation author was the primary investigator and author of this paper.

Chapter 4, in full, is a reprint of the material as it appears in Amaya, D. J., M. J. DeFlorio, A. J. Miller, and S.-P. Xie (2017), WES feedback and the Atlantic Meridional Mode: observations and CMIP5 comparisons, Climate Dynamics. The dissertation author was the primary investigator and author of this paper.

Chapter 5, in full, is a reprint of the material as it appears in Amaya D. J., Y. Kosaka, W. Zhou, Y. Zhang, S. P. Xie, and A. J. Miller (2019), The North Pacific pacemaker effect on historical ENSO and its mechanisms, Journal of Climate. The dissertation author was the primary investigator and author of this paper.

VITA

2014	Bachelor of Science in Meteorology, Texas A&M University
2014-2019	Graduate Student Researcher, Scripps Institution of Oceanography
2015	Master of Science in Oceanography, University of California San Diego
2019	Doctor of Philosophy in Oceanography, University of California San Diego

PUBLICATIONS

Amaya D. J., 2019: The Pacific Meridional Mode, a Review. *Curr. Clim. Chang. Rep*., doi:10.1007/s40641-019-00142-x.

Amaya D. J., Y. Kosaka, W. Zhou, Y. Zhang, S.-P. Xie, and A. J. Miller, 2019: The North Pacific pacemaker effect on historical ENSO and its mechanisms. *J. Climate*, https://doi.org/10.1175/JCLI-D-19-0040.1.

Wang, J. K., K. R. Johnson, A. Borsato, **D. J. Amaya**, G. L. Griffiths, G. M. Henderson, S. Frisia, 2019: Hydroclimatic variability in southeast Asia over the last two millennia. *Earth Planet. Sci. Lett*., https://doi.org/10.1016/j.epsl.2019.115737.

Sanchez, S. C., **D. J. Amaya**, A. J. Miller, S.-P. Xie, and C. D. Charles, 2019: Pacific Meridional Mode over the last millennium. *Climate Dyn.,* https://doi.org/10.1007/s00382-019-04740-1.

Amaya, D. J., N. Siler, S.-P. Xie, and A. J. Miller, 2018: The interplay of internal and forced modes of Hadley Cell expansion: lessons from the global warming hiatus. *Climate Dyn.,* 51, 305-319, https://doi.org/10.1007/s00382-017-3921-5.

Amaya, D. J., M. J. DeFlorio, A. J. Miller, and S.-P. Xie, 2017: WES feedback and the Atlantic Meridional Mode: observations and CMIP5 comparisons. *Climate Dyn.,* 49, 1665-1679, https://doi:10.1007/s00382-016-3411-1.

Amaya, D. J., S.-P. Xie, A. J. Miller, and M. J. McPhaden, 2015: Seasonality of tropical Pacific decadal trends associated with the 21st century global warming hiatus. *J. Geophys. Res. Ocean.*, 120, 6782– 6798, https://doi:10.1002/2015JC010906.

Amaya, D. J., and G. R. Foltz, 2014: Impacts of canonical and Modoki El Niño on tropical Atlantic SST. *J. Geophys. Res. Ocean.*, 119, 777–789, doi:10.1002/2013JC009476. http://doi.wiley.com/10.1002/2013JC009476.

Kramm, G., **D. J. Amaya**, T. Foken, and N. Mölders, 2013: Hans A. Panofsky's Integral Similarity Function—At Fifty. *Atmos. Clim. Sci.*, 3, 581–594, doi:10.4236/acs.2013.34061.

ABSTRACT OF THE DISSERTATION

Tropical-Extratropical Climate Interactions on Seasonal-to-Decadal Timescales

by

Dillon J. Amaya

Doctor of Philosophy in Oceanography

University of California San Diego, 2019

Arthur J. Miller, Co-Chair
Shang-Ping Xie, Co-Chair

Decades of research have shown that the accumulation of greenhouse gases in the atmosphere due to anthropogenic emissions strongly influences global and regional climate. However, natural variability associated with intrinsic climate modes introduces substantial noise across myriad timescales, posing a significant challenge for the accurate simulation and projection of future climate variability and change.

In this dissertation, we utilize state-of-the-art climate model simulations in tandem with modern observational data sets to: 1. Investigate the physical mechanisms governing the evolution

of internal climate modes on seasonal-to-decadal timescales, 2. Analyze the impact of those modes on remote climates through ocean-atmosphere teleconnections, and 3. Assess the interplay of internal and forced variability in order to better interpret observed climate trends. We show that the observed cooling of the tropical Pacific Ocean in recent decades primarily stems from a decadal intensification of the equatorial wind-driven ocean circulation during boreal winter. We then provide model evidence that internal variations associated with this decadal cooling superposed with anthropogenic trends to produce a period of accelerated Hadley Cell expansion that strongly mirrors observed trends since 1980.

We also consider the influence of extratropical climate variability on tropical climate. Specifically, we develop a novel statistical technique to isolate the spatiotemporal evolution of the Atlantic Meridional Mode (AMM) in observations. We show that the AMM integrates extratropical atmospheric noise into a deterministic pattern of propagating sea surface temperature (SST), wind, and latent heat flux anomalies. A comparison to CMIP5 reveals that most models tend to poorly simulate the relevant coupled feedbacks. We further explore these mechanisms using a fully-coupled climate model to produce an ensemble of North Pacific SST pacemaker experiments. We find that North Pacific SST has significantly influenced the observed trajectory of observed ENSO variability, particularly the 2014-2015 and 2015-2016 El Niños. These interactions are made possible through two physical pathways that arise from the evolution of the Pacific Meridional Mode (PMM).

The research presented in this dissertation improves understanding of the physical mechanisms controlling key internal climate modes, and takes a significant step towards quantifying tropical-extratropical interactions.

Chapter 1

Introduction

1.1 Motivation

For much of the global population, subtle variations in regional climate can have profound impacts on one's socioeconomic outlook. This is particularly true for the hundreds of millions of people who depend critically on the accurate prediction of surface air temperature and rainfall patterns for water and food. Decades of research have led to the conclusion that the accumulation of greenhouse gases in the atmosphere due to anthropogenic emissions strongly influences global and regional climate (e.g., Hartmann et al. 2013). Therefore, projecting future climate variability and change due to external radiative forcing has been a fundamental driver of scientific inquiry in recent years. However, climate is also characterized by natural "noise" that can be large relative to external anthropogenic "signals". The complicated interplay of internal variability and external forcing presents a significant challenge in projecting future climate change.

While a significant portion of intrinsic variability results from the chaotic and unpredictable nature of the climate system (Shepherd 2014), there exist deterministic components associated with internal climate modes (Deser et al. 2010). Internal climate modes vary across myriad timescales and are defined by recognizable and recurrent patterns in ocean surface temperature and/or atmosphere circulation, often resulting from coupled interactions between the two. Further, these modes can often be represented by dynamical systems, such that their physical evolution includes a predictable component in time and space. Generally, climate modes evolve regionally; however, many of them drive large-scale atmospheric responses or "teleconnections",

which can extend their influence to remote climates throughout the globe. As a result, improving our understanding of the dynamical underpinnings behind climate modes and their teleconnections may significantly enhance the predictability of a wide range of climate impacts.

1.2 Tropical influence on extratropical climate

The influence of tropical climate modes on extratropical climate and weather has been an active area of research since the mid-20th century. Early observational work by Riehl (1950), Bjerknes (1969), and others showed that tropical sea surface temperature (SST) anomalies can drive atmospheric convection, which acts as a thermal source for barotropic and baroclinic circulation anomalies at higher latitudes. Subsequent theory and modeling experiments linked these teleconnections to Rossby wave trains that emanate from a tropical heat source and force surface responses in mid-latitude temperature, wind, and precipitation (Gill 1980; Horel and Wallace 1981; Barnston and Livezey 1987).

A major source of anomalous atmospheric heat in the tropics is the El Niño-Southern Oscillation (ENSO), which is an internal climate mode that dominates tropical Pacific variability on interannual timescales. As will be discussed in the coming chapters, ENSO represents an anomalous warming or cooling of the equatorial Pacific Ocean, which strongly modulates the position of tropical precipitation and influences the mid-latitudes through the aforementioned atmospheric bridge (Horel and Wallace 1981). Low-frequency tropical Pacific climate modes are also thought to significantly impact higher latitudes through a similar mechanism (Newman et al. 2016). The influence of tropical Pacific climate modes on global precipitation and surface air temperature variability on seasonal-to-decadal timescales will be a major focus of this dissertation.

1.3 Extratropical influence on tropical climate

Within the tropics, meridional temperature gradients in the atmosphere are small due to mostly uniform insolation and the large Rossby deformation radius of propagating waves. As a result, tropical atmospheric circulation is weak and SST anomalies are particularly effective at driving an atmospheric response. In comparison, meridional temperature gradients in the mid-latitudes are much sharper, and atmospheric circulation is much more vigorous, making it difficult for ocean anomalies to strongly impact the atmosphere (Alexander and Scott 1997). Therefore, while extratropical climate modes can significantly modulate local climate, their influence on remote climates through atmospheric teleconnections is less clear.

However, over the past two decades, the climate community has identified important physical mechanisms by which extratropical ocean-atmosphere variability can significantly impact tropical climate modes such as ENSO in the Pacific and the Atlantic Niño in the Atlantic. These extratropical-to-tropical pathways primarily develop through the so-called Pacific and Atlantic Meridional Modes (PMM and AMM, respectively), which are modes of coupled climate variability found in the subtropical Pacific and Atlantic Oceans. As will be discussed, the PMM and AMM act as conduits by which stochastic extratropical atmospheric variability can teleconnect into the deep tropics through a series of coupled air-sea interactions (Chiang and Vimont 2004). Their influence is then felt globally through tropically-forced atmospheric teleconnections.

1.4 Dissertation overview

The work in this dissertation utilizes state-of-the-art climate model simulations in tandem with modern observational data sets to investigate the impact of internal climate modes on remote climates on seasonal-to-decadal timescales. The interaction between natural and anthropogenic

climate variability is also analyzed with an emphasis on future projections. The dissertation is organized as follows. In Chapter 2, we assess the seasonality of decadal trends in ocean circulation along the equatorial Pacific strip. This analysis seeks to improve our understanding of the physical drivers behind observed decadal tropical Pacific cooling and the observed seasonality of the recent global warming "hiatus". The results of this work serve as motivation for Chapter 3, which develops a statistical technique to relate observed Hadley Cell expansion to this tropical Pacific cooling. Specifically, we isolate an internal and forced mode of Hadley Cell width variability in coupled climate simulations, and utilize them to assess future changes in regional hydrology.

While Chapters 2 and 3 primarily focus on the influence of tropical climate modes on higher latitudes, Chapters 4 and 5 delve into extratropical-to-tropical teleconnections. In Chapter 4, we develop a novel statistical technique to isolate the physical processes that govern the seasonal evolution of the AMM in observations. We then use these techniques to assess the ability of modern climate models to accurately simulate the relevant coupled air-sea interactions. Finally, in Chapter 5, we use a coupled climate model to generate the first ever ensemble of North Pacific pacemaker simulations. In these experiments, we force the model with the observed trajectory of SST anomalies in the North Pacific, while allowing the model to freely evolve everywhere else. We show that North Pacific-forced ocean-atmosphere interactions can account for ~15-20% of observed ENSO variability since 1950. These interactions are made possible through two distinct physical pathways associated with the PMM.

Chapter 2

Seasonality of tropical Pacific decadal trends associated with the 21st century global warming hiatus

Abstract

Equatorial Pacific changes during the transition from a non-hiatus period (pre-1999) to the present global warming hiatus period (post-1999) are identified using a combination of reanalysis and observed data sets. Results show increased surface wind forcing has excited significant changes in wind-driven circulation. Over the last two decades, the core of the Equatorial Undercurrent intensified at a rate of 6.9 cm s^{-1} $decade^{-1}$. Similarly, equatorial upwelling associated with the shallow meridional overturning circulation increased at a rate of 2.0 x 10^{-4} cm s^{-1} $decade^{-1}$ in the Central Pacific. Further, a seasonal dependence is identified in the sea surface temperature trends and in subsurface dynamics. Seasonal variations are evident in reversals of equatorial surface flow trends, changes in subsurface circulation, and seasonal deepening/shoaling of the thermocline. Anomalous westward surface flow drives cold-water zonal advection from November to February, leading to surface cooling from December through May. Conversely, eastward surface current anomalies in June-July drive warm-water zonal advection producing surface warming from July to November. An improved dynamical understanding of how the tropical Pacific Ocean responds during transitions into hiatus events, including its seasonal structure, may help to improve future predictability of decadal climate variations.

2.1 Overview

Global average surface air temperature (SAT) has been significantly increasing since the industrial revolution (Hartmann et al. 2013), although this overall global warming trend has been punctuated by periods of weaker/stalled warming or cooling. Sometimes lasting several decades, breaks in twentieth century warming have been called global warming "hiatuses" in the literature (e.g., Meehl et al. 2011; Kosaka and Xie 2013; England et al. 2014). This has reignited debate on the validity of anthropogenic climate change among skeptics and confusion among the public.

Examples of hiatuses include a period of time from the 1940s to the 1970s and currently from about 2000 to the present (Figure 2.1a). In particular, the current global warming hiatus has been the subject of significant scientific scrutiny. For example, a growing body of literature has shown increased ocean heat uptake over the last decade (Meehl et al. 2011; Katsman and Oldenborgh 2011; Meehl et al. 2013; Guemas et al. 2013). Yet uncertainty remains on the mechanisms driving the transition from a non-hiatus period to a global warming hiatus period (Solomon et al. 2010, 2011; Kaufmann et al. 2011). Since future hiatus periods are likely to disrupt future warming trends (Easterling and Wehner 2009; Hansen et al. 2011) it is important to ascertain the impact that a hiatus has on the global climate system.

Recent research has focused on the Pacific Ocean as a potential player in modulating global warming trends due to its immense volume (Meehl et al. 2011; Brown et al. 2015; Dai et al. 2015). Specifically, studies have shown periods of hiatus correspond well with negative phases of the Pacific Decadal Oscillation (PDO) (Meehl et al. 2011; Kosaka and Xie 2013; England et al. 2014), an internal mode of climate variability (Mantua et al. 1997; Power et al. 1999; Folland 2002). During a negative (positive) phase, this ENSO-like pattern of climate variability is characterized by cooler (warmer) tropical Pacific sea surface temperatures (SST) and stronger (weaker) trade

winds. The 1990s saw the beginning of an easterly trend in the trade winds and as a result the first decade of the 21st-Century has been dominated by anomalously intense trades, which are normally associated with a negative PDO (Figures 2.1b and 2.1c).

A growing body of research has indicated that a negative phase PDO, which has significant impacts on tropical Pacific SST, heat content, and atmospheric/ocean circulations, forces regional climate anomalies in North America, and is a contributing mechanism to the current global warming hiatus (e.g., Kosaka and Xie 2013; England et al. 2014; McGregor et al. 2014). It remains largely unclear though how the eastern Pacific has remained cool even with increased global radiative forcing.

England et al. (2014) describe an intensification of wind-driven circulation in the tropical Pacific during the hiatus, which would drive increased equatorial upwelling in the central and eastern Pacific, thus sustaining cool SSTs. Additionally, Kosaka and Xie (2013) and Trenberth et al. (2014) show a seasonal dependence in surface variables associated with global "hiatus modes". Here, we focus on the seasonal response of surface climate anomalies and subsurface ocean circulation anomalies in the tropical Pacific to increased wind stress forcing associated with a PDO phase transition into a hiatus period.

Thanks to satellite altimetry, the Argo program, and the Tropical Atmosphere Ocean/Triangle Trans-Ocean Buoy Network (TAO/TRITON) moored buoys in the tropical Pacific, the most recent PDO phase change is perhaps the best-observed decadal climate shift in history. This study utilizes extensive ocean reanalysis and observational data sets to bring further clarity to how tropical Pacific Ocean circulation has responded to strengthening trade winds, how these changes maintain cool SSTs at the surface, and how these responses vary seasonally. Understanding the seasonal variability of the circulation is critical in determining the role that the

Pacific Ocean plays in the current hiatus and would improve predictability of future events. Our analysis aims to shed light on the interplay between surface and subsurface variability in the tropical Pacific Ocean during the period 1990-2009.

In the following section we outline the reanalysis products and observational data used in this study. We then present our results illustrating how tropical Pacific surface and subsurface anomalies have changed in the last two decades. An analysis into the seasonal cycle of these phenomena is then performed, followed by a summary and discussion of our results in the context of tropical Pacific climate variability and the current global warming hiatus.

2.2 Data and methods

2.2.1 Reanalysis products and observational data

In the past decade, there has been a growing interest in using ocean syntheses (model dynamics coupled with sparse observational data to produce a complete ocean description) to improve our understanding of decadal climate variability and our ability to predict climate on decadal time scales (e.g., Smith et al. 2007; Keenlyside et al. 2008; Pohlmann et al. 2009; Köhl 2015). Of the variety of methods utilized to assimilate observed data into global ocean models, the adjoint method provides a description of the ocean circulation that exactly obeys the model equations for dynamical principles (Wunsch and Heimbach 2006). Reanalysis products that employ this assimilation method are therefore valuable for research in the dynamics of decadal climate variability.

We use the second German contribution to Estimating the Circulation and Climate of the Ocean system (GECCO2), a reanalysis product that runs from 1948 to 2011 (iteration 28) and is based on the Massachusetts Institute of Technology general circulation model (Marshall et al.

1997). This reanalysis product utilizes a 4D-var, adjoint method of data assimilation that improves upon its predecessor (GECCO) by featuring higher horizontal and vertical resolution and additional physics (Köhl 2015). GECCO2 was forced twice per day by the National Center for Environmental Prediction climatology for the entire run. Additionally, satellite measured monthly mean wind stress fields were included beginning in the early 1990's (Köhl and Stammer 2008). The native output grid is 1/3˚ with meridional refinement near the equator and 1˚ zonal spacing; however, the data have been linearly interpolated to a 1˚x1˚ for ease in processing. All figures derived from the GECCO2 data use this interpolated grid with the exception of Figure 2.8. We use GECCO2 products for SST, sea surface height (SSH), and zonal and meridional components of wind stress/currents. Model heat budget terms for GECCO2 were not saved or made available to the public. Therefore, we estimated zonal temperature advection using finite differencing of monthly means. Additionally, SAT was taken from the Goddard Institute for Space Studies Temperature Analysis (GISSTEMP) (Hansen et al. 2006, 2010). GISSTEMP is available from 1880-present and uses the base period 1951-1980 to calculate anomalies. Finally, the PDO Index was taken from the National Climatic Data Center, which is available from 1854-present.

To determine the robustness of our findings, we compared all GECCO2 derived results with National Oceanic and Atmospheric Administration's Extended Reconstructed Sea Surface Temperatures Version 3b (ERSST), which is available on a 2˚x2˚ grid from 1854-present (Smith et al. 2008). We also compared our findings with SST, zonal wind stress, and ADCP zonal current velocity observations taken by the TAO/TRITON moorings at 5˚S-5˚N, 147˚E-95˚W (McPhaden et al. 1998). It is important to note that TAO/TRITON temperature profiles were among the observational data sets assimilated into GECCO2 (Köhl and Stammer 2008); however, a 30-year 4D-var assimilation may not necessarily reproduce SST accurately. Therefore, we include our

results using TAO/TRITON measurements. In our comparisons, GECCO2 data were resampled to be temporally and spatially consistent with a given TAO/TRITON product. With the exception of Figure 2.1a, all figures were generated using GECCO2 data unless otherwise specified in the figure title.

2.2.2 Trend analysis

Our analysis period for this study is from January 1990 to December 2009. All anomalies and trends are calculated for GECCO2 variables relative to the 1980-2009 climatology. To estimate trends in our data we use a simple linear regression technique. In Section 2.3.1, we report the slope of the linear fit for the 20-year analysis period at each grid point in units per decade (Figures 2.1, 2.4 insert, 2.5b, 2.6b, and 2.6d). In Section 2.3.2, time/longitude plots are generated by linearly regressing a time series of each calendar month over the 20-year period (i.e., collect all Januaries from 1990-2009 and linearly regress). The slope of the linear fit is then reported for each calendar month at each longitude (Figures 2.7, 2.8, 2.11, and 2.12). In these figures, we limit trends in surface wind stress and surface currents to only the zonal component because it dominates the overall trend in the vector fields (not shown).

Seasonal subsurface trends in temperature and current velocities are calculated by collecting all occurrences of December-March and July-November and linearly regressing from 1990-2009. The slopes are then reported for each depth, latitude/longitude (Figures 2.9 and 2.10). Statistical significance for trends was determined using the Mann-Kendall test (Bevan and Kendall 2006), which tests the null hypothesis of trend absence in a time series against the alternative of trend. The Mann-Kendall test has the added benefit of being less affected by outliers sometimes contained in observations. If a Student's *t* test is applied to the same data, our results do not change.

2.3 Results

2.3.1 Surface and subsurface trends

Figure 2.1a shows SAT anomalies averaged globally, while Figure 2.1b depicts area averaged zonal wind stress anomalies in the equatorial Pacific Ocean. Although there is an overall warming trend in SAT anomalies, there are two major periods of hiatus from about 1940 to the mid-1970s and from about 2000 to the present. Interestingly, the former exhibits a slight cooling trend from 1940-1970 while the latter is associated with no apparent trend. When compared to Figure 2.1b, the most recent hiatus corresponds closely to a general strengthening of easterly wind anomalies in the equatorial Pacific. This easterly trend seems to begin well before the present hiatus period sometime around 1993. Conversely, the 1940-1970 hiatus is characterized by a general westerly trend in the wind stress that extends from about 1950-1970.

It is therefore apparent that not only do the two hiatuses described above exhibit slightly different SAT trends, they also occur during opposite trends in equatorial Pacific wind stress. While the slowdown of radiative forcing is an important cause of the 1940s-1970s warming hiatus (e.g., Solomon et al. 2011), the PDO plays an important role in the current hiatus (Marotzke and Forster 2015). Determining the mechanisms that drive the different SAT characteristics of hiatus periods is a complicated matter involving globally coupled ocean-atmosphere interactions and is an active area of research beyond the scope of this study. The background trends in the wind stress, however, correlate well with PDO phase transitions in the mid-to-late 1970s and again in the mid-to-late 1990s. By correlating the PDO Index with the zonal wind stress time series we get a correlation coefficient of 0.48. Thus, strong easterly winds and periods of hiatus tend be associated with negative phases of the PDO, which is consistent with previous studies (e.g., Kosaka and Xie

2013; England et al. 2014). The remainder of the results will attempt to describe the 1990s PDO phase transition from a non-hiatus (positive PDO) period into the resulting hiatus (negative PDO) period in the context of this background strengthening of easterly wind stress and the resulting impact on the equatorial Pacific surface and subsurface.

Figure 2.2 depicts the 1990-2009 trends in SST and surface wind stress in the tropical Pacific. Stippling indicates the SST trend is significant at the 95% for a Mann-Kendall test. The wind stress trend vector is only plotted where the zonal and meridional component are both statistically significant at 95%. As anticipated by Figure 2.1b, there are easterly trends throughout much of the central tropical Pacific associated with a phase transition from a positive PDO in the 1990s to a negative PDO in the 2000s. Similarly, the SST trends reflect this phase transition with largely negative trends along the equatorial strip.

Figure 2.3a shows how the Pacific cold-tongue has varied during the transition to the present hiatus period. This is accomplished by averaging monthly SST anomalies 5˚S-5˚N over the basin from 1990-2010 and plotting them as a time/longitude plot. Over this time period the edge of the equatorial cold-tongue (outlined by the 27.5˚C isotherm) has shifted westward by 20.2 degrees of longitude in response to the increased zonal wind stress, which is significant at 99% for a Mann-Kendall test (Figure 2.3a). Intensified trade winds would lead to an anomalous build-up of SSH in the west equatorial Pacific warm pool region (Figure 2.3b) (e.g., Merrifield et al. 2012). The SSH build up is associated with a deepened thermocline. We estimated the depth of the thermocline as the depth of the 20˚C isotherm and averaged over 5˚S-5˚N, 140˚E-180˚W (purple box, Figure 2.4). A monthly time series of this area average shows the thermocline has been anomalously depressed over the west equatorial Pacific by 22.8 m over the 20-year period as estimated by linear regression. Averaging over 5˚S-5˚N, 170˚W-130˚W in the central basin (red

box, Figure 2.4), there is an anomalous shoaling of less than a meter over the 20-year period. While the thermocline shoaling in the Central Pacific is not significant, the thermocline deepening in the western is significant at 99%. We then use the zonal gradient in the depth of the thermocline to estimate the zonal subsurface pressure gradient along the western and central equatorial strip. By taking the difference of the purple box and the red box in Figure 2.4, we show an upward trend in the zonal gradient that is significant at 99% for a Mann-Kendall test. This would suggest that even though the shoaling trend in the Central Pacific is small, the deepening in the western Pacific is strong enough to significantly intensify the zonal subsurface pressure gradient. Similar trends are evident in the 20˚C depth based only on observations between the first decade of the 21st century relative to the 1980s and 1990s (e.g., McPhaden et al. 2011).

To better observe how trends in the zonal gradient of the thermocline along the equator have impacted subsurface currents and heat content, the linear trends from 1990-2009 in subsurface temperatures and the zonal, meridional, and vertical components of the current velocity (U, V and W respectively) were calculated and reported at each grid point (Figures 2.5b, 2.6b, and 2.6d). Stippling and the plotted current vectors represent significance at 95% for the subsurface temperature trends current velocity trends. Climatological cross-sections are included in Figures 2.5a, 2.6a, and 2.6c for reference.

Longitude/depth cross-sections of the equatorial Pacific are characterized by strong, climatological westward flow from 5-20m and even stronger return flow eastward in the form of the Equatorial Undercurrent (EUC) at around 125-175 m (Figure 2.5a). In Figure 2.5b, there is a pool of warming temperature trends seemingly “trapped” at 75m-200m at 140˚E-170˚W, while a La Niña-like pattern of decreasing SST trends dominates the cross-section from the surface to about 85m in the central/east regions. The mixed layer cooling in the Central Pacific (165˚E-

150˚W) overrides the subsurface warming, and coincides with strong westward surface flow trends. These structures are consistent with intensified westward advection of cold water. Additionally, the subsurface warming in the western Pacific (Figure 2.5b) is consistent with a similar heat anomaly described by (England et al. 2014) in a numerical simulation of the ocean driven by observed surface winds.

The cooling trends in the central and eastern equatorial Pacific surface waters are indicative of a shoaling thermocline, while the warming trends in the western subsurface indicate thermocline deepening. This is consistent with the increasing trend observed in the zonal gradient of the thermocline (Figure 2.4). Significant strengthening in the zonal slope of the thermocline would lead to anomalous subsurface pressure gradients that accelerate the EUC from about 170˚E to 140˚W over the 20-year period (Figure 2.5b). The core of the climatological EUC is found around 85-127m, 150˚W-130˚W and has an average magnitude of 37 cm s^{-1} in the reanalysis (Figure 2.5a). The most significant trends in the zonal component of the subsurface currents lie further west and are deeper around 105-155m, 180˚-160˚W and have an average magnitude of 6.9 cm s^{-1} $decade^{-1}$ (Figure 2.5b). GECCO2 underestimates the strength of the observed zonal current in the background state (e.g., Johnson et al. 2002), but the linear trend estimated from GECCO2 is similar to that observed by TAO/TRITON moored buoys for the same period (see Figure 2.13).

To investigate the cross-equatorial structure, Figure 2.6 describes latitude/depth cross-sections in the Central and West Pacific (180˚-120˚W and 140˚E-180˚ respectively). In the Central Pacific, the average climatological rate of upwelling on the equator is 1.3 x 10^{-3} cm s^{-1} and occurs between 50-85m, while the most significant upwelling trends occur at the same depths and have an average value of 2.0 x 10^{-4} cm s^{-1} $decade^{-1}$ (Figures 2.6a and 2.6b). This upwelling trend

integrated from 170˚-120˚W and 0.5˚S-0.5˚N produces a volume transport trend of 11.1 Sv decade^{-1} from 1990-2009, which is in good agreement with the 9 Sv change in vertical transport across the late 90s transition from a positive to negative PDO reported by (McPhaden and Zhang 2004). Increased upwelling could therefore be contributing to the cooling trends observed in the mixed layer and at the surface in Figures 2.2 and 2.5b.

In the West Pacific climatological cross-section, the currents right on and just south of the equator are dominated by northward flow from 45-200m (Figure 2.6c). In Figure 2.6d these currents are significantly intensified by about 0.92 cm s^{-1} decade^{-1} from 1990-2009 just south of and on the equator. There appears to be a stronger Southern Hemisphere component (5˚S-10˚S) to the warming subsurface trends observed in Figure 2.5b. Additionally, these temperature trends seem to roughly line up with the strongest intensifying trends of the subducting branch of the meridional overturning circulations, which can be found at around between 15˚S-5˚S in the Central Pacific (Figure 2.6b) and between 4˚S and the equator in the western Pacific (Figure 2.6d). Combined with the increased equatorward flow, this enhanced subduction may imply the presence of enhanced meridional temperature advection seen in previous studies (e.g., England et al. 2014; Yang et al. 2014).

2.3.2 Seasonality and observational comparison

To better understand how the above results vary seasonally, a series of time/longitude plots were generated. Figure 2.7a shows trends in SST and the zonal wind stress for each calendar month for 1990-2009 averaged over 2.5˚S-2.5˚N and from 140˚E-80˚W. Figures 2.7b and 2.7c show trends in SSH and the depth of the 20˚C isotherm respectively (D20), both with the same trend in zonal surface current overlaid and averaged over the same latitude intervals. The convention for

D20 trends is such that positive values represent a deepening trend and negative values represent a shoaling trend. The dark gray stippling indicates trend significance at 90%, while light gray represents 80% significance. For the zonal wind stress and zonal surface current trends, the black vectors represent 90% significance and light gray vectors are 80% significance. We limit trends in surface wind stress and surface currents to only the zonal component because it dominates the overall trend in the vector fields (not shown). To the left of each time/longitude section the corresponding seasonal cycle of the wind stress/current trends averaged from 160˚E-150˚W is plotted in blue, while the mean 1990-2009 means seasonal cycle in the same box for the respective variable is in green.

In Figure 2.7a, the decreasing trend observed in Figure 2.2 is most pronounced from December-May (DJFMAM) while weak cooling or warming trends are found from June-November, (JJASON). This result is consistent with studies by Kosaka and Xie (2013) and Trenberth et al. (2014). There is evidence that the SST trends are responding to an enhancement of the mean seasonal cycle of the zonal wind stress as indicated by the significant easterly wind stress trends (blue line) during NDJFMA, which is typically a time of relatively strong climatological easterly flow (green line). Additionally, the easterly wind stress trends are weakest in MJJASO when the mean trades are also at their weakest (Figure 2.7a, side panel). The relationship described above for wind stress trends holds most consistently for the Central Pacific, while the trend in the seasonal SST cycle holds from 160˚E-90˚W.

Surface currents near the equator are primarily driven by the wind stress, as the Coriolis force is very small. An enhancement of the seasonal cycle of the wind stress should therefore correspond to an enhancement in the seasonal cycle of surface currents and zonal temperature advection (Figures 2.7b, 2.7c, and 2.8). Trends in SSH reflect the weakening and strengthening of

the zonal wind stress as water is piled up in the west during DJFMAM and is allowed to slosh back during JJASON (Figure 2.7b). The surface currents also respond to the waxing and waning of the wind stress. Strong westward/eastward trends in equatorial flow from 160˚E to about 120˚W are dominant during times of strong/weak easterly wind stress. Additionally, trends in SST persist for about three months after the most significant trends in surface currents. The westward equatorial flow trends in NDJF would tend to build SSH in the West Pacific and decrease SSH in the Central/East Pacific. We observe this as positive SSH trends from 140˚E-160˚E and negative SSH trends from 180˚-80˚W in DJFMAM (Figure 2.7b). Additionally, the westward flow would advect climatologically cold-water westward and increase subsurface upwelling in the Central Pacific, setting up the SST trends observed in DJFMAM (Figures 2.7a, 2.6b, and 2.8). As the westward flow trend weakens and disappears in February, the cold SST and low SSH trends persist for three months before responding to an eastward surface current trend in June-July.

During these months the climatological surface flow is westward at an average rate of 9.15 cm s^{-1}, while the trend in the zonal current is eastward at 6.13 cm s^{-1} $decade^{-1}$ (Figures 2.7b and 2.7c side panels). The eastward trend is expected to significantly slow down the mean equatorial flow, reducing the build-up of water in the western basin as well as decreasing the removal of water in the east. Consequently, SSH increases in the Central/East Pacific and decreases in the West Pacific over the 20-year period (Figure 2.7b). In addition, the eastward surface current trends would generate a tendency toward eastward warm-water advection in the West Pacific eastward, increasing SST in JJASON (Figures 2.7a and 2.8). Similarly, the positive SST and SSH trends persist three to four months after the eastward flow weakens in July. The abrupt reversal in surface current trends is surprising and may be explained by the fact that the zonal wind stress trends always have a relatively strong easterly component from 170˚E to about 120˚W during the 20-year

period (Figures 2.1b and 2.7a). A west-to-east reversal in the surface current trends is therefore likely due to the weakening of the easterly wind stress from April to August. Ultimately, the trends in the zonal surface current are acting to enhance the mean seasonal cycle seen in the left panels of Figures 2.7b and 2.7c.

Although the boreal summer and fall trends in SST and SSH are insignificant, they do elicit a significant trend of D20 (Figure 2.7c). In December, trends of D20 are largely negative from about 170˚W-120˚W. Over the following five months the shoaling D20 trends steadily shift eastward, and as a result, the increasing trend in the zonal gradient of D20 is most pronounced in boreal winter and spring (Figures 2.4 and 2.7c). The opposite case occurs in May when positive (deepening) D20 trends are located throughout the entire West and Central Pacific from 140˚E-160˚W. The deepening thermocline then propagates eastward from June-November, flattening the trend in the zonal gradient of D20.

A full heat budget analysis was not possible using the GECCO2 data set as the required budget terms were not saved. Instead, we provide a qualitative illustration of the trend in zonal advection of temperature anomalies from 2.5˚S-2.5˚N during 1990-2009. Figure 2.8 shows the trends in zonal temperature advection in ˚C month^{-1} decade^{-1} estimated by finite differencing of monthly means and linear regression. The trend significance in the two components of zonal temperature advection was previously reported in Figures 2.7. Thus, we leave off stippling in Figure 2.8 for clarity, as the plot is rather noisy. In particular, the temperature gradient east of about 130˚W is too noisy to produce a confident interpretation; therefore, we limit our analysis to west of this longitude. In NDJF, there is a trend towards enhanced westward cold-water advection on the order of -0.2 to -0.3˚C month^{-1} decade^{-1} from about 160˚E-150˚W, which is consistent with the negative SST trends observed in the following three months (Figures 2.7a and 2.8). During

times of increasingly eastward flow (June-July), there is a trend towards eastward warm-water advection on the order of 0.11˚C month^{-1} decade^{-1}. The weakening of the climatologic surface flow seen in Figures 2.7b and 2.7c would reduce cold-water advection during boreal summer and produce a tendency toward warm-water advection, which is consistent with the positive SST trends seen in Figure 2.7a for the following 2-3 months.

Trends of D20 have significant impacts on subsurface circulation intensity from 1990-2009 (Figures 2.4 and 2.5). Therefore, we should expect seasonal variations in trends of D20 to have significant impacts on the seasonal cycle of these subsurface circulations, particularly in the zonal direction (Figure 2.7c). Figure 2.9 shows a longitude/depth cross-section for the trend in DJFMAM and JJASON from 1990-2009. As in Figure 2.5b, stippling and vectors represent significance at 95% for a Mann-Kendall test. During DJFMAM, there is a strong westward trend in the flow near the surface centered on the dateline, which is consistent with the wind-driven westward equatorial surface flow seen in Figures 2.7b and 2.7c. Westward trends in the surface layer are also consistent with the westward advection of cold-water seen in Figure 2.8 and cooling SST trends in the Central/East Pacific (Figure 2.9a). The subsurface warming trends, first seen in Figure 2.5b, persist throughout the year, which is consistent with the positive D20 trends shown in Figure 2.7c. East of 170˚W, however, the subsurface temperature trends follow the seasonal variation of the D20 trends with cooling in DJFMAM when the thermocline shoals and warming in JJASON when the thermocline deepens.

The dominant trend in currents below 50m is a pronounced strengthening of the EUC from 180˚-140˚W on the order of 9 cm s^{-1} decade^{-1}. This is generally consistent with a stronger zonal gradient in D20 during this time of the year (Figures 2.4 and 2.7c). Overall, Figure 2.9a depicts an intensifying zonal wind-driven circulation. In contrast, during JJASON the D20 zonal gradient

trend, while not zero, is substantially weaker and not significant compared to the DJFMAM trend (Figure 2.7c). Recall from Figure 2.5b, the most significant annual mean trend of the EUC is 6.9 cm s^{-1} $decade^{-1}$. The trend in the EUC during DJFMAM is greater than the annual mean trend while the JJASON trend is much less (4 cm s^{-1} $decade^{-1}$), indicating that the most significant increase in the strength of the EUC occurs in the boreal winter and spring.

Figure 2.10 is the same as Figure 2.9 except for meridional cross-sections of the Central and West Pacific. During DJFMAM, the Central Pacific is experiencing strong cooling from the surface to about 100m on the equator and around 10˚N (Figure 2.10a). On the equator and near 2˚S there are significant current trends showing increased upwelling that could be contributing to the equatorial cooling. During JJASON, however, the strong cooling in the central equatorial Pacific gives way to warming trends along the equator while the cooling trends persist around 10˚N. These equatorial variations occur in spite of stronger trends in upwelling during JJASON compared to DJFMAM. This suggests that seasonal variations in central equatorial Pacific temperature trends are dominated by seasonal variations in the trends of D20 and zonal temperature advection, which show a similar seasonal cycle (Figures 2.7c, 2.8, 2.10a, and 2.10b).

In the West Pacific, significant warming trends occur throughout much of the subsurface during DJFMAM and JJASON, with a slight southern hemisphere asymmetry. The persistent warming trends could be due to the consistent deepening trends observed in D20 (Figure 2.7c); however, it is possible that the intensified subduction and equatorward flow seen in the annual mean trend is increasing meridional advection of warm water from 1990-2009 and significantly contributing to the subsurface warming trends (Figures 2.6d, 2.10c, and 2.10d).

All of the above GECCO2 SST results were compared with ERSST data and were generally consistent. For brevity we include only the time-latitude average of SST trends in the

equatorial Pacific (Figure 2.11). Like GECCO2, the observations also support a seasonal variation in the SST trend with cooling most prominent in DJFMAM and diminishing to neutral or warming conditions in JJASON. It should be noted that the magnitude of GECCO2 SST trends is slightly higher for a given trend relative to ERSST.

Similarities between GECCO2 and TAO/TRITON SST trends are to be expected because TAO/TRITON vertical temperature profiles were among the data assimilated into GECCO2 (Köhl and Stammer 2008). Nevertheless, a 30-year 4D-var assimilation may not necessarily reproduce observed SST accurately. Thus, time-latitude averages of SST and zonal wind stress trends measured by the TAO/TRITON array were generated and compared to GECCO2 (Figure 2.12). There exist large data gaps in the TAO/TRITON SST and zonal wind stress products due to instrument failure, particularly in the West/Central Pacific. Therefore, it was necessary to resample GECCO2 data to be temporally and spatially consistent with TAO/TRITON data. When comparing Figures 2.12a and 2.12b there is a strong spatial correlation in the magnitude and timing of SST trends between the resampled GECCO2 data and TAO/TRITON. Moorings east of 170˚W demonstrate a strong seasonality in the 20-year cooling trends that is consistent with both ERSST and GECCO2. Moorings west of 170˚W do not show such a striking seasonal dependence, which is also consistent with the notion that the majority of the seasonal cycle observed in GECCO2 was found in the Central/East Pacific. The trend in the zonal wind stress is also generally consistent in the Central Pacific with the most easterly trends occurring in boreal winter and the weakest in the summer.

Figure 2.13b shows the trend in ADCP-measured zonal current velocity taken by equatorial TAO/TRITON moorings. There is an eastward trend to the EUC at 165˚E, 170˚W, 140˚W, and 110˚W with the strongest component ranging from 11 cm s^{-1} $decade^{-1}$ at about 200m to 16 cm s^{-1}

decade^{-1} about 100m from west to east. Figure 2.13a shows the trend in GECCO2-derived zonal currents, resampled to be spatially consistent with the available TAO/TRITON ADCP data. GECCO2 shows a positive trend in the EUC from 1990-2009 at 165˚E, 170˚W, and 140˚W, but it fails to reproduce the anomalous eastward flow at 110˚W (Figure 2.13b). Additionally, GECCO2 tends to underestimate the observed trend in the zonal current velocity with maximum values of about 5 cm s^{-1} decade^{-1} and 10 cm s^{-1} decade^{-1}, west-to-east. This depth difference, however, is consistent with the shoaling of the EUC from west to east in tandem with the thermocline. In general, GECCO2 consistently captures the observed structure of current variability, but has a weaker trend than observed during the transition to the hiatus period.

2.4 Summary and discussion

The response of equatorial Pacific surface and subsurface dynamics to a consistent increase in zonal wind stress during the transition from a non-hiatus (positive PDO) to the present hiatus period (negative PDO) was quantified using an ocean reanalysis product. Comparisons to observational data from ERSST and TAO/TRITON moorings were generally consistent with GECCO2 results. It was found that surface waters have been anomalously advected further westward over the past 20 years along the equatorial Pacific. Associated changes to SSH and zonal thermocline depth gradients were associated with a more vigorous wind-driven subsurface circulation consistent with previous studies using models that were not constrained with observations (e.g., England et al. 2014).

The trends discussed in this study bear resemblance to longer centennial time scale trends reported elsewhere. For example, Drenkard and Karnauskas (2014) show a 20th-century deepening and westward shift of the EUC core that is similar to Figure 2.5b using a different reanalysis

product. Yang et al. (2014) also show a long-term strengthening over 1900-2008 of tropical Pacific interior flow associated with a spin up of Pacific subtropical cells that is comparable to Figure 2.6. Nevertheless, the trends reported here are larger than the longer time scale trends, most likely because they are due to more energetic processes operating on shorter decadal time scales associated with, for example, the PDO. Some of the physical processes involved in these two time scales may be similar, though an analysis to determine the degree of correspondence is beyond the scope of this study. Additional investigation is also needed to clarify whether the trends we described are associated with changes in ENSO statistics (McPhaden et al. 2011). For example, the SST trends in Figure 2.2 are reminiscent of a Central Pacific La Niña pattern (e.g., Ashok et al. 2007; Lee and McPhaden 2010), which has been the focus of major research efforts in recent years (e.g., Capotondi et al. 2015; Amaya and Foltz 2014).

A major finding of this study is that the seasonal variations during this transitional period are driven by seasonal variations in zonal advection trends of climatologic surface waters and the seasonal deepening/shoaling of the thermocline that influence equatorial upwelling. These surprising reversals in current trends and enhanced/weakened upwelling combine to cause anomalous cooling in DJFMAM and anomalous warming in JJASON. Changes in the surface currents appear to be driven by variations in the strength of the easterly wind stress. A further consequence of the seasonal reversal of the anomalous surface current is a seasonal variation in the strength of zonal and meridional wind-driven subsurface circulations along the equator. The seasonal spinning up and slowing down of these subsurface circulations has important impacts on the redistribution of heat in the tropical Pacific Ocean. A quantitative analysis using a model with a consistent and complete heat budget is needed to evaluate this further and should be the focus of future studies.

During the recent hiatus, the global mean SAT trend showed a pronounced seasonality, positive during the boreal winter and negative during summer (Cohen et al. 2012). In the limit that the tropical Pacific is the driving force behind the hiatus, Kosaka and Xie (2013) suggested that seasonal differences in Northern Hemisphere teleconnections induced by tropical Pacific SST anomalies cause the seasonality of global mean SAT trend. Our results differ from their work in that we show a pronounced seasonal variation in the La Niña-like pattern in the tropics, which may cause a seasonal variation in tropical atmospheric cooling. The seasonality of decadal variability has not been rigorously investigated. The results of these two studies motivate further research into decadal seasonal variations and how such variability impacts remote climates and projects onto global SAT trends.

Pinpointing the missing heat associated with the global warming hiatus is crucial to our understanding of such events (e.g., Balmaseda et al. 2013; Chen and Tung 2014; Kintisch 2014; England et al. 2014). While uncertainties regarding the magnitude (Karl et al. 2015) and the mechanisms driving the beginning and end of a hiatus remain, its impact on climatically significant regions such as the tropical Pacific can be identified. This study takes an important step toward increasing our understanding of the region and may help to improve our ability to predict both regional and remote climate variability associated with transitions into future hiatuses. Hiatus periods are likely to affect future decadal warming trends (Easterling and Wehner 2009; Hansen et al. 2011), so continuing to improve our understanding of their causes and consequences and should be a high priority for additional research.

2.5 Acknowledgements

GECCO2 ocean reanalysis data is available at http://icdc.zmaw.de/.ERSSTv3b data set is freely available and maintained by NOAA's National Climate Data Center. TAO/TRITON data can be delivered by PMEL at http://www.pmel.noaa.gov/tao/. The NCDC PDO Index can be found at https://www.ncdc.noaa.gov/teleconnections/pdo/. This research was conducted by DJA with partial funding from AJM by the NSF (OCE-1419306), SPX by the NSF (1305719), and the Robert Scripps Fellowship. MJM is supported by NOAA. PMEL contribution no. 4310. We thank three anonymous reviewers for comments that improved the quality of this paper.

Chapter 2, in full, is a reprint of the material as it appears in Amaya, D. J., S.-P. Xie, A. J. Miller, and M. J. McPhaden (2015), Seasonality of tropical Pacific decadal trends associated with the 21st century global warming hiatus, Journal Geophysical Research Oceans. The dissertation author was the primary investigator and author of this paper.

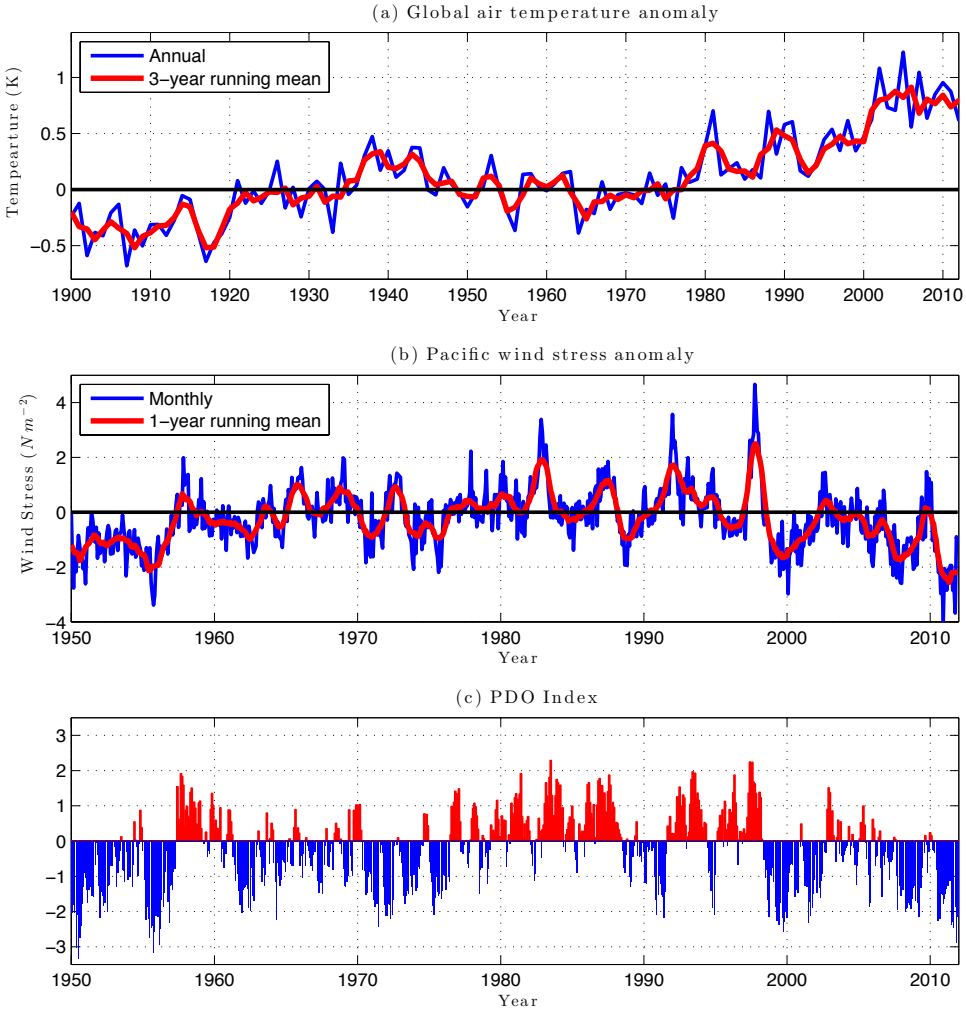

Figure 2.1: GISS global averaged surface air temperature anomalies (a), zonal wind stress anomalies averaged 5˚S-5˚N, 180˚-150˚W (b), and the Pacific Decadal Oscillation (PDO) Index (c). The upper panel runs from January 1900 to December 2011, while both (b) and (c) from January 1948 to December 2011. Blue time series are annual (a), monthly, negative (c) data (b). Red time series are 3- (a) and 1-year (b) running means and positive PDO values (c). Wind stress anomalies were scaled by 100.

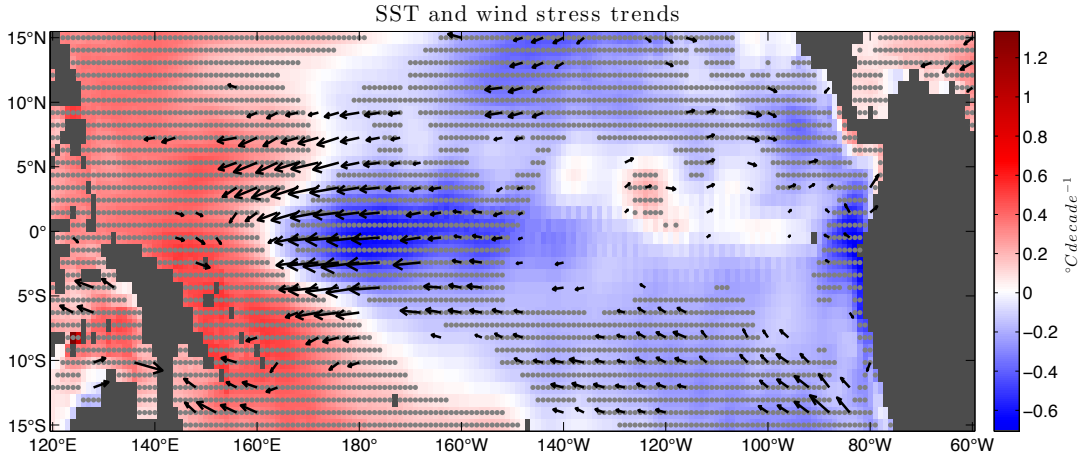

Figure 2.2: Trends in SST (˚C decade^{-1}) and surface wind stress (N m^{-2} decade^{-1}) during 1990-2009. Stippling indicates SST trend significance at the 95% level. Wind stress vectors are only plotted where significant at the 95% level. The maximum wind stress trend vector represents 0.02 N m^{-2} decade^{-1}.

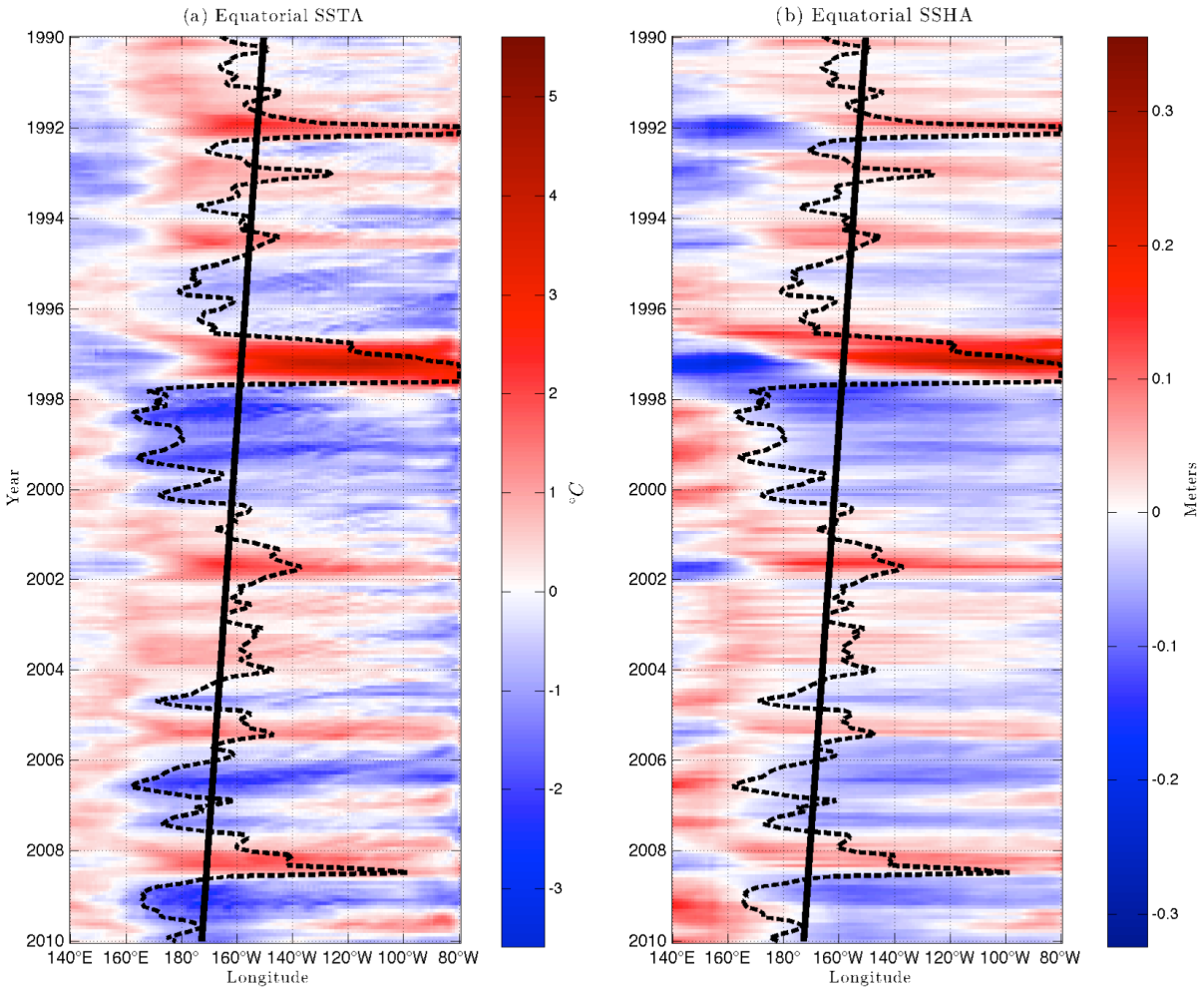

Figure 2.3: Time/longitude plots of SST anomalies (a) and SSH anomalies (b) averaged over 5˚S-5˚N. The dashed lines outline the 27.5˚C isotherm. The line of best fit is in solid black.

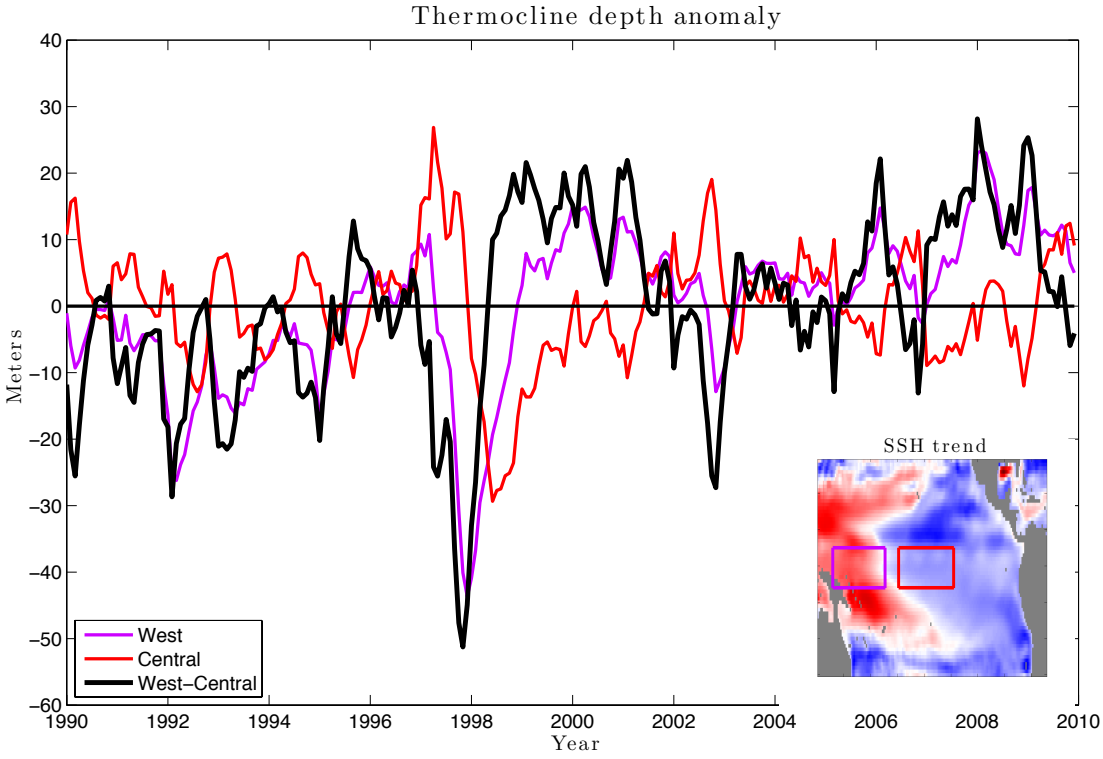

Figure 2.4: Time series for the depth of the 20˚C isotherm averaged from 5˚S-5˚N, 140˚E-180˚W (purple box/line), 5˚S-5˚N and 170˚W-130˚W (red box/line). The difference of the purple box from the red box is shown in black. Positive (negative) anomalies represent a deeper (shallower) thermocline. The insert shows the SSH trend.

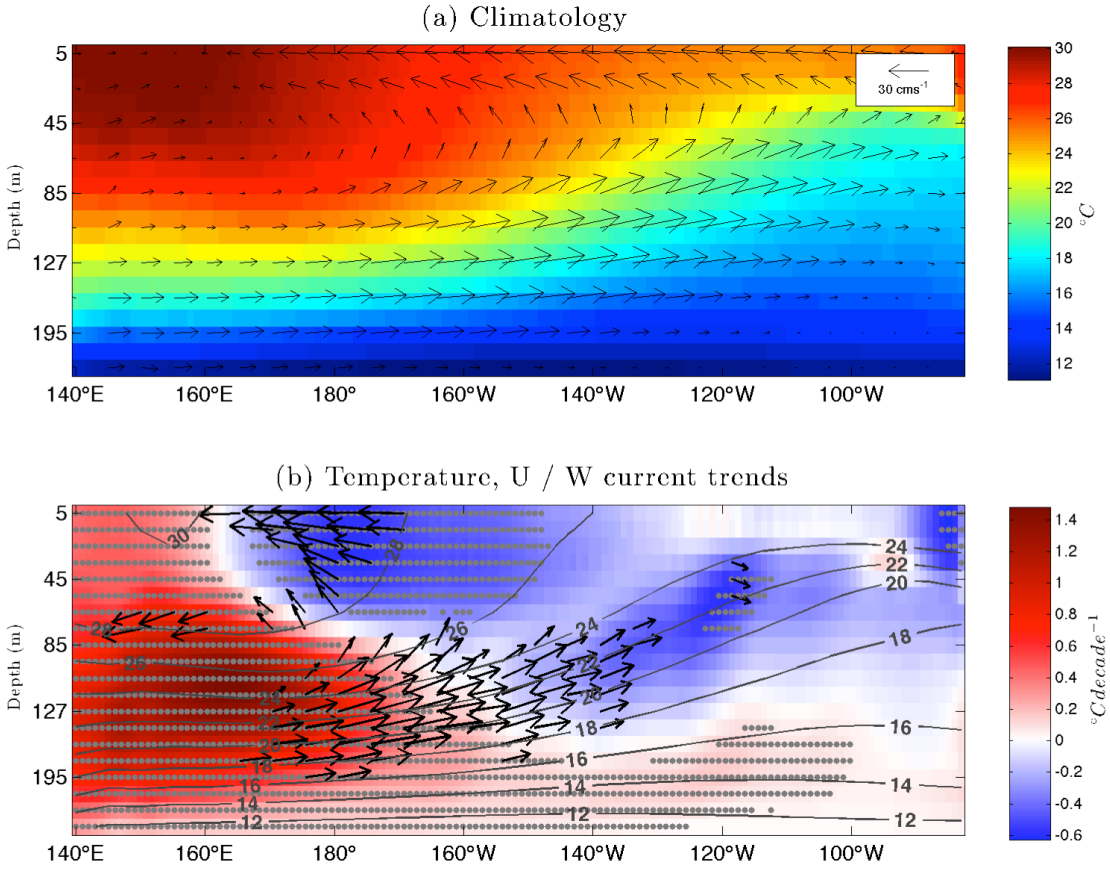

Figure 2.5: Longitude/depth cross-sections of temperature (shading) and currents (vectors) averaged over 2.5˚S-2.5˚N for (a) mean climatology (1980-2010) and the linear trends during 1990-2009 (b). Temperature trends (˚C decade^{-1}) are in shading and U/W current trends (cm s^{-1} decade^{-1}) are black vectors. Gray contours in (b) represent the mean climatology of temperature. Stippling indicates temperature trend significance at the 95% level. Current vectors are only plotted where significant at the 95% level. The maximum current trend vector represents 8.5 cm s^{-1} decade^{-1}. Note: in the figure the vertical velocity component of current vectors has been scaled by 10^4.

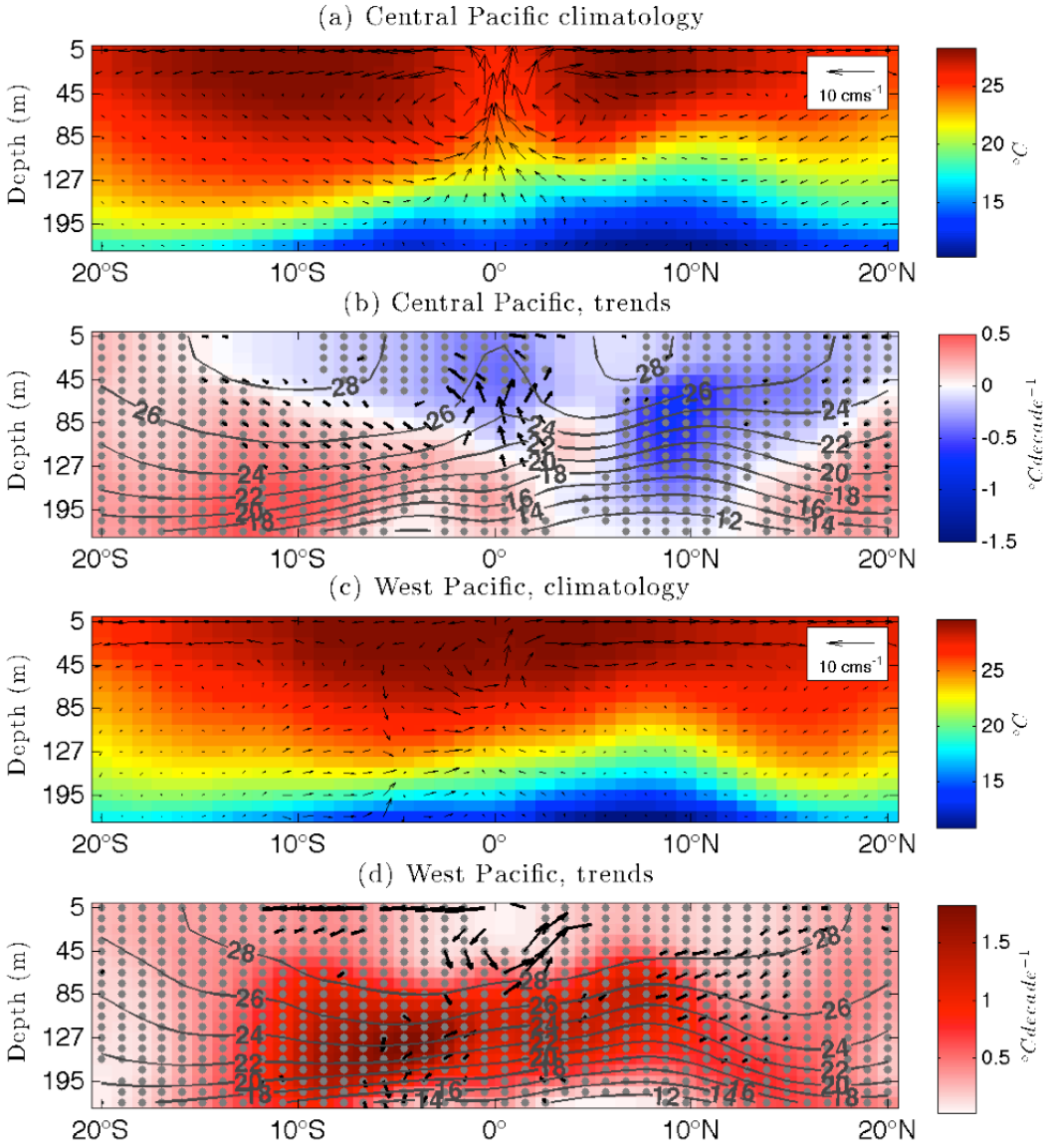

Figure 2.6: Same as Figure 2.5, but latitude/depth cross-sections of temperature and currents. Averaged from 180˚-120˚W (a, b) and 140˚E-180˚ (c, d). Gray contours in (b, d) represent the mean climatology of temperature for the respective region. Stippling and vectors represent significance at the 95% level. The maximum current trend vector represents 2.5 cm s^{-1} $decade^{-1}$ and 3.2 cm s^{-1} $decade^{-1}$ for (b) and (d) respectively.

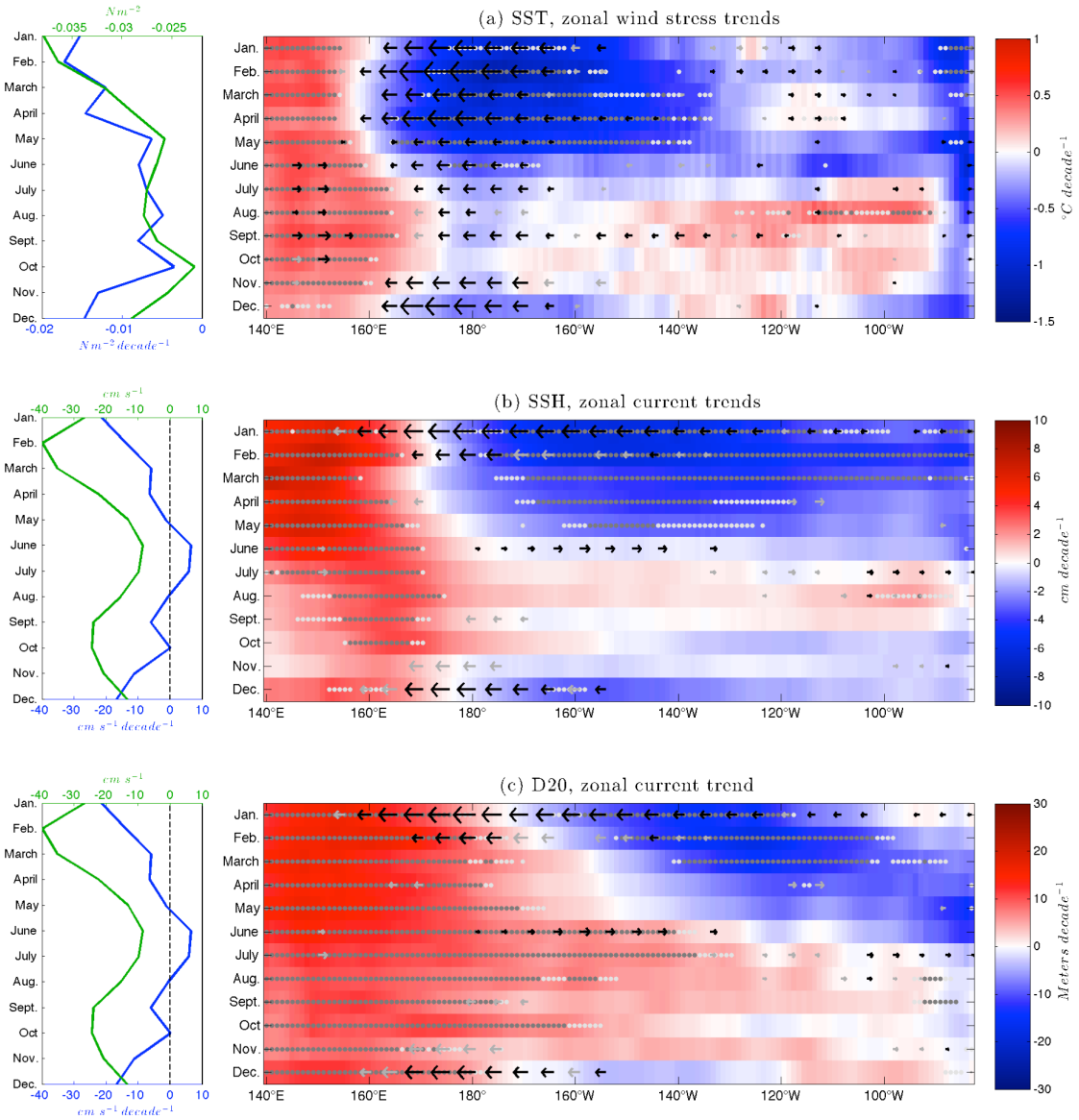

Figure 2.7: Time/longitude plots of the 1990-2009 trends in SST (a, ˚C decade^{-1}), SSH (b, cm decade^{-1}), and D20 (c, meters decade^{-1}) in shading and zonal wind stress (a only, N m^{-2} decade^{-1}) or 5m zonal current (b and c, cm s^{-1} decade^{-1}) averaged from 2.5˚S-2.5˚N. Zonal wind stress trends (a) and zonal current velocity trends (b, c) averaged from 160˚E-150˚W are shown in corresponding seasonal cycles to the left in blue. The mean 1990-2009 seasonal cycles for zonal wind stress (N m^{-2}) and zonal current velocity (cm s^{-1}) are in green. Dark gray and light gray stippling represents temperature trends significant at 90% and 80% respectively. Zonal wind stress and zonal current velocities are black for 90% significance and light gray for 80%. The maximum zonal wind stress trend vector represents 0.03N m^{-2} decade^{-1} and the maximum current trend vector represents 26 cm s^{-1} decade^{-1}.

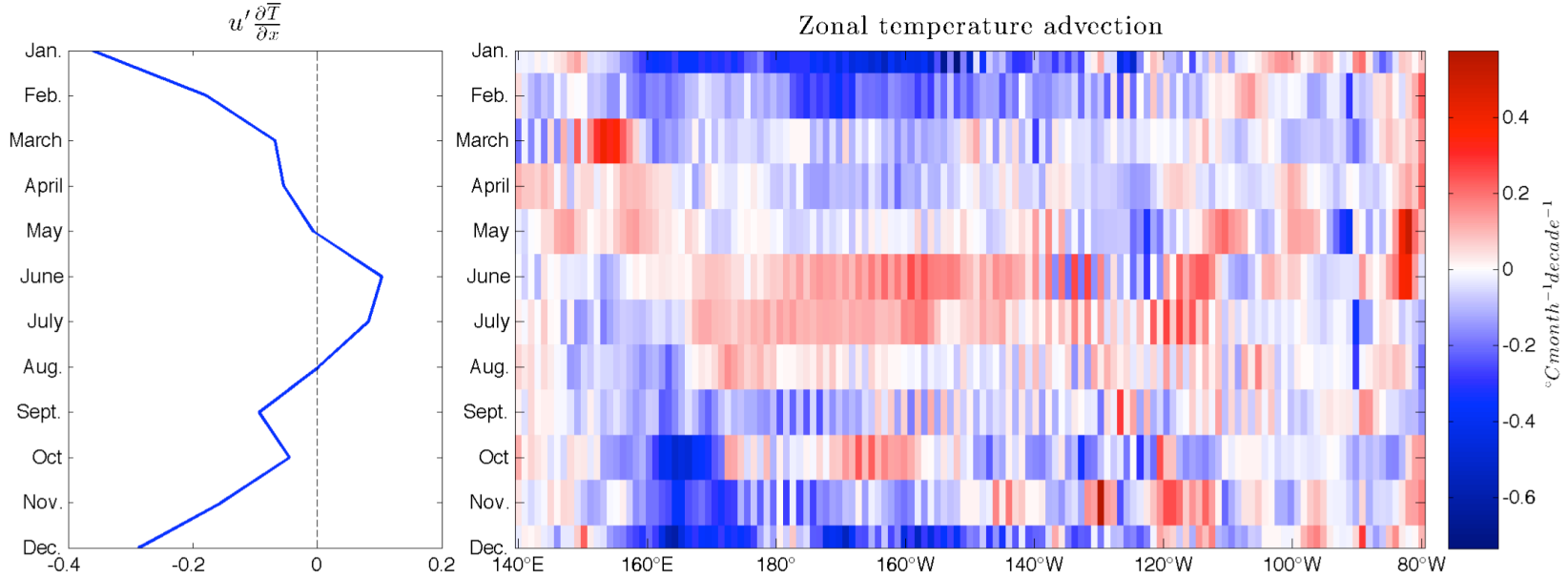

Figure 2.8: Same as Figure 2.7, but zonal surface temperature advection trends (˚C month^{-1} decade^{-1}) from 1990-2009. Zonal temperature advection trends averaged from 160˚E-150˚W are shown to the left. This data was taken from the raw model grid.

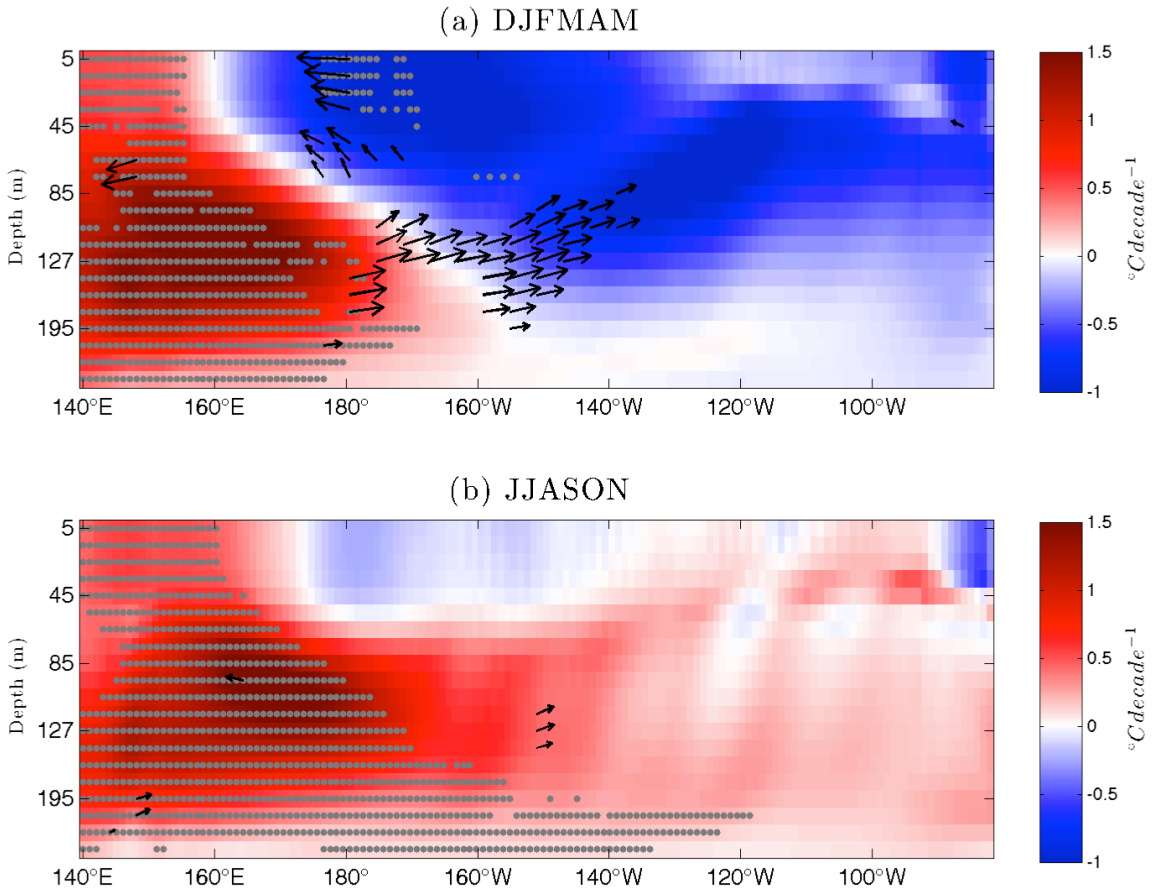

Figure 2.9: Same as Figure 2.5b, but linear trends of DJFMAM (a) and JJASON (b) from 1990-2009. The maximum current trend vector represents 16.1 cm s^{-1} $decade^{-1}$ and 5.3 cm s^{-1} $decade^{-1}$ for (a) and (b) respectively.

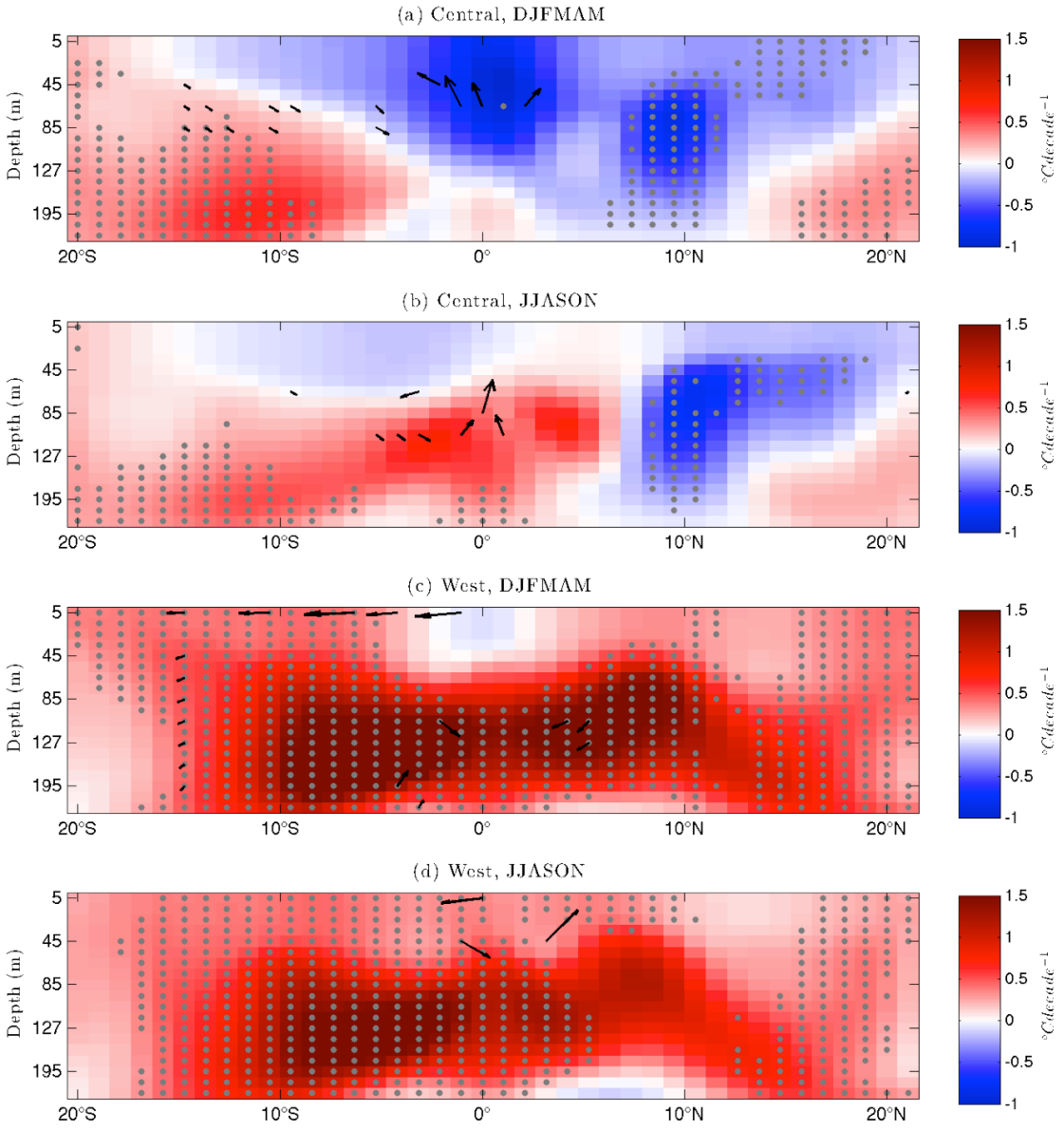

Figure 2.10: Same as Figure 2.6 (b, d), but averaged over DJFMAM (a) and JJASON (b). The maximum current trend vector represents 2.96 cm s^{-1} $decade^{-1}$, 3.2 cm s^{-1} $decade^{-1}$, 2.8 cm s^{-1} $decade^{-1}$, and 3.5 cm s^{-1} $decade^{-1}$ for (a), (b), (c), and (d) respectively.

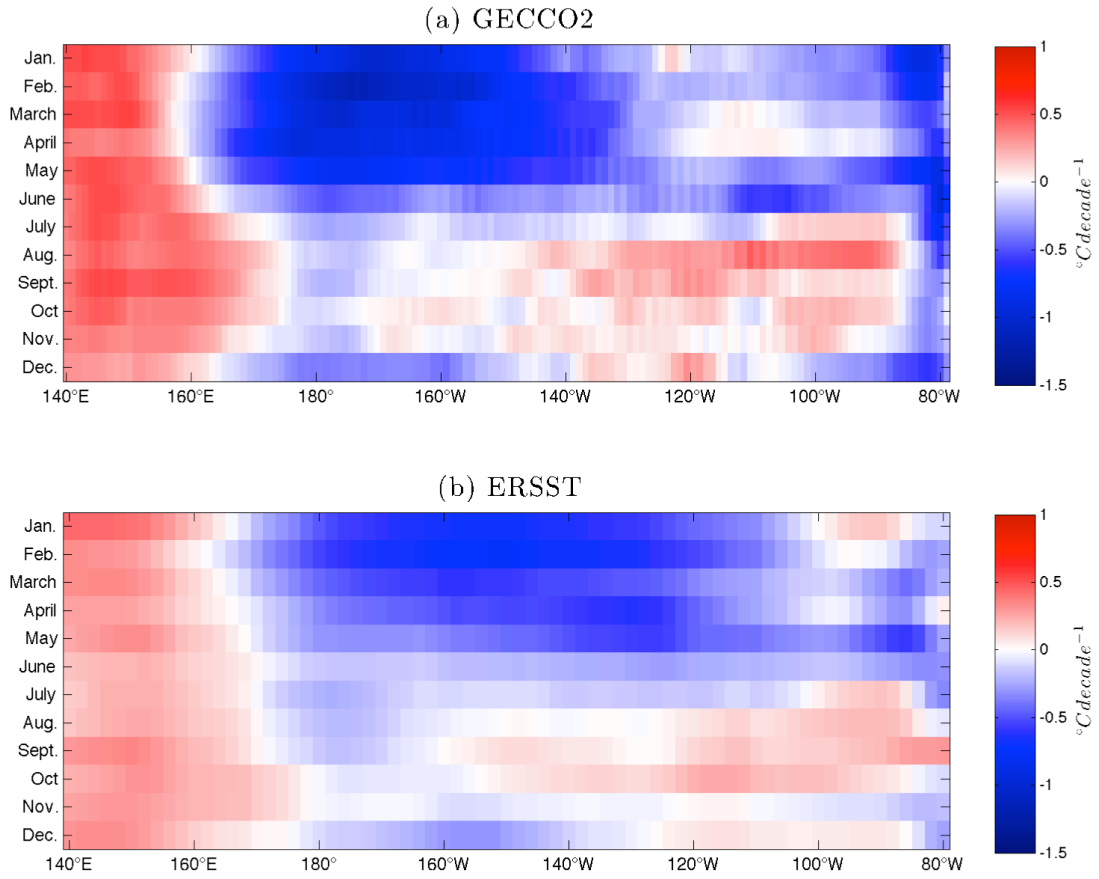

Figure 2.11: Same as Figure 2.7a, but for GECCO2 (a) and ERSST averaged SST (b) trends.

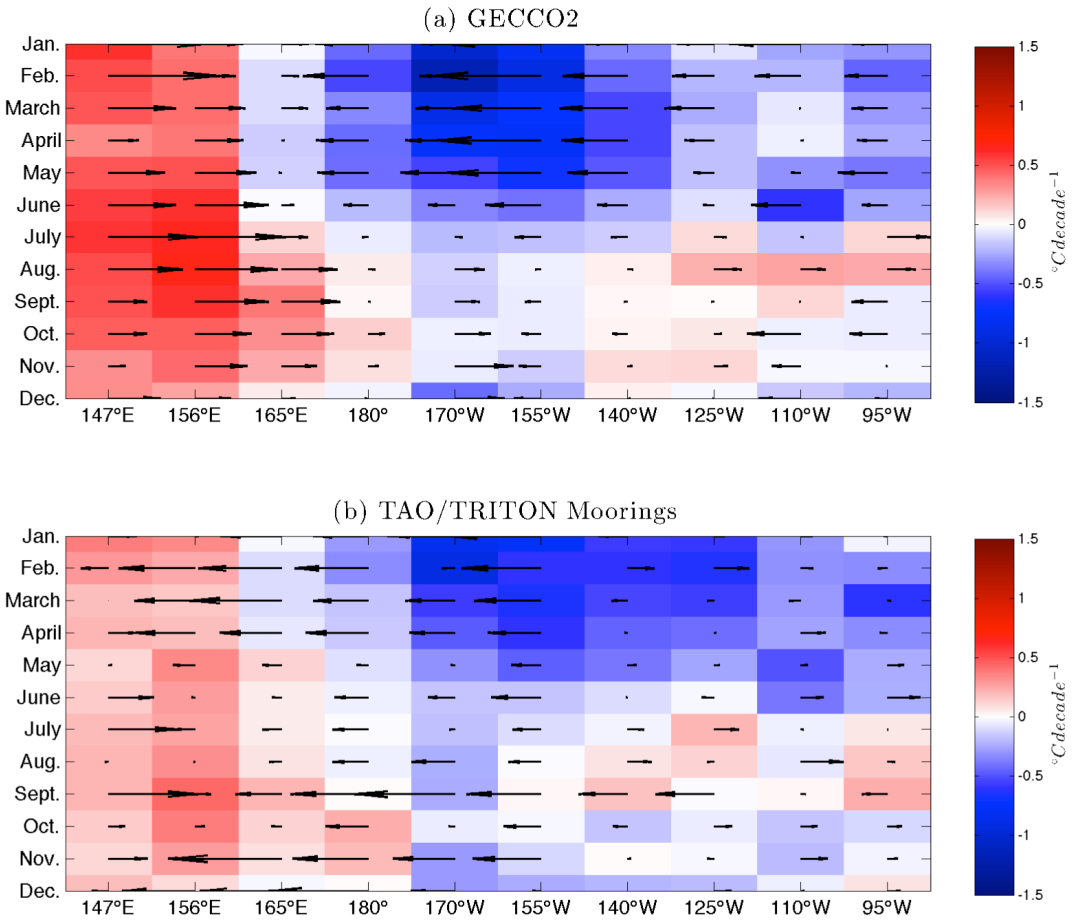

Figure 2.12: Same as Figure 2.7a, but for GECCO2 SST and zonal wind stress trends (a) and TAO/TRITON SST and zonal wind stress trends (b). All moorings from 5˚S-5˚N were averaged along each longitude line. The maximum zonal wind stress vector represents 0.91 N m^{-2} $decade^{-1}$ and 0.02 N m^{-2} $decade^{-1}$ for (a) and (b) respectively.

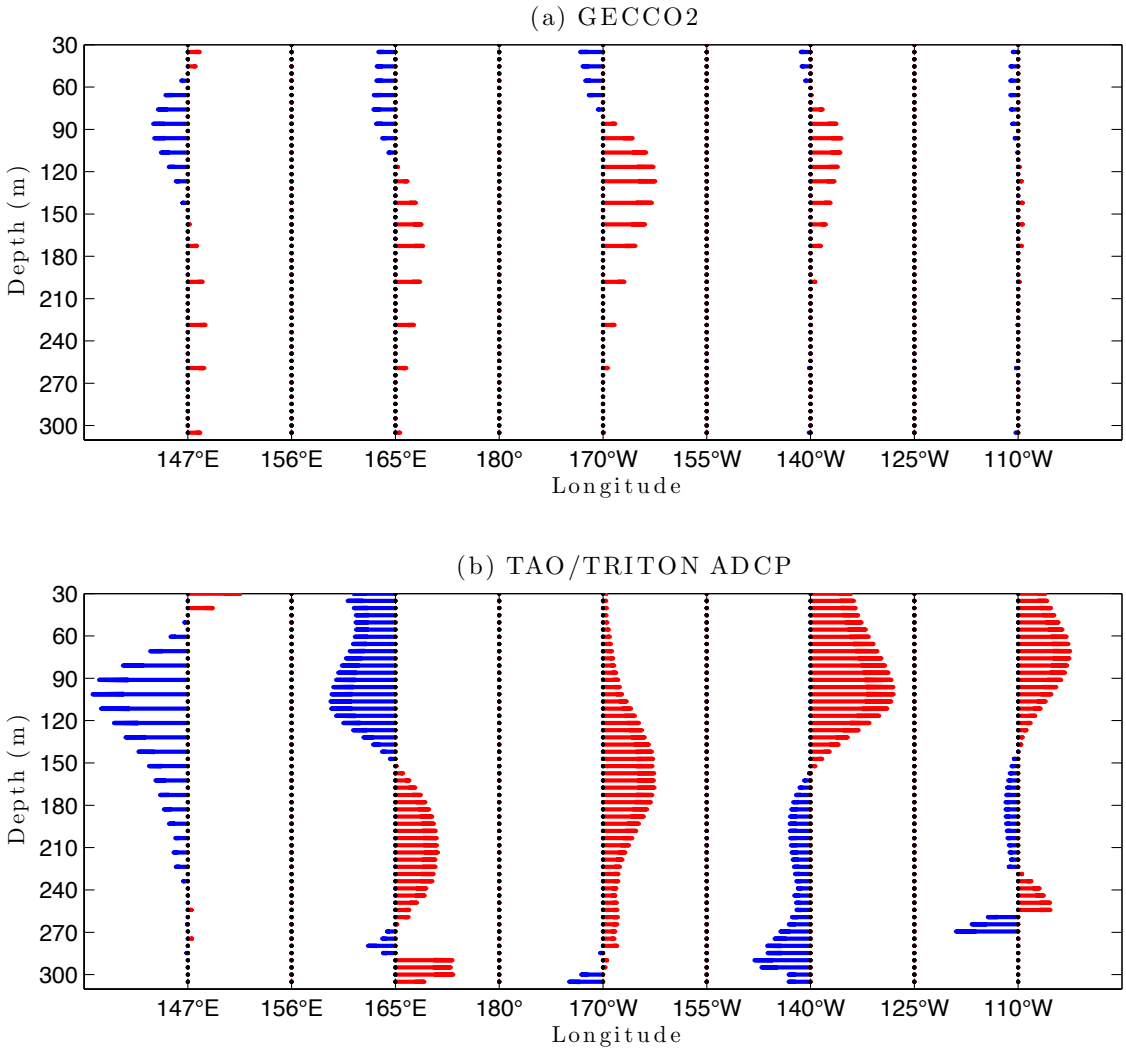

Figure 2.13: TAO/TRITON mooring ADCP measurements of the zonal current velocity trend at 0˚ latitude (a) and GECCO2 derived zonal current velocity trends at 0.5˚ latitude (b). Red vectors represent eastward trends (cm s^{-1} $decade^{-1}$), while blue represents westward trends. The maximum current trend vector represents 16.0 cm s^{-1} $decade^{-1}$ and 10.1 cm s^{-1} $decade^{-1}$ for (a) and (b) respectively.

Chapter 3

The Interplay of Internal and Forced Modes of Hadley Cell Width Variability

Abstract

The poleward branches of the Hadley Cells and the edge of the tropics show a robust poleward shift during the satellite era, leading to concerns over the possible encroachment of the globe's subtropical dry zones into currently temperate climates. The extent to which this trend is caused by anthropogenic forcing versus internal variability remains the subject of considerable debate. In this study, we use a Joint EOF method to identify two distinct modes of tropical width variability: (i) an anthropogenically-forced mode, which we identify using a 20-member simulation of the historical climate, and (ii) an internal mode, which we identify using a 1000-year pre-industrial control simulation. The forced mode is found to be closely related to the top of the atmosphere radiative imbalance and exhibits a long-term trend since 1860, while the internal mode is essentially indistinguishable from the El Niño Southern Oscillation. Together these two modes explain an average of 70% of the interannual variability seen in model "edge indices" over the historical period. Since 1980, the superposition of forced and internal modes has resulted in a period of accelerated Hadley Cell expansion and decelerated global warming (i.e., the "hiatus"). A comparison of the change in these modes since 1980 indicates that by 2013 the signal has emerged above the noise of internal variability in the Southern Hemisphere, but not in the Northern Hemisphere, with the latter also exhibiting strong zonal asymmetry, particularly in the North

Atlantic. Our results highlight the important interplay of internal and forced modes of tropical width change and improve our understanding of the interannual variability and long-term trend seen in observations.

3.1 Introduction

Recent studies have shown a significant expansion of the tropics since 1980 in a variety of observational products (e.g., Hu and Fu 2007; Fu and Lin 2011; Davis and Rosenlof 2012; Nguyen et al. 2013). This widening has been indicated by poleward displacements of the Hadley Cells (Hu and Fu 2007), subtropical dry zones (e.g., Sousa et al. 2011; Hoerling et al. 2012), extratropical storm tracks (Bender et al. 2012), and jet streams (Archer and Caldeira 2008). Such a major shift in global circulation and precipitation patterns has had a profound impact on communities and ecosystems found at the poleward margins of the subtropical dry zones, including higher occurrences of droughts in southern portions of Australia (CSIRO 2012), the southwestern United States (Cayan et al. 2010), the Altiplano region of South America (Morales et al. 2012), the Mediterranean (Sousa et al. 2011; Hoerling et al. 2012), and northern China (Ye 2014). This has led to significant public concern over a possible large scale "desertification" of these typically mild climates, and widespread interest in understanding the mechanisms governing tropical expansion.

While there is a broad agreement that the tropics are expanding, the magnitude of expansion depends on how the tropical boundary is defined and the dataset used for the analysis (Davis and Rosenlof 2012; Lucas et al. 2014). One common measure is the latitude closest to the equator at which the mid-tropospheric mass streamfunction is equal to zero (i.e., where mass transport shifts from poleward to equatorward between the Hadley Cell and the Ferrel Cell). According to this metric, total observed expansion can range from 0.2 to 3.2 degrees latitude

decade^{-1} depending on the reanalysis product (Johanson and Fu 2009; Davis and Rosenlof 2012). Other measures of tropical width are based on changes in tropopause height, which can be independent of Hadley Cell variability (Seidel et al. 2008). The zonal mean tropopause is relatively flat in the tropics with a height of about 15km, but it lowers moving poleward to about 11-13km in the extratropics and about 9km near the poles. Therefore, tropopause-based edge metrics estimated from radiosonde (Seidel and Randel 2006) and reanalysis data (Davis and Birner 2013) have utilized subtropical height thresholds to estimate symmetric expansion to be between –0.5-3.1 degrees latitude decade^{-1}. Additionally, surface observations of zonal mean precipitation minus evaporation (P – E) have been used to define the edge of the tropics as the transition between the E dominated subtropics (which reside under the subsiding branch of the Hadley Cells) to the P dominated mid-latitudes (i.e., the latitudes closest to the equator at which P – E = 0). This method suggests tropical expansion trends of –0.7-2.5 in different reanalysis products (Davis and Rosenlof 2012).

The wide range in the trend estimates listed here could be due to each metric's propensity to isolate discrete levels of the atmosphere that have varying observational coverage. As a result, some estimates based on reanalysis data are less constrained by observations than others, and they can be plagued by the biases and errors associated with the underlying model used in a given reanalysis product (Trenberth et al. 2001; Sterl 2004). Additionally, early estimates that utilized absolute thresholds (like tropopause height) may be biased high due to uniform tropopause rise as a result of global warming.

Previous studies point to two main causes of Hadley Cell expansion since 1980. First, climate models forced with the observed increase in greenhouse gases produce a tropical widening (Lu et al. 2008; Hu et al. 2013); however, the magnitude of the trend is generally underestimated

relative to observations. This has led some to suggest that non-greenhouse gas forcings, (i.e., anthropogenic aerosols and stratospheric ozone) may also play a significant role (Kang et al. 2011; Allen et al. 2012; Min and Son 2013; Kovilakam and Mahajan 2015; Waugh et al. 2015; Allen and Ajoku 2016)

Second, other studies have pointed to the primary influence of natural variability (Garfinkel et al. 2015). For example, multidecadal trends in the Northern and Southern Annular Modes are thought to be important, with expansion (contraction) during their positive (negative) phases driven by shifts in mid-latitude gross static stability (Previdi and Liepert 2007; Kang et al. 2011; Nguyen et al. 2013). Other studies have pointed to the importance of the El Niño-Southern Oscillation (ENSO) and the Pacific Decadal Oscillation (PDO), with contraction (expansion) of the Hadley Cell occurring during periods when SSTs in the tropical eastern Pacific are warm (cool) (Lu et al. 2008; Grassi et al. 2012; Allen et al. 2014; Lucas and Nguyen 2015; Mantsis et al. 2017; Allen and Kovilakam 2017). Lucas and Nguyen (2015) used radiosonde data and partial regression techniques to conclude that the 1980-2013 PDO phase change may account for as much as 50% of the widening over Asia, while (Allen and Kovilakam 2017) used tropical Pacific pacemaker experiments to suggest that unforced decadal ENSO variations can account for nearly all of the Northern Hemisphere (NH) zonal mean expansion and much of the Southern Hemisphere (SH) trend.

Disentangling the natural and forced contributions to Hadley Cell variability and expansion with such a limited observational record is a difficult task. These limitations are further compounded when taking into account the tendency of current width metrics to sample single levels of the atmosphere without considering how the tropical edge might vary with height. In this study, we attempt to overcome these limitations by using targeted modeling experiments and

developing an objective, multivariate estimate of Hadley Cell width variability over a range of latitudes and heights to investigate the interaction between natural and forced variability over the satellite era. We find that since 1980, the superposition of forced and internal variability has resulted in an unusual period of accelerated Hadley Cell expansion, drawing parallels to a similarly unusual phenomenon—the global warming hiatus (Fyfe et al. 2016). Furthermore, we find that the strength of the forced tropical expansion is not symmetric about the equator, with the signal already emerging above the noise in the zonal mean SH, but not the NH. Finally, we consider zonal variations, moving beyond most previous studies that focused on the zonal mean. We find that while the SH largely follows the zonal mean results, the NH displays significant zonal variations, particularly in the North Atlantic. Our results add to the mounting evidence that internal variability plays a significant role in observed tropical expansion and raises several interesting questions for future studies.

The rest of the paper is organized as follows. In Section 3.2, we outline the data and methods used in the analysis. In Section 3.3, we discuss the interplay of internal and forced modes of tropical width variability in the zonal mean, and then explore zonal variations in these interactions in Section 3.4. We conclude with a summary and discussion in Section 3.5.

3.2 Data and methods

3.2.1 Joint Empirical Orthogonal Function

To objectively analyze variability of the zonal mean overturning circulation at a variety of atmospheric levels, we calculated a Joint Empirical Orthogonal Function (EOF) from 60˚S to 60˚N using three parameters widely discussed in the tropical expansion literature: 1) The zonal mean meridional mass streamfunction (MMS) at 500mb (Equation 3.1; ψ_{500}), 2) The zonal mean height

of the tropopause (Z_T), and 3) The zonal mean precipitation minus evaporation (P – E). The MMS was calculated as:

$$\psi(P,\phi) = \frac{2a\cos\phi}{g}\int_{P_0}^{P}[v]dp \tag{3.1}$$

where a is the radius of the Earth, g is gravitational acceleration, ϕ is latitude, P_0 is the model's lowest pressure level, and v is the meridional wind component, with brackets denoting the zonal average. The tropopause was calculated using monthly mean data and defined according to the World Meteorological Organization (WMO) lapse rate definition (WMO, 1957). We focus only on the annual mean (from July to the following June) in order to better represent variability that is symmetric about the equator. Anomalies were calculated by removing the long-term annual mean climatology from each variable. Before taking the EOF, each of the individual components was normalized by its Frobenius norm (i.e., the square root of its total variance) and combined into a single matrix. The results of the Joint EOF are three spatial patterns representing the leading modes of ψ_{500}, [Z_T], and [P – E] as a function of latitude, where the time variability for all three patterns is described by a single principal component (PC). Here we focus only on the leading EOF and PC, for reasons that will become apparent in Section 3.3. Results are consistent if the domain is extended to 90˚S-90˚N or if just the NH or SH is included in the Joint EOF.

There are four main advantages to calculating the Joint EOF of ψ_{500}, [Z_T], and [P – E]. First, the method draws out the leading modes of variability among the three parameters without any *a priori* assumptions about what those modes might look like. Second, each chosen variable is related to a common Hadley Cell edge index found in the literature (Lucas et al. 2014). Third, the parameters represent horizontal slices at different pressure levels, which allows us to sample Hadley Cell variability throughout the troposphere without constraining our analysis to a single pressure surface. Finally, the Joint EOF identifies the modes when ψ_{500}, [Z_T], and [P – E] vary in

tandem, and maximizes the signal by cutting down on unrelated noise present in the individual parameters. When an EOF is taken for each individual parameter, the resulting spatial pattern tends to be a linear combination of the first and second Joint EOFs (not shown), which muddles the physical interpretation of the mode. Therefore, the Joint EOF method is the preferred method of isolating modes of variability in the zonal mean overturning circulation variability.

3.2.2 GCM experiments and observational datasets

We utilize two different experiments from the Geophysical Fluid Dynamics Laboratory climate model version 2.1 (GFDL-CM2.1) to separate and analyze natural and forced tropical width variability. First, natural variability is investigated using the 1000-year pre-industrial control simulation with all atmospheric forcings set to 1860 levels. Second, a 20-member historical all-forcing experiment from January 1861 to December 2014 is used to approximate the forced response. The historical ensemble includes 10-members from the CMIP5 archive and an additional 10-members run by Kosaka and Xie (2016). These experiments were initialized from a 600-year control and were forced with observed atmospheric forcings until 2006, and the RCP4.5 projected emissions scenario thereafter. CM2.1 has a resolution of approximately 2˚ latitude x 2.5˚ longitude with 17 vertical levels. The detailed formulation of CM2.1 has been documented by Delworth et al. (2006), and additional information regarding the additional 10-member historical ensemble and the control simulation can be found in Kosaka and Xie (2016).

For observations, we use the National Oceanic and Atmospheric Administration's (NOAA) Extended Reconstructed SST versions 3b (ERSSTv3b; Smith et al. 2008), and atmospheric temperature, wind velocity, precipitation and evaporation from the Modern Era Retrospective-analysis for Research and Applications 2 (MERRA2; Bosilovich et al. 2015). The net effective

radiative climate forcing from 1880-2012 was taken from Hansen et al. (2011), and is available at http://www.columbia.edu/~mhs119/EnergyImbalance/Imbalance.Fig01.txt.

3.3 Internal and forced modes of tropical width variability

3.3.1 Internal mode

We begin with the internal mode, which explains 49% of the total interannual variance across the three parameters within the pre-industrial control simulation. The climatology of ψ_{500} (black line) in Figure 3.1a shows large positive (negative) values north (south) of the equator, representing the poleward branches of the NH and SH Hadley Cells. These terminate around 30˚ as zero crossings in either hemisphere (ψ_{500}= 0; vertical dashed lines), which are often defined to be the "edge" of the tropics (e.g., Lucas et al. 2014). Superimposed on the climatology is the leading internal mode of ψ_{500} variability (blue line). This mode features anomalies that are a near mirror-image about the equator, with two opposite-signed peaks in each hemisphere. The peaks correspond to negative (positive) anomalies on the equatorward flanks of the NH (SH) climatological Hadley Cell and positive (negative) anomalies on the poleward flanks. Note that the anomalies are slightly larger in magnitude in the NH than in the SH.

A similar pattern is seen in the leading internal mode for the other two parameters (Figures 3.1b and 3.1c). The [Z_T] climatology (black line) depicts a maximum tropopause height in the tropics of about 15.5 km, dropping to about 9 km near 60˚ in either hemisphere. The tropical edge is similarly marked, but in this case as the latitude where the tropopause is 1.5 km less than the tropical (15˚S-15˚N) mean (i.e., ΔZ_T = 1.5 km; Davis and Rosenlof 2012). Here the EOF shows positive anomaly peaks that slightly favor the NH (orange line), while a broad region of negative anomalies prevails within the tropics (Figure 3.1b). Finally, the climatology of [P – E] shows two

peaks, indicative of a double-ITCZ (Figure 3.1c, black line). Poleward of these rain bands, there are regions of negative values in the subtropics associated with the descending branch of the climatological Hadley Cell. The subtropical dry zones end with zero crossings around 40˚ in both hemispheres ([P – E] = 0), indicating a transition to mid-latitude storm tracks. The leading internal mode in [P – E] shows positive anomalies poleward of the model's ITCZ climatological peaks and negative anomalies from 10˚S-10˚N that are nearly symmetric about the equator, along with negative anomalies at the subtropical edges overlying the climatological zero crossings.

In each case, the leading Joint EOF projects strongly in the tropics and in tropical edge regions traditionally captured by the various edge indices outlined in the literature (vertical dashed lines). Further, the sign of the anomalies and their meridional positions are all consistent with a poleward expansion of each parameter's climatological tropics. This is highlighted by the high correlation between the associated internal mode PC (PC_{int}; purple line Figure 3.2a) and individual total (NH + SH) tropical edge indices (R = 0.75, R = 0.94, and R = 0.71 for ψ_{500} = 0, ΔZ_T = 1.5 km, and [P – E] = 0 respectively). In contrast, PCs from the next four EOFs do not project as strongly on these edge indices, and tend to have average correlation coefficients of less than 0.2 (not shown). Thus, the leading internal mode can be confidently interpreted as a measure of internal tropical width variability, and we will not focus on higher order modes as a result.

PC_{int} is strongly correlated with the Nino3.4 index (R = –0.96; black line), indicating that its variability is primarily driven by ENSO (Figure 3.2a). The negative sign of the correlation indicates that high values of PC_{int} correspond to a La Niña-like pattern. These results are consistent with several studies showing that a La Niña anomalously weakens the thermally driven subtropical jet stream, shifting eddy-momentum convergence and the meridional circulation poleward (Robinson 2002; Seager et al. 2003; Lu et al. 2008).

3.3.2 Forced mode

We now focus on the forced mode, which represents the Joint EOF within the ensemble mean of 20 GFDL-CM2.1 historical all-forcing simulations, and explains 62% of the total interannual variance (Figure 3.1, bottom row). Averaging across the ensemble reduces random internal variability, thereby enhancing the signal of the forced response. In addition, each parameter was first linearly detrended, subjected to a 10-year low-pass filter, and then retrended before calculating the EOF, further minimizing the influence of internal variability.

The PC for the forced mode (PC_{for}) is characterized by a long-term secular trend from 1860-2013 that is intermittently punctuated by strong negative peaks (Figure 3.2b). PC_{for} is highly correlated with the low-passed net effective climate forcings at the top of the atmosphere (TOA) from 1880-2012 derived from Hansen et al. (2011) (black line; R = 0.97; R = 0.85 detrended). Therefore, these negative peaks could be due to strong volcanic forcing, while the long-term trend may be attributed to increased greenhouse gases and decreased stratospheric ozone concentration throughout the historical period, which is supported by the high correlation between low-passed global mean SST (GMSST) and PC_{for} (R = 0.98; R = 0.89 detrended). Similar to PC_{int}, PC_{for} also projects strongly on low-passed variability at the edge of the tropics, with raw (detrended) correlations of R = 0.98 (0.88), R = 0.91 (0.70), and R = 0.93 (0.72) for the total (NH + SH) ψ_{500} = 0, ΔZ_T = 1.5 km, and [P – E] = 0 edge indices respectively. The high correlation of PC_{for} with TOA radiative forcings, GMSST, and the traditional edge indices gives us confidence that the Joint EOF method is credibly capturing the time variability and trend associated with the prescribed external forcing of the zonal mean overturning circulation in this model.

The forced EOFs spatial patterns (Figures 3.1d-f) have several similarities to their internal counterparts (Figures 3.1a-c). For example, in all three parameters there are forced anomalies of the same sign as the internal anomalies overlying the subtropical zero crossings of the ψ_{500} and [P – E] climatology and near the regions where ΔZ_T = 1.5 km. This suggests that the forced mode induces a similar poleward expansion of the climatological Hadley Cells, tropical tropopause heights, and subtropical dry zones as the internal mode. However, while the internal mode anomalies are slightly larger in the NH, there is an asymmetry in the magnitude of the forced anomalies in favor of the SH. Uniform forcings like greenhouse gas emissions influence the tropics nearly equally between hemispheres (Lu et al. 2008; Seager et al. 2010; Hu et al. 2013), but an asymmetric forcing like ozone may explain the enhanced SH tropical expansion in our forced EOF mode (Kang et al. 2011; Polvani et al. 2011b; Min and Son 2013; Lucas and Nguyen 2015). Anthropogenic aerosols are another asymmetric forcing (Wang et al. 2016) that have been hypothesized to contribute to Hadley Cell expansion (Allen et al. 2014), but modeling studies have indicated the ozone effect dominates the SH zonal mean response (Tao et al. 2016).

3.3.3 Mode interactions: total variance and total expansion

To what degree can the forced and internal modes represent the total tropical width variance? To test this, we project each ensemble member of the historical simulation onto the internal and forced EOF patterns to acquire two PCs that represent the time variability of the leading modes of forced and internal tropical width changes in each member. We then construct a multivariate linear regression model for each member based on the regression coefficients between these two PCs and the traditional edge indices discussed previously. We are then able to compare the results of this model to the total (NH + SH) traditional edge indices in each member. Using

this method, we find that the combination of our two EOF modes can explain 66% ± 4%, 85% ± 2%, and 57% ± 5% of the total unfiltered variance in ψ_{500} = 0, ΔZ_T = 1.5 km, and [P – E] = 0 respectively. This result supports the conclusions of recent studies that ENSO and external forcings are the primary drivers of interannual tropical width variability in the zonal mean (Allen et al. 2014; Mantsis et al. 2017; Allen and Kovilakam 2017). Recall, however, that our Joint EOF method does not partition the influence of the different external forcings on Hadley Cell width (i.e., ozone and/or greenhouse gases). As such, single forcing experiments that take advantage of this objective methodology are needed in future studies to further quantify the role of these individual drivers in Hadley Cell width variability.

A related question is, how much of the observed changes in tropical width during the satellite era can be attributed to these modes? To answer this, we first scale the EOFs by the observed changes in each PC from 1980-2013, and then add the results to the climatology of each parameter to measure how far the climatological tropical edges (vertical dashed lines) shift poleward. The scaling required for the forced EOF is fairly straightforward in that it is the change in PC_{for} from 1980-2013 due to the trend, which we estimate to be 1.31σ using a 2nd-order polynomial fit to the entire time series.

The scaling for the internal mode is based on the regression coefficient between PC_{int} and Nino3.4 (R_{coeff} = –0 .94 $\sigma^{\circ}C^{-1}$). Using observed SST from ERSSTv3b, we produce a Nino3.4* index (Chen and Wallace 2015), and calculate the linear trend from 1980-2013 based on the 10-year low-passed time series (–0.66˚C over 34 years; Figure 3.3a). This trend is multiplied by R_{coeff} to get an estimate for the representative scaling in PC_{int} (0.63σ). The fact that the scaling is less than 1σ makes sense because the internal mode is the result of interannual variability and we are interested in a representative multidecadal trend in these anomalies. This does not mean, however,

that the observed trend in Nino3.4* is so common. On the contrary, by calculating a 34-year running trend time series in the control simulation Nino3.4, we put the observed Nino3.4* trend into historical context and find that it was actually quite extreme (~2.12σ) relative to the probabilistic range of 34-year trends that may be expected in nature (Figure 3.3b).

The strong cooling observed in the Nino3.4* index has been linked to a decadal strengthening of the tropical Pacific trade winds (e.g., Watanabe et al. 2014; Amaya et al. 2015), and this acceleration may be the result of aerosol forcing (Takahashi and Watanabe 2016). Therefore, it is possible that the trend in Figure 3.3b is also partially forced by aerosols. However, Allen and Kovilakam (2017) recently used the CMIP5 ensemble to show that forced SST patterns only weakly project on the eastern tropical Pacific during this time period. Thus, we continue under the assumption that the cooling trend in Figure 3.3b is entirely due to internal variability, but we acknowledge that further research is needed to quantify the role of external forcing on tropical Pacific SST trends. These results will be discussed in greater detail in Section 3.5.

The contributions of the scaled anomalies to tropical expansion are reported in Table 3.1 as changes in degrees latitude. Based on the combination of the two Joint EOFs, we estimate a total NH expansion of 0.26, 0.55, and 0.38 degrees latitude and a total SH expansion of 0.38, 0.44, and 0.35 degrees latitude for ψ_{500}, [Z_T], and [P − E] respectively. Interestingly, the internal anomalies account for 58%, 73%, and 63% of the overall NH change in each parameter, but only 42%, 66%, and 40% of the SH expansion. This is generally consistent with Allen and Kovilakam (2017) and others, who suggest that NH tropical expansion is dominated by unforced trends due to ENSO. These model expansion estimates are smaller than most other observational estimates during the same time period, which could be due in part to observational uncertainty (Lucas et al.

2014) or a broader problem with coupled models underestimating the observed tropical expansion (Hu et al. 2013; Tao et al. 2016).

The fact that the expansion of the NH Hadley Cell in the model is primarily driven by natural variability during the satellite era could be due to the differences in the strength of the two EOFs near the tropical edges (note the change in y-axis between top/bottom row of Figure 3.1). The internal anomalies are stronger than the forced anomalies in these regions, particularly in the NH, which is possibly a consequence of the observed asymmetrical strength of ENSO teleconnections to the NH relative to the SH (Garreaud and Battisti 1999). In contrast, the forced anomalies tend to be stronger near the SH tropical edge, which is likely due to the presence of asymmetric forcing such as ozone (Tao et al. 2016). This inverse asymmetry between the two modes leads to a larger difference in the magnitude of internal and forced anomalies near the NH tropical edge and a smaller difference near the SH tropical edge for a 1σ occurrence/trend of both EOFs. Therefore, on short time scales when the trend in PC_{for} is small, we expect that anthropogenic expansion of the NH Hadley Cell would be dominated by natural variability.

3.3.4 Mode interactions: signal time of emergence in the zonal mean

On long time scales, it is interesting to consider the time when the anomalies associated with the forced expansion of the Hadley Cell rise above the noise level of the internal mode. Since we are interested in multidecadal Hadley Cell expansion over the satellite era, we will focus on the time of emergence of the forced trend beginning in 1980. This trend is estimated with a 2nd-order least-squares fit (PC_{fit}; Figure 3.2b) calculated from 1861-2013, and is extrapolated into the future until the signal is sufficiently large (see next paragraph). The trajectory of PC_{fit} corresponds

to a non-equilibrium 2.0˚C increase in GMSST by 2100 (3.0˚C for global mean surface temperature; GMST), which roughly corresponds to the CMIP5 RCP6.0 future warming scenario.

Here we define the time of signal emergence to be the year when the forced trend in each parameter is significantly larger than the probabilistic range of unforced trends in Hadley Cell width due to PC_{int}. This condition is met when:

$$\alpha_k R(\phi_{TE})_{for} > \sigma_k t_{0.95} R(\phi_{TE})_{int} \qquad \text{for k = 2, 3, 4, …, n} \tag{3.2}$$

where ϕ_{TE} is the latitude of the climatological tropical edge defined by the traditional edge indices, α_k is the *k*-year change in PC_{fit} from 1980 to k – 1 years after 1980, R_{for} (R_{int}) is the regression slope at ϕ_{TE} of each respective parameter in the EOF onto PC_{for} (PC_{int}), σ_k is the standard deviation of a *k*-year running trend of PC_{int}, and $t_{0.95}$ is the t-statistic for a 95% confidence interval based on the *k*-year running trend time series. Thus, if the magnitude of the forced trend exceeds the 95% confidence level for *k*-year running trend time series, then we consider the signal to have emerged above the "noise" of PC_{int} (i.e., ENSO-like variability). If the magnitude of the forced trend is not significant, then we increase *k* and repeat the process.

Since these Joint EOF patterns primarily describe the expansion of the Hadley Cells, we report the time of emergence for forced anomalies at the tropical edges (i.e., at the latitudes of the vertical dashed lines in Figure 3.1). Within this framework, we find that the zonal mean forced anomalies contributing to SH Hadley Cell expansion emerge above the ENSO-driven noise level at 95% confidence in 2007, 2010, and 2003 for ψ_{500}, [Z_T], and [P – E] respectively. In contrast, the forced anomalies contributing to NH Hadley Cell expansion do not rise above the noise until 2019, 2015, and 2023. This is consistent with our previous results indicating that forced Hadley Cell variability is larger in the SH than in the NH. It also implies that, in the zonal/annual mean and to the extent that ENSO represents the dominant form of "noise", anomalies that would

contribute to externally forced Hadley Cell expansion over the satellite era may currently be detectible in the SH, while the forced expansion of the NH tropics may become apparent in the next decade based on the current trajectory of the forced trend. Other forms of internal variability produced by different climate modes or stochastic noise may also prove important, but can only delay the signal emergence further into the future for each hemisphere.

3.3.5 Hadley Cell expansion during hiatus periods

Based on the discussion of Figures 3.1-3.3, it is evident that both ENSO-like variability and external forcing play important roles in the year-to-year and long-term changes in tropical width. This conclusion draws interesting parallels between tropical expansion and the recent "hiatus" in global warming (e.g., Amaya et al. 2015; Kosaka and Xie 2016; Xie and Kosaka 2017). In particular, natural modulations of ENSO/PDO and long-term secular warming due to increased greenhouse gases linearly superimpose upon each other to reproduce the so-called global warming "staircase" and the early 2000's global warming hiatus (e.g., Kosaka and Xie 2016).

Similarly, the leading internal mode shown in Figure 3.1 suggests that ENSO variability also plays an important role in modulating tropical width, but in the opposite sense of global temperature, as illustrated in Figure 3.4. Specifically, we hypothesize that decadal shifts between periods of predominantly El Niño events (red shading) to predominantly La Niña events (blue shading) will tend to produce long-term trends (such as in Figure 3.3) that act to dampen forced GMST warming (red line), while simultaneously enhancing forced Hadley Cell expansion as measured by a traditional edge index (green line).

To test this hypothesis, we first show the 14-year trend over the observed "hiatus period" (2000-2013) in Nino3.4* and GMSST for each member of the GFDL-CM2.1 historical simulation

(Figure 3.5a). There are some members that have long-term cooling trends in Nino3.4* during this time period, while others have long-term warming trends. The spread in the trends is due to the presence of internal variability in each member, and the trends themselves represent random transitionary periods between one phase of decadal ENSO variability to the other in the model. Ensemble members with larger warming (cooling) trends in Nino3.4* tend to have larger (smaller) GMSST warming trends than the ensemble mean (forced warming, dashed red line) during this time period (R = 0.74). This is consistent with the red line in our schematic (Figure 3.4) and with previous studies that have shown that long-term changes in ENSO can dampen or amplify forced warming trends (Kosaka and Xie 2013; Fyfe and Gillett 2014).

Figure 3.5b shows the same 14-year trends in GMSST, but compared to 14-year trends in the symmetric Hadley Cell index [P – E] = 0. In general, ensemble members with weaker GMSST warming trends tend to have Hadley Cells that are expanding more rapidly than the ensemble mean or forced expansion (R = –0.73; horizontal red dashed line). This suggests that simulations with prolonged cooling in the equatorial Pacific are not only dampening global warming due to increased greenhouse gases, but are also enhancing the forced expansion of the tropics in the model. This result is further reinforced in by Figure 3.5c, which shows the edge index trend versus the Nino3.4* trend. Broadly, ensemble members with stronger cooling trends in Nino3.4* have accelerated Hadley Cell expansion relative to the ensemble mean, and ensemble members with warming trends in Nino3.4* have dampened forced expansion trends (R = –0.65). Similar correlations are found among 14-year trends in GMSST, Nino3.4*, and P – E over the full simulation period (1874-2013), giving us high confidence in their robustness.

3.4 Zonally varying responses to Hadley Cell expansion

An important focus of recent literature has been on the regional characteristics of Hadley Cell expansion (Choi et al. 2014; Chen et al. 2014; Karnauskas and Ummenhofer 2014; Lucas and Nguyen 2015). These studies have largely been based on radiosonde and satellite data, and they indicate that there may be significant differences in tropical expansion rates depending on the region of interest. In this section, therefore, we extend our EOF analysis to two dimensions, in order to better understand how internal and forced modes of Hadley Cell variability interact regionally.

3.4.1 Zonal variations in P – E and signal time of emergence

Figure 3.6a shows the regression of the low-passed ensemble mean P – E field onto PC_{for} scaled by the change in PC_{fit} from 1980-2013 (1.31σ), which represents the P – E signal associated with forced tropical expansion in the model. Figure 3.6b shows the regression of the control simulation P – E field onto PC_{int}, scaled by the 95% confidence level for 34-year running trends ($\sigma_{34} t_{0.95}$ = 0.63; Equation 3.2). In both cases, the regression pattern has been weighted by the standard deviation of the control simulation P – E at each grid point. The shape of the line in the side-panels of each subplot in Figure 3.6 represents the zonal mean climatology of P – E. The color of the line represents the zonal mean regression of P – E with each respective PC, which has been weighted by the standard deviation of the zonal mean control simulation P – E at each latitude and scaled the same as the spatial map to its left.

The forced P – E regression (Figure 3.6a) is characterized by a near-zonally uniform increase in P – E from 50˚S-60˚S, punctuated by smaller regions of strong P – E reduction in the Southeast Pacific, South Atlantic, and Southeast Indian Ocean, which are likely due to the

poleward shift in the SH subtropical high centers in each basin (Karnauskas and Ummenhofer 2014). This result is further highlighted by the negative zonal mean anomalies found at the climatological SH zero crossing of P – E (Figure 3.6a, side-panel). A similar shift is evident in the NH, but with less zonal symmetry. In the North Atlantic, there is a strong increase in P – E at high latitudes coupled with a strong reduction in subtropical P – E that encompasses much of southern Europe and the Mediterranean Sea. This is consistent with the zonal mean expansion of the NH dry zones and long-term observations of the region (Hoerling et al. 2012). However, in the North Pacific, North America, and over the main Eurasian continent, the anomalies are much weaker, explaining the weaker zonal-mean regressions for the NH as a whole (side panel of Figure 3.6a).

Figure 3.6b shows many of the defining characteristics of a La Niña event. In the tropical Indo-Pacific, there are anomalies consistent with a western shift and intensification of the Walker Circulation and the poleward shift in the zonal mean ITCZ and SPCZ seen in the Figure 3.6b side-panel. In the North Pacific, there is a reduction in P – E throughout the southern portion of the United States, consistent with the Rossby wave train that tends to steer extratropical cyclones to higher latitudes during La Niña events (Horel and Wallace 1981). The North Atlantic, southern Europe, and Mediterranean also experience a drying associated with a poleward expansion of the Hadley Cell, a shift in the precipitation bands, and increased evaporation at the surface due to increased subsidence. As a result, the zonal mean regression of internal anomalies produces a poleward expansion of the NH subtropics with negative anomalies at the NH climatological P – E zero crossing (Figure 3.6b, side-panel). In the SH subtropics, the anomalies are similar in space to the forced anomalies discussed in Figure 3.6a, though their magnitudes are smaller. At high southern latitudes, there are hints of a poleward displacement of extratropical storm tracks with the South Pacific dominating the zonal mean.

Equation 3.2 was applied to each grid point to determine the year in which the P – E signal would rise above the noise. As a result, stippling in Figure 3.6a indicates forced P – E changes that have emerged above the noise-level of PC_{int} at the 95% confidence level by 2013. Consistent with the results presented in Section 3.3.2, much of the SH P – E signal in the subtropics and high latitude Southern Ocean has emerged during the early parts of the 21st century. This once again emphasizes the tendency for the SH forced changes to follow the zonal mean. The bulk of NH forced anomalies over the subtropical latitudes of the North Pacific, North America and Eurasia also follow the zonal mean results and remain below the noise threshold through 2013. The North Atlantic does not follow this pattern, but instead has a large proportion of forced changes (particularly at high latitudes) that are detectible by 2013. This result stands in contrast to the zonal mean view of Hadley Cell expansion discussed earlier and highlights the importance of a regionally varying perspective, particularly with respect to future atmospheric forcings.

3.4.2 Zonally varying mode interactions with observational comparisons

Next, we further analyze any zonal variations in the interaction between the internal and forced modes of Hadley Cell width change during the satellite record (Figure 3.7a). In accordance with the schematic outlined in Figure 3.4, we scale the forced P – E regression pattern by the same change in PC_{fit} from 1980-2013 as before (1.31σ), and then calculate a linear combination of this pattern with the internal mode P – E regression scaled by the observed change in Nino3.4* during the same time period (i.e., 0.63σ; see Section 3.3.3). This exercise allows us to consider the linear enhancement of forced P – E changes from 1980-2013 by the observed decadal shift from predominantly El Niño events to predominantly La Niña events (Figures 3.3, 3.4, and 3.7a).

Generally, the internal P – E anomalies dominate the mode superposition throughout the tropics, North America, and Eurasian continent (Figure 3.7a). However, in regions where the forced anomalies project strongly (i.e., the North Atlantic and SH), the interactions between the modes can be important. For example, the subtropical North Atlantic and Mediterranean regions experience a sharp decrease in P – E as the two modes enhance one another. In the zonal mean, the anomalies found at the NH climatological zero crossing experience a similar strengthening (Figure 3.7a, side-panel) This enhancement is consistent with our earlier results that showed a larger poleward shift of the dry zone edges when the impacts of the internal mode and forced mode "line-up" (Figures 3.4 and 3.5). SH anomalies experience a similar regional and zonal mean intensification with more negative (positive) P – E anomalies throughout the subtropics (high-latitudes) relative to either the internal mode or forced mode individually.

Previous studies have indicated that a combination of anthropogenic forcing and decadal ENSO variations such as in Figure 3.7a can account for most of the observed tropical expansion during the satellite era (Grassi et al. 2012; Allen et al. 2014; Lucas and Nguyen 2015; Mantsis et al. 2017; Allen and Kovilakam 2017). We further test this hypothesis in the zonally varying sense by comparing Figure 3.7a to observed P – E changes associated with observed Hadley Cell width variability. Figure 3.7b shows the observed regression pattern of annual mean MERRA2 P – E fields with a composite Hadley Cell edge index from 1980-2013, weighted by the control simulation P – E standard deviation at each grid point. The composite edge index was taken as the average of three observed total (NH + SH) annual mean edge indices discussed earlier (ψ_{500} = 0, ΔZ_T = 1.5 km, and [P – E] = 0). We combine the indices in this way to get a more robust estimate of the variability and long-term trend in Hadley Cell width, which can vary substantially from one index to another (e.g., Lucas et al. 2014). As in Figure 3.7a, the regression pattern was then scaled

by the observed trend in the composite index over the 34-year period (2.27 degrees latitude) to represent the change in weighted P – E over this time period. Our results are generally consistent using any individual index for the regression.

Broadly, the EOF reconstruction and the observed P – E changes share much of the same large-scale features. Both patterns have a near-zonally uniform P – E increase at high southern latitudes, as well as remarkably consistent pockets of SH subtropical drying. In the NH, they also show a similar decrease in P – E in the Northeast Pacific off the coast of California and a much stronger P – E reduction throughout the North Atlantic and Mediterranean Sea (Bender et al. 2012; Hoerling et al. 2012). The observations also show the Indo-Pacific zonal gradient in P – E that is reminiscent of La Niña-like conditions. All told, we contend that the two patterns are qualitatively quite similar, which further supports the hypothesis that atmospheric forcings and decadal ENSO transitions can explain much of the observed change in tropical width.

Repeating the experiment with different reanalysis products generates similar regression patterns to Figure 3.7b, but the magnitude of the trend in each composite edge index (i.e. the scaling of Figure 3.7b) varies substantially. For example, data taken from the National Center for Environmental Programs Reanalysis 2 (NCEP2) produces a 34-year expansion of less than 1 degree latitude (not shown). As a result, it would appear that the spatial pattern seen in Figure 3.7b is robust, but as currently scaled the magnitude of anomalies may be overestimated as the MERRA2 trend is on the higher end of observational estimates (Lucas et al. 2014). Therefore, despite the EOF reconstruction appearing much weaker than MERRA2 (note the colorbar change), Figure 3.7a falls within the range of observational uncertainty. The good agreement between our results and observations implies that the satellite record just so happens to correspond with a period of accelerated tropical expansion akin to the accelerated warming periods of the 1970s-1990s

(Kosaka and Xie 2016). Indeed, if not for the decadal La Niña-like cooling pattern in the tropical Pacific the observed trend might have been substantially smaller.

3.5 Summary and discussion

In this study, we sought to identify the leading modes of internal and forced tropical width variability without any *a priori* assumptions about what those modes might look like. Using a Joint EOF approach, we found that the leading internal mode is closely associated with ENSO variability, the leading forced mode is related to TOA radiative forcings, and each mode is characterized by symmetric poleward expansion of the climatological Hadley Cells. The forced EOF showed an asymmetry in favor of enhanced SH tropical expansion relative to the NH. This is possibly due to asymmetric ozone forcing (Kang et al. 2011; Polvani et al. 2011b; Min and Son 2013; Tao et al. 2016), but could also be the result of the minimal observed warming in the Southern Ocean relative to the global average (Li et al. 2013; Armour et al. 2016; Hwang et al. 2017), which may act to strengthen the equator-to-pole temperature gradient, thereby strengthening thermal winds and shifting eddy-momentum flux convergence poleward in the SH (Lu et al. 2008).

By taking advantage of the long-term trend in PC_{for}, we estimated the time that the forced trend in Hadley Cell expansion would emerge above the probabilistic range of internally generated trends in the zonal mean and in the zonal varying sense. In the zonal mean, we showed that the forced trend may already be detectible above the noise level in the SH. This was due in part to the asymmetrical nature of the forced mode about the equator and the weaker projection of ENSO in the SH relative to the NH (Garreaud and Battisti 1999). In contrast, we showed that the zonal mean NH forced anomalies could require several more years at their current trajectory to emerge above

this noise level. These results were largely consistent when considering zonally varying P – E fields, but with the important exception of the North Atlantic. Here, the forced poleward shift in North Atlantic subtropical dry zones and mid-latitude storm tracks is mostly detectible above the noise (Figure 3.6a stipples).

One caveat is that these results are primarily based on a single model. GFDL-CM2.1 does not simulate the aerosol indirect effect, and therefore it is possible that aerosol related signals could be muted in this model. However, we achieved qualitatively similar results when repeating the Joint EOF with the Community Earth System Model (CESM) Large Ensemble (Kay et al. 2015), which does incorporate the aerosol indirect effect. We defer to future studies to evaluate the viability of these results in the full CMIP5 ensemble.

This study sheds light on several longstanding questions in the literature. For example, can atmospheric forcing and ENSO variations alone explain the observed changes in tropical width? The internal mode's relationship to ENSO is consistent with the emerging consensus in the literature that tropical expansion generated by a long-term transition from a more El Niño-like state (positive PDO) to a more La Niña-like state (negative PDO) could account for much of the observed trend since 1980 (Lu et al. 2008; Grassi et al. 2012; Allen et al. 2014; Lucas and Nguyen 2015; Mantsis et al. 2017; Allen and Kovilakam 2017). When we put our EOF modes into this observational context by comparing the combination of 1980-2013 changes in our forced and internal modes (Figure 3.7a) to the regression of observed P – E with a composite edge index (Figure 3.7b), we found that our EOF reconstruction qualitatively reproduced the large-scale observed drying of the global subtropics, the southward shift of the SH storm tracks, and much of the tropical anomalies, with the magnitude if the model anomalies falling within the range of observational uncertainty.

Consistent with recent studies of the hiatus, our results further reinforce the importance of accounting for both forced and internally driven variability when interpreting observed climate trends. Here we have focused exclusively on ENSO-driven variability, but other types of variability—e.g., the Annular Modes (Previdi and Liepert 2007) and the Atlantic Multidecadal Oscillation (AMO; Lucas and Nguyen 2015)—may also influence Hadley Cell width. However, it should be noted that our Joint EOF method does not identify these climate modes as major contributors to the interannual variability of Hadley Cell width, even in the higher order EOF modes.

Our study also raises the question of why the forced poleward shift in the storm tracks is stronger in the North Atlantic than elsewhere in the NH? Bender et al. (2012) also showed that the magnitude of the storm track shift was largest in the North Atlantic using satellite observations. Although they suggest this result should be viewed with caution as data artifacts may spuriously amplify the observed trend, their conclusions imply that external forcings (rather than internal variability) may explain the bulk of the trend in this region. Aside from increased greenhouse gases, aerosol and tropospheric ozone forcings have also been suggested as drivers of forced Hadley Cell expansion in the SH (Kim et al. 2017) and in the North Atlantic (Allen et al. 2012; Kovilakam and Mahajan 2015). Since greenhouse gases, ozone, and aerosol forcings are not perfectly correlated during the historical period, it is difficult to assess the relative contributions of these climate forcings to tropical expansion when they are all included in a single mode (e.g., Figure 3.1d-f). Therefore, targeted experiments that utilize single forcing simulations are needed to provide clarity on the role of individual forcings in North Atlantic Hadley Cell modes.

Finally, our results highlight just how unusual the period since 1980 has been. Based on Figure 3.3b, observations suggest the 1980-2013 tropical Pacific cooling was exceptionally intense

in the scope of modeled long-term natural variations. Consequently, this phase change substantially muted the global warming trend and generated accelerated Hadley Cell expansion. As the PDO cycle transitions to a warm phase, we expect the opposite to occur, with accelerated global warming and a "hiatus" in Hadley Cell expansion. On top of the additional contraction expected from ozone recovery (Polvani et al. 2011a), this suggests that the rapid pace of Hadley Cell expansion observed since 1980 will likely not be maintained through the first half of the 21st century.

3.6 Acknowledgements

This material is based upon work supported in part by the National Science Foundation Graduate Research Fellowship (NSF; DGE-1144086). N. S. and S.P.X. are supported by the NSF (1637450). S.P.X. is further supported by the National Key R&D Program of China (2016YFA0601804). A.J.M is supported by the NSF (OCE1419306) and the National Oceanic and Atmospheric Administration (NOAA; NA14OAR4310276). We would like to thank Sarah M. Kang and Kristopher Karnauskas for their helpful comments during the course of our study. We also thank Yu Kosaka for running the additional 10-member GFDL-CM2.1 ensemble and the 1000-year control simulation. We also express our gratitude to the World Climate Research Programme's Working Group on Coupled Modelling, which maintains CMIP. MERRA2 Reanalysis data was provided by the NASA Global Modeling and Assimilation Office, from their web site at https://gmao.gsfc.nasa.gov/reanalysis/MERRA-2/. Finally, we'd like to thank two anonymous reviewers for comments that improved the quality of this paper.

Chapter 3, in full, is a reprint of the material as it appears in Amaya, D. J., N. Siler, S.-P. Xie, and A. J. Miller (2018), The interplay of internal and forced modes of Hadley Cell expansion:

lessons from the global warming hiatus, Climate Dynamics. The dissertation author was the primary investigator and author of this paper.

Table 3.1: Total (NH +SH) tropical expansion (˚latitude) based on scaled anomalies in Figure 3.1.

Metric	Internal 1980-2013	Forced 1980-2013	Internal + Forced 1980-2013
ψ_{500}	NH: 0.15 SH: 0.16	NH: 0.11 SH: 0.22	NH: 0.26 SH: 0.38
$[Z_T]$	NH: 0.40 SH: 0.29	NH: 0.15 SH: 0.15	NH: 0.55 SH: 0.44
[P – E]	NH: 0.24 SH: 0.14	NH: 0.14 SH: 0.21	NH: 0.38 SH: 0.35

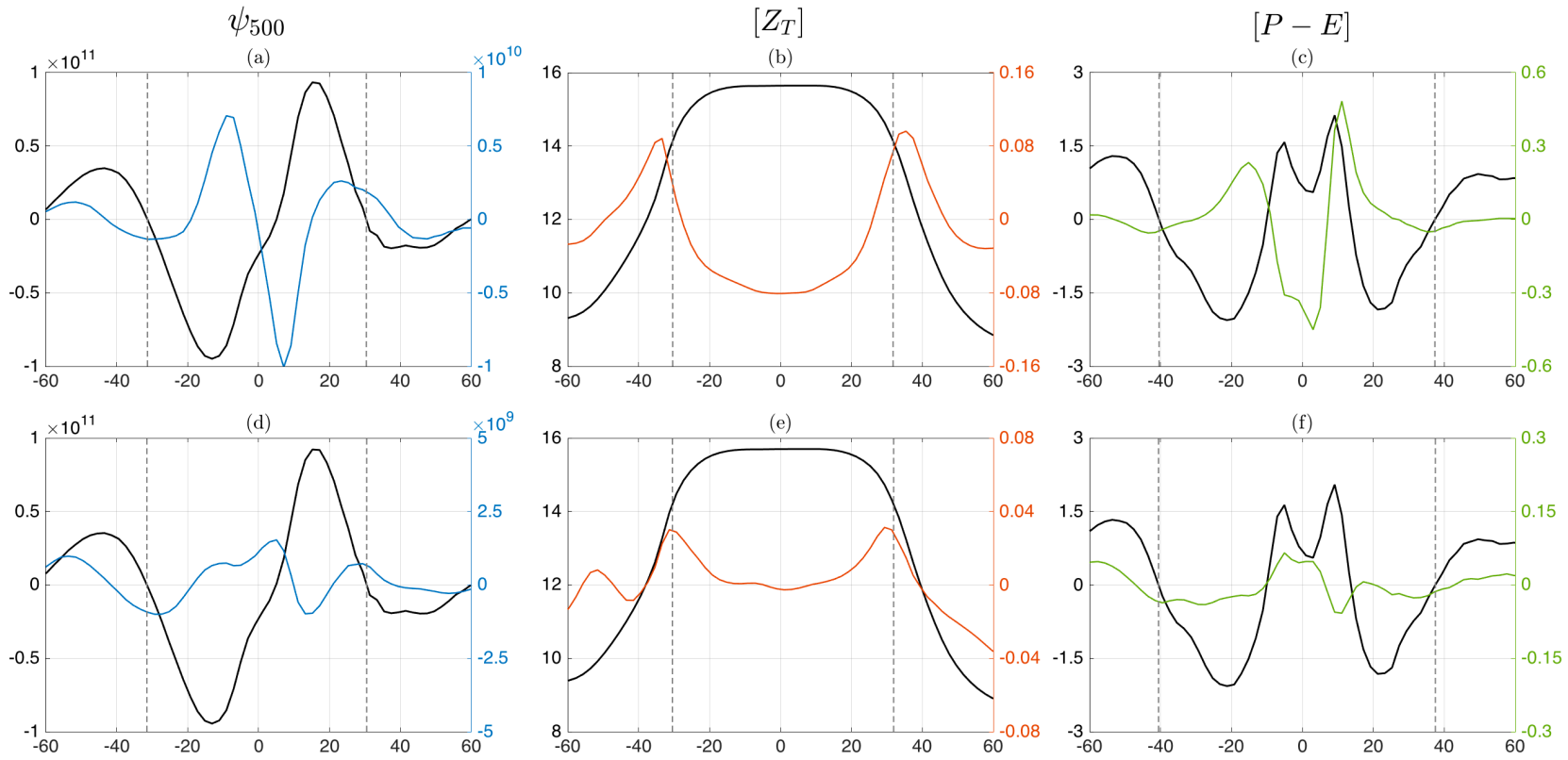

Figure 3.1: Joint EOF of $\boldsymbol{\psi_{500}}$ (kg m^{-1} s^{-1}), [Z_T] (km), and [P – E] (mm day^{-1}) in the 1000-year control simulation (top row) and the low-passed ensemble mean of the 20-member all-forcing historical simulation from 1861-2014 (bottom row). Black lines represent the zonal mean climatology of $\boldsymbol{\psi_{500}}$, [Z_T], and [P – E] respectively. Colored lines are the EOF spatial patterns. Note that we have removed the tropical mean (15˚S-15˚N) from the [Z_T] anomalies to better assess the tropical edges without the influence of globally uniform tropopause rise.

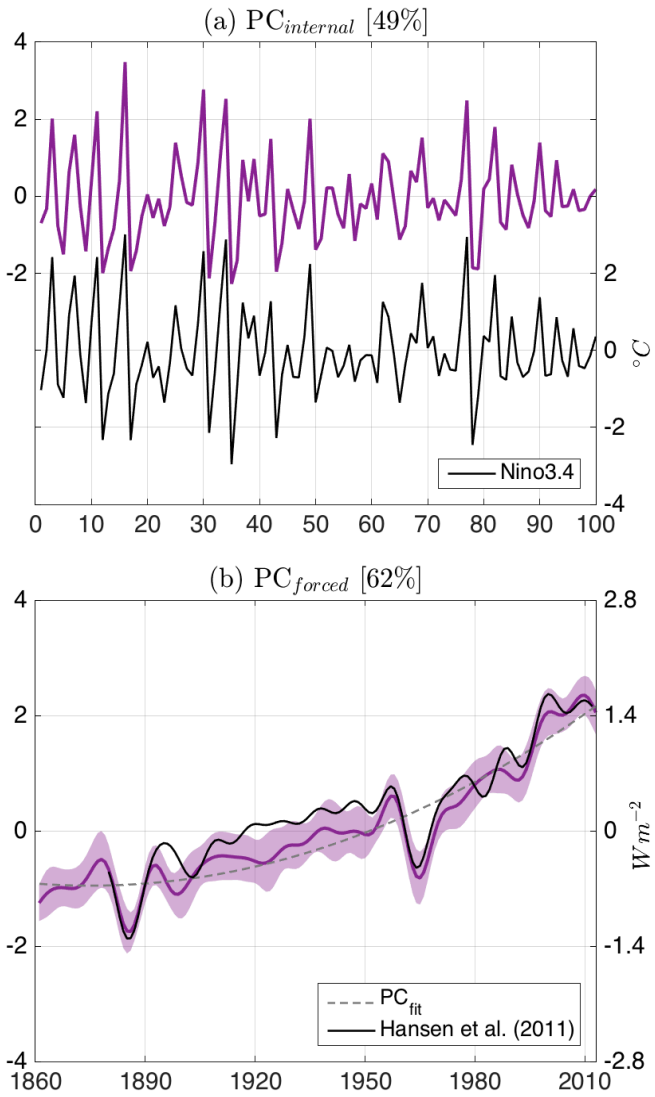

Figure 3.2: PC_{for} and PC_{int} respectively. Numbers in square brackets are the percent variance explained by each EOF mode among the three variables in Figure 3.1. Black line in (a) is the control simulation Nino3.4 index (˚C). For clarity, only the first 100 years of PC_{int} and Nino3.4 are shown. Gray dashed line in (b) is 2nd-order least-squares fit to PC_{for}. Black line in (b) is the net effective climate forcing taken from Hansen et al., (2011) (W m^{-2}).

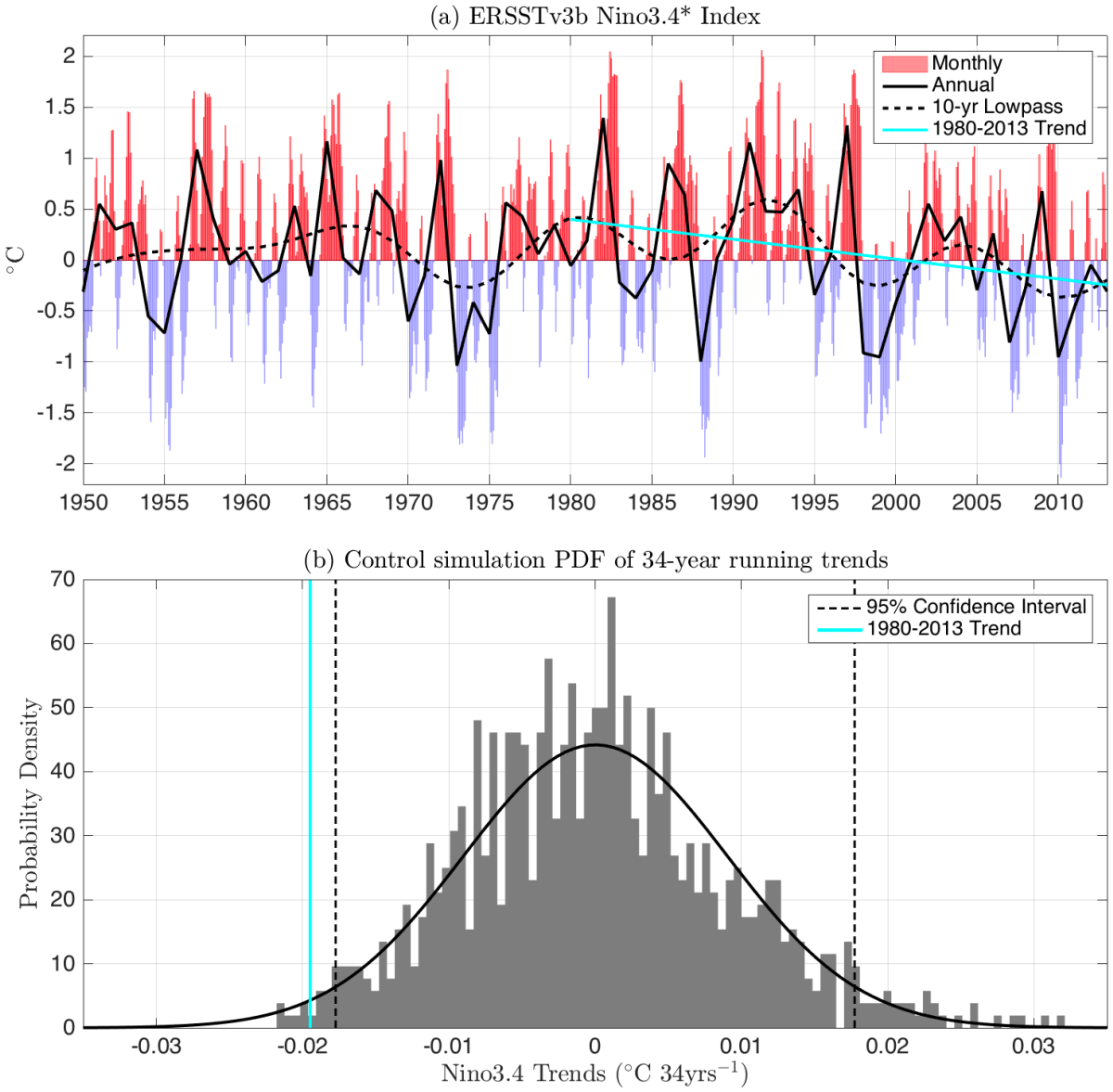

Figure 3.3: (a) Monthly mean Nino3.4* index calculated from ERSSTv3b (˚C, red/blue shading). Black solid line is the annual mean, black dashed line is the 10-year low-pass filter, and cyan line is the linear fit from 1980 to 2013. (b) Probability density function (PDF; gray shading) of 34-year running trends of Nino3.4 in a 1000-year control simulation. Black solid line following gray shading is a Gaussian distribution with the same mean and standard deviation as the PDF. Black dashed lines mark 95% confidence intervals. Vertical cyan line represents the observed trend (a). Note the height of the cyan line is arbitrary.

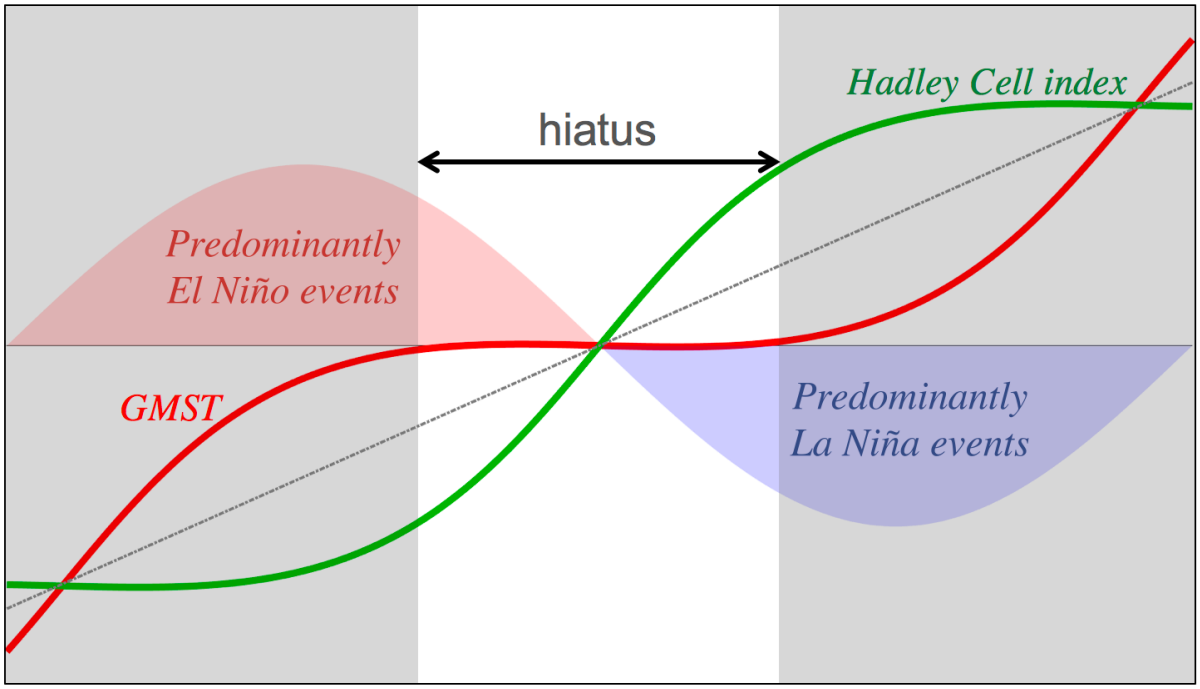

Figure 3.4: Schematic demonstrating the hypothesized interplay between anthropogenic forcings (gray dashed line) and decadal phases in the relative frequency of ENSO events (red/blue sine wave). Green line represents trajectory of a measured Hadley Cell edge index with time. Red line represents trajectory of measured global mean surface temperature (GMST) with time. During the long-term transition from a period of more El Niño events (red shading) to a period of more La Niña events (blue shading), forced global warming is dampened and the trend flattens out, producing a hiatus period. Simultaneously, the increasing prevalence of La Niña-forced Hadley Cell expansion drives accelerated widening of the tropics through an enhancement of the externally forced Hadley Cell widening.

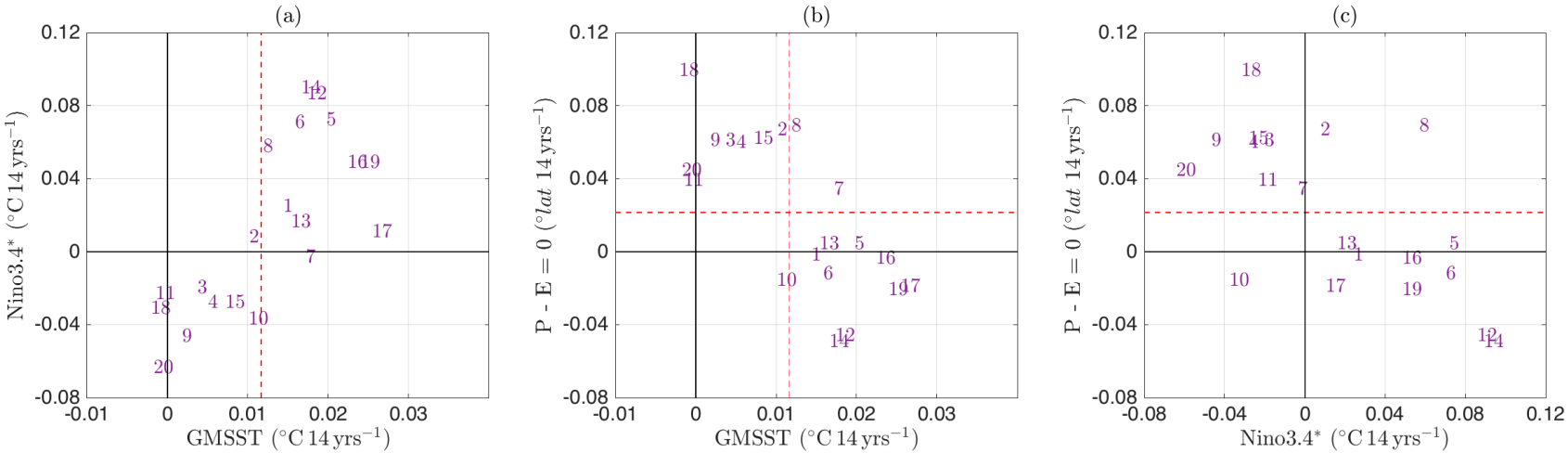

Figure 3.5: (a) Trends in Nino3.4* (˚C 14yrs^{-1}) versus trends in GMSST (˚C 14yrs^{-1}). (b) Trends in the latitude where P – E = 0 (˚lat 14yrs^{-1}) versus trends in GMSST. (c) Trends in the latitude where P – E = 0 versus trends in Nino3.4*. Every trend is calculated from 2000-2013. Different numbers represent different members of the 20-member all-forcing historical ensemble. Red dashed lines in each case are the ensemble mean trend for the corresponding axis.

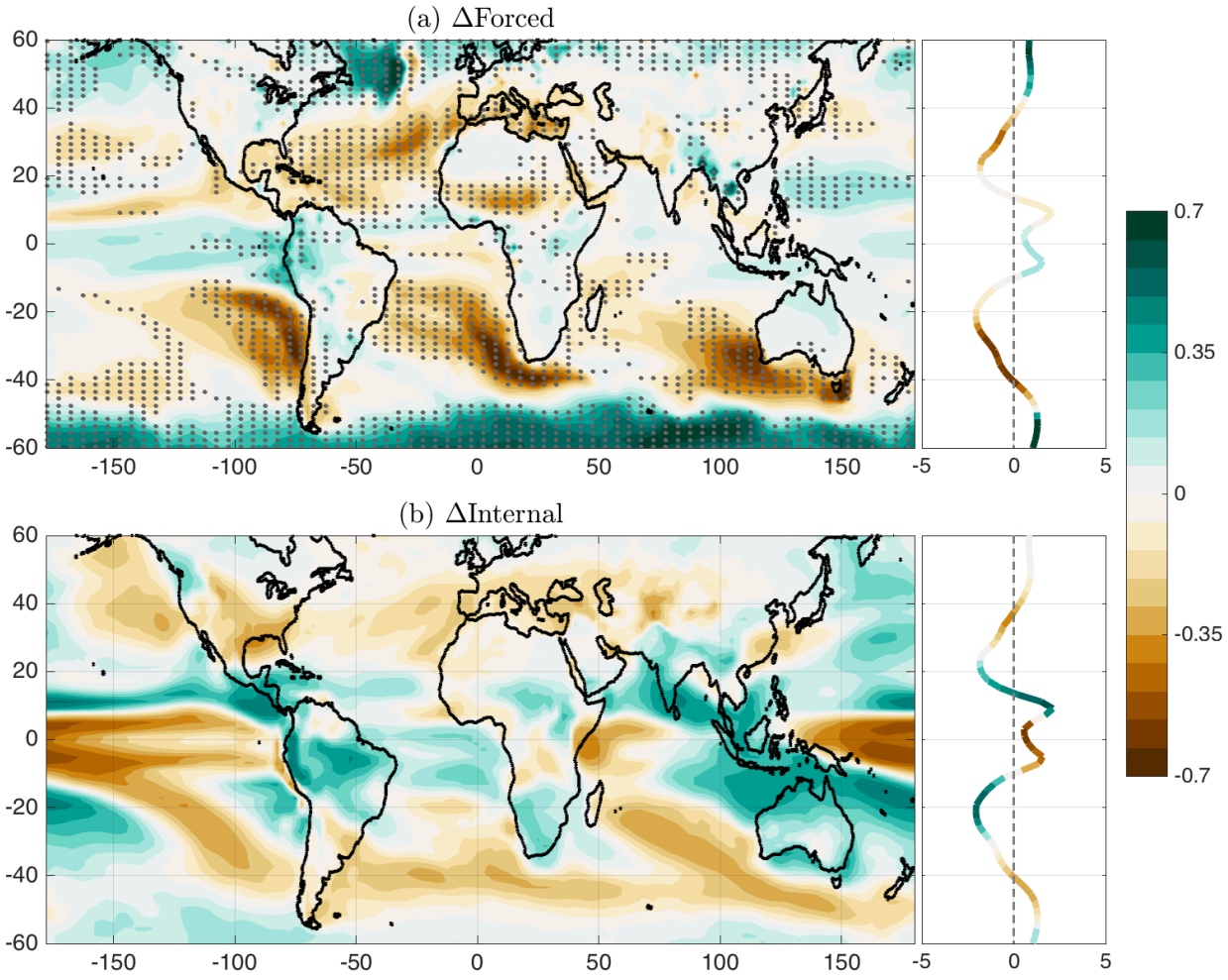

Figure 3.6: (a) Regression of ensemble mean P – E with PC_{for} scaled by change in PC_{fit} from 1980-2013. (b) Regression of control simulation P – E with PC_{in} scaled to represent a 95% confidence interval of 34-year running trends using Equation 3.2. Both patterns weighted by standard deviation of control simulation P – E anomalies at each grid point. Shape of line in each side-panel is zonal mean climatological P – E as a function of latitude. Shading of each line right of (a) and (b) represents regression of zonal mean P – E with respective PC, scaled the same as corresponding x/y map. Stippling in (a) denotes grid points where signal has emerged above the noise by 2013 (see text).

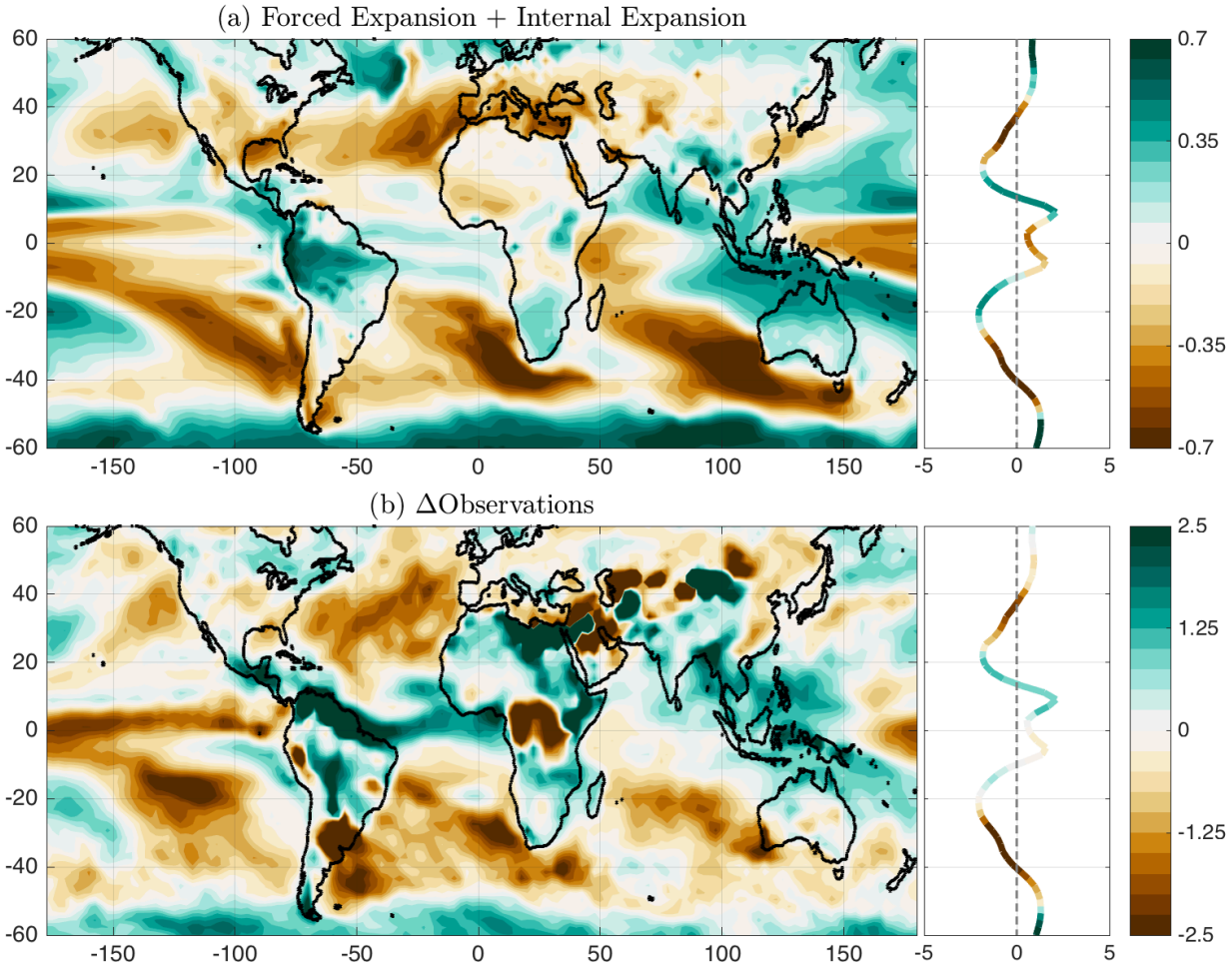

Figure 3.7: (a) The sum of Figures 3.6a and 3.6b. Figure 3.6b was first scaled by the observed change in Nino3.4* from 1980-2013 before taking the sum (see text). (b) Regression of observed annual mean P – E with composite Hadley Cell edge index from 1980-2013, scaled by the change in the composite edge index over this time period (2.27 ˚lat). Note the different colorbars. Regressions are weighted by the standard deviation of control simulation P – E anomalies at each grid point.

Chapter 4

WES Feedback and the Atlantic Meridional Mode: Observations and CMIP5 Comparisons

Abstract

The Atlantic Meridional Mode (AMM) is the dominant mode of tropical SST/wind coupled variability. Modeling studies have implicated wind-evaporation-SST (WES) feedback as the primary driver of the AMM's evolution across the Atlantic basin; however, a robust coupling of the SST and winds has not been shown in observations. This study examines observed AMM growth, propagation, and decay as a result of WES interactions. Investigation of an extended maximum covariance analysis shows that boreal wintertime atmospheric forcing generates positive SST anomalies (SSTA) through a reduction of surface evaporative cooling. When the AMM peaks in magnitude during spring and summer, upward latent heat flux anomalies occur over the warmest SSTs and act to dampen the initial forcing. In contrast, on the southwestern edge of the SSTA, SST-forced cross-equatorial flow reduces the strength of the climatological trade winds and provides an anomalous latent heat flux into the ocean, which causes southwestward propagation of the initial atmosphere-forced SSTA through WES dynamics. Additionally, the lead-lag relationship of the ocean and atmosphere indicates a transition from an atmosphere-forcing-ocean regime in the northern subtropics to a highly coupled regime in the northern tropics that is not observed in the Southern Hemisphere. CMIP5 models poorly simulate the latitudinal transition

from a one-way interaction to a two-way feedback, which may explain why they also struggle to reproduce spatially coherent interactions between tropical Atlantic SST and winds. This analysis provides valuable insight on how meridional modes act as links between extratropical and tropical variability and focuses future research aimed at improving climate model simulations.

4.1 Introduction

Interannual variability of the tropical Atlantic coupled ocean-atmosphere system is most significantly influenced by two modes of climate: the Atlantic Niño (Zebiak 1993) and the Atlantic Meridional Mode (AMM; Chiang and Vimont 2004). The Atlantic Niño is an El Niño-Southern Oscillation (ENSO)-like response to zonal movement of the equatorial thermocline, which produces anomalous sea surface temperatures (SST) and significant shifts in the Atlantic Walker and Hadley Circulations. This response is phase-locked to boreal summer and is driven by Bjerknes dynamics that are also associated with the Pacific ENSO (e.g., Zebiak 1993; Carton and Huang 2002). The Atlantic Meridional Mode involves interannual and decadal fluctuations of the interhemispheric SST gradient in the tropical Atlantic, which drives cross-equatorial boundary layer flow toward the anomalously warm hemisphere (Nobre and Shukla 1996; Chang et al. 1997). This fluctuation of the meridional SST gradient significantly modulates the seasonal march of the Intertropical Convergence Zone (ITCZ), which impacts regional rainfall over Northeast Brazil and the Sahel of Africa (Foltz et al. 2012; Xie and Carton 2004; Hastenrath and Heller 1977; Folland et al. 1986). In addition, the AMM has been shown to affect Atlantic hurricane activity (e.g., Vimont and Kossin 2007).

Several hypotheses have been proposed to explain the dynamical genesis of the AMM. Nobre and Shukla (1996) first suggested an external mechanism in which trade wind variations in

the tropical North Atlantic force SST anomalies (SSTA) through surface latent heat flux anomalies. In subsequent studies, ENSO and the North Atlantic Oscillation (NAO) were identified as examples of large-scale climate modes which can cause remotely forced and stochastically generated trade wind variations that give rise to a meridional SST asymmetry about the equator (e.g., Chiang et al. 2002; Amaya and Foltz 2014).

A second mechanism outlined by Chang et al. (1997) implicates wind-evaporation-SST (WES) feedback Xie and Philander (1994) as the major mechanism for the AMM. In this theory, cross-equatorial atmospheric flow reduces the strength of the trade winds in the warmer hemisphere and increases the strength of the trades in the cooler hemisphere due to turning by the Corolis force. This change in the magnitude of the trade winds acts to reinforce the meridional SST gradient through anomalous, opposite signed surface evaporation between hemispheres. Several studies have also indicated that tropical and subtropical low-level cloud cover anomalies can force changes in SST anomalies, and consequently affect the meridional SST gradient, due to enhanced shortwave reflection (e.g., Evan et al. 2013; Tanimoto and Xie 2004). The ITCZ, which is sensitive to variations in this meridional gradient, then follows the SST patterns and trade wind convergences into the warmer hemisphere (Chiang et al. 2002).

However, subsequent studies have shown that WES feedback is largely confined to the deep tropics and is relatively weak, requiring at least some external forcing to sustain the coupled variability and reproduce the observed AMM behavior (Chang et al. 2001; Chiang et al. 2002; Czaja et al. 2002). In particular, Chang et al. (2001) used a 145-yr simulation of an atmospheric general circulation model (AGCM) to show that stochastic forcing alone can generate significant SSTA in the tropical Atlantic north of about 15˚N, but a weak-to-moderate local air-sea coupling is needed to reproduce observed tropical Atlantic variability south of this latitude.

In spite of the many advances made by these studies, there is still widespread uncertainty regarding the role of WES feedback in exciting and sustaining the AMM. Chang et al. (2001) presented observational evidence in support of the WES feedback theory based on a lagged correlation analysis between different time series in a maximum covariance analysis (MCA). Similarly, Sutton et al. (2000) and Okumura et al. (2001) examined the AMM in a modeling framework and found a negative and slightly positive WES feedback, respectively, through model analysis, while Ruiz-Barradas et al. (2003) showed a positive feedback throughout the north tropical Atlantic, except off the coast of Africa. These studies were primarily based on the outputs of AGCMs, which can produce different feedback strengths among models (Frankignoul et al. 2004). Wary of model uncertainty, Frankignoul and Kestenare (2005) conducted a study based on observational reanalysis data aimed at revisiting air-sea coupled interactions in the tropical Atlantic. They showed that boreal winter trade wind anomalies north of approximately 10˚N off the coast of Africa can generate initial SSTAs through anomalous latent heat fluxes, which are then sustained in the deep tropics by positive WES feedback.

Very few studies have investigated how initial stochastically forced SST anomalies in the subtropics evolve into a fully coupled ocean-atmosphere thermodynamic mode in the deeper tropics. Such an analysis would complement many of the previous investigations mentioned here, which focused on the AMM/WES feedback relationship in the context of mechanistic generation and sustention. WES feedback theory suggests that a positive SST anomaly will propagate southwestward due to the tendency of SST-forced surface wind anomalies to weaken (strengthen) the climatological trade winds on the southwestern (northeastern) edge of the SST anomaly, potentially providing the link from subtropical origins to deep tropical growth and decay (Xie 1999).

In the Pacific, Vimont et al. (2001, 2003) expanded upon this idea and proposed a seasonal footprinting mechanism by which mid-latitude atmospheric variability during boreal winter could potentially force a subtropical SST anomaly that would then propagate through WES feedback to the equatorial Pacific in the summer and influence zonal surface wind and SST variability. Subsequent modeling efforts by Vimont (2010), Vimont et al. (2009), and Wu et al. (2010) confirmed that WES feedback could indeed propagate subtropical Pacific SSTAs southwestward toward the Central Pacific, though in some cases over much faster timescales than originally proposed. These results have informed recent studies which indicate that the AMM and its Pacific counterpart (the Pacific Meridional Mode, PMM) may act as conduits by which extratropical atmospheric variability can significantly influence equatorial SST variability, thereby exciting Atlantic Niño and Pacific ENSO events through this WES-driven propagation (Vimont et al. 2003b; Foltz and McPhaden 2010; Alexander et al. 2010; Larson and Kirtman 2014; Di Lorenzo and Mantua 2016).

While the WES driven propagation of anomalies associated with the PMM has been well studied over recent years, there remains little observational evidence of a similar mechanistic evolution of the AMM. In this study, we use observations to synthesize the results outlined by the previous literature and paint a consistent and cohesive picture of WES dynamics in the tropical Atlantic as they pertain to AMM generation, propagation, and decay. We then use this new observational insight to test the performance of models included in phase 5 of the Coupled Model Intercomparison Project (CMIP5) in simulating AMM structure and the physical mechanisms associated with the AMM's propagation. While individual CMIP5 models have been used to evaluate the physical mechanisms governing AMM variability, a full comparison of a suite of CMIP5 models has not been investigated. Our observational and model results bring together

nearly two decades of research in tropical Atlantic coupled variability and could potentially increase predictability and prediction skill of the AMM in future modeling efforts, benefiting socioeconomic endeavors in coastal Atlantic countries that are affected by interannual climate variability.

In the following section, we outline the observational data sets employed in our study, as well as the specifications for the CMIP5 models being evaluated. Sections 4.3 and 4.4 consist of our observational analysis of the AMM's spatiotemporal evolution. In Section 4.5, we repeat the analysis performed in Sections 4.3 and 4.4, but for a suite of CMIP5 models. Section 4.6 contains a summary and accompanying discussion of our results.

4.2 Data and methods

We characterize tropical Atlantic SST variability using monthly mean data from the National Oceanic and Atmospheric Administration's Extended Reconstructed Sea Surface Temperature Version 3b (NOAA ERRST.v3b), which is available from 1854-present (Smith et al. 2008). We limit our analysis to 1950-2015, since the spatial density of SST data increased significantly during this period. Monthly mean 10-meter wind and net surface latent heat flux data are obtained from the National Centers for Environmental Prediction-National Center for Atmospheric Research (NCEP-NCAR) Reanalysis (Kalnay et al. 1996), also from January 1950 to December 2015. We find that our results are largely insensitive to the choice of a particular reanalysis product.

We investigate tropical Atlantic coupled variability by applying a maximum covariance analysis (MCA; Bretherton et al. 1992) between SST and both components of the 10-meter horizontal wind. MCA is analogous to empirical orthogonal function (EOF) analysis, but performs

the singular value decomposition on the cross-covariance matrix between the variables. The resulting expansion coefficients (ECs) associated with the left and right singular vectors can then be projected onto the original data to obtain homogeneous and heterogeneous regression maps. The MCA results in this study show the homogeneous SST structure and the heterogeneous surface horizontal wind structure, so that both regressions are the result of the same time variability.

The AMM spatiotemporal evolution is examined using an extended MCA (EMCA) technique, which incorporates time-lagged information, similar to the technique used by Frankignoul and Kestenare (2005) and Polo et al. (2008). The EMCA methodology is largely similar to MCA, but differs in that seasonally averaged time series of SST and 10-meter wind anomalies are stacked before computing the cross-covariance matrix, such that December-February (DJF) averaged maps are on top of March-May (MAM), June-August (JJA), and September-November (SON) averaged maps. Thus, if the data initially had dimensions of $N \times M$, where N is the time dimension and M is space, it has dimensions $N \times 4*M$ after concatenating the matrices. The cross-covariance matrix is then calculated and the singular value decomposition is performed on this new matrix. EMCA yields four spatial structures per variable which are lagged in time, but are all described by a single EC.

Model evaluation is based on historical simulations of 17 CMIP5 models. The modeling centers and countries, CMIP5 model abbreviations, and the number of runs for each model used in this study are shown in Table 4.1. Monthly mean SST, 10-meter winds, and net surface latent heat flux were used from 1950-2005 for each model. For brevity we show only the multi-model mean results. The MCA and various regressions were performed for each model separately and the average spatial pattern for the respective variables was taken to be the multi-model mean. For models with multiple ensemble members, each member was stacked in time such that the stacked

array would have dimensions of *N*(number of ensembles) x M*. The MCA and other analyses were then calculated based on this expanded matrix.

Prior to MCA analyses, all fields are linearly detrended. Data used to calculate Figure 4.1 are smoothed with a 3-month running mean at each grid point. Additionally, we remove the linear influence of ENSO on tropical Atlantic coupled variability by regressing out the cold tongue index (CTI; 6°N-6°S, 180°W-90°W) from each field at each grid point for data used in Figures 4.1-4.3 and Figures 4.5-4.7. Monthly anomalies in the observational analysis are relative to the climatology 1986-2015, while CMIP5 evaluations are relative to 1976-2005.

4.3 AMM propagation in observations

Following Chiang and Vimont (2004), we first apply MCA analysis to observed SST and 10-meter winds in the domain 32˚N-22˚S and 74˚W to the African coastline. The leading mode of tropical Atlantic coupled SST/wind variability is shown in Figure 4.1a, while the normalized ECs, which describe the time variability of the leading spatial modes, are shown in Figure 4.1b. The squared covariance fraction for the leading mode is 66% and the correlation coefficient of the two ECs is 0.72, indicating strong coupling of SST and winds in this region.

The leading mode of covariability in the tropical Atlantic is the AMM (Figure 4.1a). There is a strong interhemispheric asymmetry in SSTA spatial loading, with positive values in the Northern Hemisphere (NH) and lower magnitude negative values in the Southern Hemisphere (SH), which is consistent with previous results (e.g., Chiang and Vimont 2004). From approximately 25˚N to 5˚N, strong southwesterly wind anomalies are co-located with the strongest SSTAs, centered at about 20˚W. There are also cross-equatorial winds that begin as southeasterly flow just south of the equator, turning to southwesterly flow just north of the equator. This C-shape

bend in the winds about the equator is a distinct signature of WES feedback and will be analyzed in more detail in Section 4.4.

The ECs depicted in Figure 4.1b vary on interannual to multidecadal timescales. In particular, the low-frequency component of the AMM ECs is reminiscent of the Atlantic Multidecadal Oscillation (AMO) index, which is well-correlated with both the SST and wind ECs (0.72 and 0.46 correlation coefficients, respectively). The surface wind variability associated with the AMM peaks in late boreal winter, while the SSTA structure peaks in the spring (Figure 4.1c). Atmospheric variability leading SSTA variability by about a season is generally consistent with stochastic atmospheric forcing of a subsequently sustained SST anomaly (e.g., Chang et al. 2001).

MCA extracts the leading mode of coupled variability between the input variables, independent of the temporal evolution of the mode itself. Consequently, the mode depicted in Figure 4.1a spans the entire AMM life cycle and consolidates its genesis, growth, and decay into one single mode (Chiang and Vimont 2004). To isolate these individual stages of the AMM, we compute the leading EMCA (see Section 4.2) mode of the SSTA and 10-meter surface winds (Figure 4.2). The squared covariance fraction for this mode is 49% and the correlation of the left and right ECs is 0.9. The observed surface latent heat flux was then regressed onto the resulting SST EC depicted in Figure 4.2e, and the results are shown in Figure 4.3. In Figures 4.2 and 4.3, the SSTA are contoured in black and the 0.3˚C contour is outlined in green. The convention for latent heat flux anomalies in Figure 4.3 is such that a positive (negative) anomaly corresponds to an upward (downward) energy flux and a cooling (warming) of the ocean.

In DJF, there are strong westerly surface wind anomalies in the NH subtropics from 32˚N-20˚N (Figure 4.2a). These surface wind anomalies lie on the northern edge of a band of positive SSTAs that runs from the west coast of Africa to the north/northeast coast of South America. A

localized maximum in SSTA can be seen centered on 15˚N, 18˚W (green contour). In Figure 4.3a, we observe three distinct forcing regimes that give rise to the SSTAs described in Figure 4.2a. The first regime is characterized by a tongue of negative latent flux anomalies extending from 20˚N-10˚N and 60˚W-20˚W. These anomalies increase in magnitude going from west-to-east toward more positive SSTAs (black contours) and are generally co-located with strong westerly surface wind anomalies at 20˚N. This co-location is consistent with boreal wintertime atmospheric forcing associated with NAO variability which reduces the strength of the background trade winds in the NH, thereby reducing evaporative cooling at the surface and driving an anomalous flux of latent energy into the ocean.

The second forcing regime is associated with cross-equatorial flow that turns southwesterly in the NH, driving negative latent heat flux anomalies that extend from 20˚N to the equator at around 30˚W (Figures 4.2a and 4.3a). These anomalies are found on the southwest edge of the SSTA warm pool and are an early indication of air-sea interactions associated with WES feedback. The final regime is centered on the SSTA maximum outlined by the green contour. Here, southwesterly anomalies oppose the climatological upwelling favorable winds along the African coastline, which may weaken coastal upwelling and provide a latent heat flux which dampens co-located SSTAs. A flux of energy into the ocean on the west/southwest edge of the SSTA warm pool coupled with a near zero latent heat flux in the center of the SSTA maximum would lead to a propagation of the SSTA west/southwestward in the following season, representing AMM genesis.

The leading mode of SST and wind covariability during MAM (Figure 4.2b) is much more pronounced in magnitude and spatial extent. Consequently, the MAM spatial structure most closely resembles the spatial structure of the “all-months” AMM shown in Figure 4.1a. The NAO-like forcing regime seen in DJF appears to have weakened significantly in the NH subtropics with

near zero flow over the warmest SSTAs. The SSTA maximum has extended southwest as far as 60˚W, which is consistent with the energy fluxes observed in DJF (Figure 4.2b, green contour). Despite this propagation, the local SSTA maximum in MAM is still located just off the coast of Africa and is likely due to the persistence of stochastic atmospheric forcing throughout boreal winter into early spring. In addition, the WES feedback regime has enhanced significantly as the weak cross-equatorial flow seen in DJF has increased in magnitude and extended across the basin west of 15˚W in MAM. This anomalous boundary layer flow is southeasterly from 0˚-10˚S and southwesterly from 0˚-10˚N and is representative of a locally driven ocean-forced response in the surface winds (Figure 4.4). The exact nature of the transition to an ocean-forced wind change as a function of latitude will be described in Section 4.4.

The regression of latent heat flux anomalies onto the SST EC shows negative values (ocean warming) that are closely co-located with the 0.3˚C green contour and the most significant southwesterly wind anomalies (Figure 4.3b). In contrast, there are very weak surface wind anomalies and positive latent heat flux anomalies over the warmest SSTA anomalies (marked by the 0.4˚C and 0.5˚C contours; Figures 4.2b and 4.3b). These localized positive latent heat flux anomalies are likely due to warm SST generating small-scale convection, which would lift warm air from the boundary layer and act as a damping on the SSTAs in the region. This zonal dipole of latent heat flux anomalies is consistent with WES feedback theory and illustrates the competition between atmosphere-forced temperature change and Newtonian cooling in the evolution of SSTAs that lie on the subtropical/tropical boundary (e.g., Xie 1999).

During JJA, the maximum SSTA propagates further southwestward and is now centered at 12˚N, 50˚W (Figure 4.2c). There is continued evidence of a WES feedback from 10˚N-5˚N and 50˚W-40˚W, as anomalous southwesterly flow and negative latent heat flux anomalies are co-

located with the southwestern edge of the SSTA maximum (green contour, Figure 4.3c). However, in the absence of sustained atmospheric forcing, the SSTAs off the coast of Africa that were seen in DJF and MAM have weakened substantially due to the cooling associated with a continued upward flux of latent energy in that region (Figure 4.3c).

Are the upward latent heat flux anomalies seen in MAM strong enough to account for the ~0.3˚C cooling observed from MAM to JJA near the African coast? A qualitative heat budget analysis can be analyzed to investigate the contribution of the latent heat flux to the mixed layer temperature change in this region. The change in SST from MAM to JJA, ΔSST, can be estimated as:

$$\Delta SST = \frac{\Delta t * Q_{LH}}{\rho C_p h} \tag{4.1}$$

Where the change in time, Δt, is three months, ρC_p= 4.088 x 10^6 J K^{-1} m^{-3} (Cronin et al. 2013), and $h \approx$ 30m (Foltz et al. 2013). The average latent heat flux, Q_{LH}, during MAM is -3.8 W m^{-2} (negative because it is an energy gain for the atmosphere, but an energy loss for the ocean) from 20˚N-10˚N, 30˚W-15˚W. Using Equation 4.1, we get an estimated $\Delta SST \approx -0.24^{\circ}C$, which corresponds well to the average ΔSST in that same box of -0.25˚C (not shown). The consistency of this rough estimate, based on a simple mixed-layer model approximation, is somewhat surprising when considering the potential impact of stratocumulous cloud and African dust forcing on SSTA via surface shortwave radiation in this region (e.g., Evan et al. 2013; Deflorio et al. 2014). Therefore, while this preliminary calculation indicates that latent heat flux anomalies represent the main contribution to SST change from MAM to JJA, this may not necessarily be true for all of the north tropical Atlantic or for all seasons given that the mixed layer depth can vary in time and space by as much as 40m (Foltz et al. 2013) and given the significant impact of other regional forcing terms on SSTAs (e.g., Evan et al. 2013; DeFlorio et al. 2014).

The anomalous surface flow and associated latent heat flux anomalies in SON are harder to interpret, as they are less spatially coherent and are not physically consistent with the temporal evolution of the AMM from DJF to JJA (Figures 4.2d and 4.3d). However, the SON SSTA structure remains physically consistent with the energy fluxes from the previous season as the maximum SSTA propagates into the South American coastline and the SSTA spanning the rest of the basin decays further.

It should be noted that the physical mechanisms for SSTA growth, propagation, and decay described above were limited to the tropical North Atlantic region. The covariability in the tropical South Atlantic region does not evolve similarly and largely maintains southeasterly flow, negative SSTA, and positive latent heat flux anomalies throughout the year. The SH lobe of the AMM has been shown to be statistically independent of the NH lobe (e.g., Mehta and Delworth 1995; Enfield and Mestas-Nuñez 1999). Therefore, the spatiotemporal evolution of SH SSTA may be found in a higher order EMCA mode, or it may materialize if a different EMCA domain was chosen to emphasize SH coupled variability. We encourage future studies to further describe and understand this distinction.

4.4 Transition from atmosphere forcing ocean to ocean-atmosphere coupling

In Section 4.3, we used observations to demonstrate the importance of WES feedback in sustaining and propagating SSTAs from subtropical latitudes to the deep tropics. This process is dependent on the ocean's ability to force sufficiently strong low-level wind anomalies, which then feedback and significantly enhance the local SSTA. Without this ocean-atmosphere coupling, model analysis suggests that an SSTA generated at subtropical latitudes by stochastic atmospheric

variability will not grow or propagate into tropical latitudes and become an AMM event (Chang et al. 2001; Chiang et al. 2002; Czaja et al. 2002). Therefore, it is of interest to empirically identify the latitudes at which the climate regime shifts from atmosphere-forcing-ocean to full ocean-atmosphere coupling. Such an analysis would improve our understanding of where air-sea coupling occurs in the tropical Atlantic and may demonstrate to what extent the AMM acts as a connection between extratropical atmospheric variability and equatorial SST variability.

To help characterize this regime shift, we propose a symmetry index based on the lag correlation structure of Atlantic zonal mean SSTA and surface wind anomalies as a function of latitude. The more symmetric the lag correlation structure between the two variables, the greater the evidence for ocean-atmosphere interactions at that latitude. In contrast, strong asymmetries would be indicative of a one-way communication between the SST and surface winds. We calculate this symmetry index for zonal mean SST/U-wind anomalies and zonal mean SST/V-wind anomalies, respectively (Figures 4.4a and 4.4b). Select lag correlations at 20˚N (blue), 10˚N (yellow), and 10˚S (red) are shown in Figure 4.4c. Stippling in Figures 4.4a and 4.4b and the bold parts of the curves in Figure 4.4c indicates statistical significance at 95%, which is based on the e-folding timescale of the autocorrelation function of the zonal mean SSTA at each latitude. The lags on the x-axis of each plot are in months.

Significantly negative correlations between SSTA and wind anomalies exist at 50˚N-45N˚ when the wind leads by 0 to 2 months for SST/U-wind and 0 to 5 months for SST/V-wind. A similar lobe of significantly negative correlations for SST/U-wind is found at southern mid-latitudes, while SST/V-wind has positive correlations at positive lags that are not statistically significant. These four mid-latitude lobes are consistent with an atmosphere-forcing-ocean climate regime (e.g., Alexander and Scott 1997) in which positive SSTAs are locally generated as a result

of northerly and easterly wind anomalies in the NH and southerly and easterly wind anomalies in the SH.

Similar lag-lead relationships are evident in NH subtropical latitudes (30˚N-20˚N, Figure 4.4). In this region, significant positive correlations can be found between SST and both components of the wind at lags ranging from 0 to 6 months. The lag correlation sign change is consistent with a shift in the background wind state from mid-latitude westerlies to the northeasterly trade winds. The increase in the number of significant lags going southward from 30˚N to 20˚N is also likely due to this gradual shift from westerly to northeasterly flow. The magnitude of the background flow is weak at 30˚N compared to 20˚N, thus we would expect a weaker SSTA response for a given wind perturbation at 30˚N relative to 20˚N. This atmosphere-forcing ocean regime is consistent with NAO variability driving SST changes through surface heat fluxes (e.g., Chang et al. 2001).

For the deep tropical region of 20˚N-0˚, the lag correlation structure for the SST and both wind components are much more symmetric. In particular, significant positive correlations occur at large negative lags (when SSTAs lead wind anomalies) in a narrow meridional band ranging from 10˚N-6˚N, where SST/U-wind has a significant correlation at all lags and SST/V-wind has a significant correlation at lags of –5 to 8 months. The tails at large negative *and* positive lags at these latitudes are remarkably consistent with the most significant southwesterly surface winds and negative latent heat flux anomalies found on the southwestern edge of the warm pool (green contour) depicted in Figures 2b and 3b. Such symmetry in the lag correlation structure provides further evidence that air-sea interactions like WES feedback are significant contributors to SST and wind variability at these latitudes. The transition from an atmosphere-forcing-ocean environment to a two-way interaction is further highlighted by the select lag correlations depicted

in Figure 4.4c. The lag correlation at 20˚N (blue) peaks at a lag of 1 month and drops sharply to zero for short negative lags, whereas the lag correlation at 10˚N (yellow), although it also peaks at a lag of 1, has much stronger and more significant lag correlations at long negative lags.

The symmetrical lag correlation structures for SST/U-wind from 4N˚-4˚S may be associated with Bjerknes feedback processes and the Atlantic Niño mode. Therefore, it is difficult to assess to what degree WES feedback dynamics contribute to the structure in this region. Additionally, although the SST/V-wind lag correlation structure near the equator is less likely to be impacted by Atlantic Niño, the climatological background wind here is usually small, so a meridional wind perturbation is less likely to produce a significant SSTA via WES interactions. This may explain why the SST/V-wind correlation is either zero or insignificantly negative from 4˚N-0˚.

In the subtropics and deep tropics of the SH, the lag correlation structures for both SST/U-wind and SST/V-wind do not show a similar transition from atmosphere-forcing-ocean to ocean-atmosphere coupling compared to the NH. In particular, significant correlations between SST and U-wind only exist at positive lags from 6˚S-30˚S, and at all southern latitudes for SST and V-wind. This relationship is emphasized by the 10˚S curve (red) in Figure 4.4c, which more closely resembles the northern subtropics than the northern tropics, albeit with weaker correlation values. The absence of significant correlations when the SST leads the wind in the SH tropics is puzzling and will be discussed in greater detail in Section 4.6.

4.5 CMIP5 evaluation

Tropical Atlantic coupled variability has not been extensively evaluated in CMIP5 models, with several exceptions. (Liu et al. 2013) evaluated Atlantic warm pool variability in the historical

simulations of 19 CMIP5 models, but stopped short of assessing the model's ability at reproducing coupled variability. Richter et al. (2014) analyzed CMIP5 model mean states and determined they exhibit too weak easterlies, and that the ITCZ is typically too far to the south. Given the significant impact of tropical Atlantic coupled variability on regional atmospheric circulation and precipitation, it is vital to assess the dexterity of CMIP5 models in reproducing observed coupled variability. Here, we repeat the observational analysis outlined in Sections 4.3 and 4.4 on a suite of 17 CMIP5 models (Table 4.1). For brevity, we present only the results of the multi-model mean.

The multi-model mean AMM and the multi-model mean monthly variance of the respective ECs are shown in Figure 4.5. It is important to note that unlike in observations, the leading mode of coupled variability in the CMIP5 models is not always the AMM. Therefore, to objectively determine the AMM mode for each model, we use a pattern correlation to compare the first five SSTA modes of the model MCA analysis to the observed AMM SSTA structure shown in Figure 4.1. The model MCA mode with the highest pattern correlation was then selected to be the model's representation of the AMM and was included in the multi-model mean. A similar technique was used for the CMIP5 EMCA (Figure 4.6), except the model AMM mode was found by comparing only the MAM SSTA structure between the models and observations. The mode number, the squared covariance fraction explained by each model's AMM, and the pattern correlation coefficient of each model's AMM with the observations for the CMIP5 MCA and EMCA analyses are listed in Table 4.2.

On average, the model AMM explains 35% of the covariance between tropical Atlantic SST and surface winds, which is only about half of the squared covariance fraction seen in the observations (Figures 4.1 and 4.5). The observed large-scale spatial structure of the AMM is generally well-reproduced in the CMIP5 models (Figures 4.1a and 4.5a). There is a distinct

interhemispheric SSTA gradient with a northeastward tilted warm lobe in the NH and general cooling in the SH. Additionally, surface wind anomalies are primarily southwesterly in the NH and southeasterly in the SH, with weak cross-equatorial flow. However, on average, the models generally underestimate the magnitude of the SSTAs, the meridional SSTA gradient, and the surface wind anomalies. This underestimation was also evident in CMIP3 models and could be related to well-known cold (warm) Atlantic SST biases in the NH (SH) (Liu et al. 2013).

Inspection of the multi-model mean month-to-month variance shows that the models reproduce the wind variability peak in January-February with reasonable accuracy. However, the multi-model mean wind variance is notably higher in boreal spring, while the observational variance declines sharply in March and April (Figures 4.1c and 4.5b). Additionally, the models poorly simulate the observed peak of SST variability in the tropical Atlantic during MAM (Figures 4.1c and 4.5b). Instead, the SST variance is lowest in boreal winter and roughly constant throughout the rest of the year. This discrepancy could be the result of a double ITCZ bias observed in CMIP5 models in the Atlantic Richter et al. (2014). An incorrect representation of the lead-lag relationship of the atmosphere and ocean associated with the AMM may contribute to the inaccuracies seen in Figure 4.5a. Further, inspection of power spectra based on each model's SST EC reveals that the models generally reproduce the observed interannual variability associated with the AMM, but tend to have more power at lower frequencies than seen in observations (not shown).

The multi-model mean EMCA of SSTA and surface winds is shown in Figure 4.6, and the multi-model mean latent heat flux regression on to the respective EMCA SSTA ECs is shown in Figure 4.7. Note that the green contour in Figures 4.6 and 4.7 now represents the 0.2˚C contour. Similar to Figure 4.5a, the CMIP5 models do a credible job in reproducing the observed genesis

of the AMM SSTA structure, but the SSTA and wind anomaly magnitudes are once again underestimated (Figures 4.2 and 4.6). Additionally, the multi-model mean latent heat flux regression in DJF does not show the presence of the three distinct forcing regimes seen in observations (Figures 4.3a and 4.7a). Instead, there are basin-wide negative latent heat flux anomalies from about 20˚N-0˚ that are most consistent with the NAO-like forcing regime depicted in Figure 4.3a, though they are much weaker than in observations (note the change in the color bar).

In MAM, the multi-model mean AMM peaks in strength, consistent with large negative latent heat flux anomalies seen in the previous season throughout the north tropical Atlantic from 20˚N-0˚. These widespread negative latent heat flux anomalies have persisted into MAM, though they are weaker than in the winter. This broad swath of negative latent heat flux anomalies is also consistent with the NAO-like forcing regime and could be associated with the models producing springtime atmospheric forcing that is too large compared to observations, as indicated by the month-month variance analysis (Figure 4.5b). Simultaneously, there is evidence of a weak ocean-atmosphere coupling with negative latent heat flux anomalies on the southwest edge of the warmest SSTAs and near-zero or slightly positive anomalies in the SSTA maximum (Figures 4.6b and 4.7b). In the SH deep tropics, positive latent heat flux anomalies are co-located with negative SSTAs. These deep tropical latent heat flux anomalies in the model are consistent with being forced by model wind anomalies, which are southwesterly in the NH (albeit very weak) and southeasterly in the SH. Cross-equatorial flow also peaks during this season.

During JJA, the multi-model mean shows hints of seasonal SSTA propagation as indicated by the SSTA maximum outlined in green. However, it is clear from comparing Figures 4.2b,c with Figures 4.6b,c that the SSTA expansion from MAM to JJA is much less striking than in nature.

The models' inability to reproduce significant SSTA propagation could be due to the fact that the most intense latent heat flux anomalies in the NH during MAM are found much closer to the equator and much further away from the edge of the SSTA warm pool relative to the observations. As a result, significant latent heat flux-driven SST change at the edge of the SSTA maximum may not occur, which would limit SSTA propagation in the models for the following season. Thus, while the multi-model mean representation of the AMM spatial structure is qualitatively consistent with observations shown in Figures 4.2b and 4.3b, it is clear that the models' representation of the physical processes that govern WES feedback are not as spatially coherent.

It is also important to note that during JJA, the broad scale negative latent heat flux anomalies seen in the previous two seasons in the north tropical Atlantic have been replaced with nearly basin wide positive latent heat flux anomalies. The month-to-month surface wind variance analysis shows a marked decrease in magnitude during boreal summer. Thus, a reduction in atmospheric forcing in the absence of a robust WES feedback would allow for broad cooling of warm SSTAs associated with the model AMM, consistent with these broad upward latent heat flux anomalies (Figures 4.5b and 4.7c).

Additionally, the multi-model mean EMCA shows a tongue of cold SSTAs on the equator in JJA that is not present in the observations. These cold anomalies are coupled with a zonal dipole of latent heat flux anomalies that is inconsistent with the cross-equatorial surface wind anomalies seen in Figures 4.6c and 4.7c. The model latent heat flux response being more tightly confined to the equator is not simply the result of the multi-model mean smoothing over more varied behavior, but is a feature that exists in nearly all of the models (not shown). It is possible that the summertime EMCA in the models is being contaminated by overestimated Atlantic Niño variability or by the

propensity for CMIP models to produce AMMs that have spuriously strong interactions with the Atlantic Niño (e.g., Breugem et al. 2006; Richter et al. 2014; Zebiak 1993).

The multi-model mean lag correlation between zonal mean SSTA and both wind components in the Atlantic as a function of latitude is shown in Figure 4.8. The models credibly reproduce the SST/U-wind and SST/V-wind lag correlation structure at high latitudes. At both northern and southern mid-latitudes, the lag correlation is asymmetrical in favor of atmosphere forcing the ocean for the U-wind and V-wind, which is consistent with the observations (Figures 4.4 and 4.8). From 30˚-20˚ in both hemispheres, the modeled correlations continue to be realistic, and are consistent with stochastic atmospheric variability generating SST anomalies.

For SST/U-wind, the multi-model mean lag correlation structure and the observed lag correlation structure are dissimilar in the deep tropics. On average, the CMIP5 models do not accurately reproduce the observed transition from an asymmetrical atmosphere-forcing-ocean regime to a more symmetrical ocean-atmosphere coupled regime (Figures 4.4a and 4.8a). Instead, the correlations from 10˚N-0˚ become negative when the SST leads the winds, which is inconsistent with WES feedback processes. This is perhaps unsurprising given the models' difficulty in reproducing the observed spatial coherence of the latent heat and surface wind anomalies from season to season (Figure 4.7). In contrast, the models tend to credibly simulate the lag correlation structure between the SSTAs and anomalies in the V-wind (Figures 4.4b and 4.8b). Since the climatological surface winds at these latitudes are primarily zonal, perturbations in the U-wind component drive the most significant SSTA anomalies through WES dynamics (Xie 1999). Therefore, the inability of the CMIP5 models to reproduce the observed SST/U-wind lag correlation symmetry in the deep northern tropics may indicate that the models are incorrectly simulating air-sea coupling in this region. If the models are not producing a realistic WES

interaction between the SST and the U-wind component, then this may help explain the poorly simulated propagation of SSTAs seen in Figures 4.6 and 4.7.

4.6 Summary and discussion

In this study, the spatiotemporal evolution of SST and wind coupled variability in the tropical Atlantic was analyzed using observations and CMIP5 models. We confirm that the leading mode of observed coupled variability in the tropical Atlantic is the AMM, which explains 66% of the covariability. EMCA of seasonally stacked SST and surface wind anomalies was then utilized to depict a consistent and cohesive evolution of tropical Atlantic SSTAs from one season to the next in observations. In DJF, SSTAs are primarily forced by strong southwesterly surface wind anomalies, which reduce the strength of the background trade winds and reduce evaporative cooling at the surface, thereby warming the underlying ocean surface.

The regression of latent heat flux anomalies onto the EMCA SST EC during boreal spring provides evidence of air-sea coupling, and shows that the magnitude of the AMM peaks during this season. Additionally, near-zero surface wind anomalies and positive latent heat flux anomalies act as a damping on the warmest SSTAs, while strong southwesterly wind and negative latent heat flux anomalies are found along the southwest edge of the SSTA warm pool. This zonal dipole of latent heat flux and surface wind anomalies is consistent with WES feedback theory (e.g., Xie 1999). As a result of these energy fluxes, the SSTA maximum is driven southwestward into the South American coast during boreal summer and autumn.

A symmetry index based on the lagged temporal correlation between zonally averaged surface wind components and SST was then created to investigate the latitude at which tropical Atlantic air-sea coupling and WES feedback processes become the dominant mechanisms in

driving SSTAs and surface wind anomalies. We show that the lag correlation structure at high latitudes is consistent with a white-noise atmosphere forcing strong SSTAs at positive lags. In the northern subtropics (30˚N-20˚N), the lag correlation structure is also dominated by an atmosphere-forcing-ocean regime. Further inspection of the northern deep tropics shows a smooth transition to more symmetric lagged temporal correlations, which is indicative of strong air-sea coupling. In particular, we identify a narrow region from 10˚N-6˚N as having the most symmetrical lag correlations, which may indicate that air-sea interactions like WES feedback play the largest role in generating and maintaining SSTAs and surface wind anomalies at these latitudes.

We then evaluated the representation of tropical Atlantic coupled variability in a suite of CMIP5 models. The AMM spatial structure from the multi-model mean of the CMIP5 models is generally consistent with observations (Figure 4.5). However, the models underestimate the magnitude of SST, surface wind, and latent heat flux anomalies throughout the basin. The model AMM errors could be a function of well-known SST biases throughout the tropical Atlantic (Richter et al. 2014; Liu et al. 2013), spurious relationships with Atlantic Niño (Breugem et al. 2006), or may perhaps be the result of issues in simulating the observed transition from an asymmetrical atmosphere-forcing-ocean environment to a more symmetrical ocean-atmosphere coupled environment.

In particular, the multi-model mean EMCA does not show a realistic southwestward propagation of the north tropical Atlantic SSTA maximum, which could be the result of the model's inability to correctly represent the spatial coherence of the physical processes governing WES feedback. As such, the ability of the average CMIP5 model to produce an AMM-like SSTA structure at all could be more due to boreal spring atmospheric forcing being too vigorous in the models (Figures 4.1c and 4.5b). These overly strong westerly surface wind anomalies in spring

may help explain the widespread negative latent heat flux anomalies seen in the models for DJF and MAM as well as the persistence of AMM-like SSTAs from one season to the next in spite of poorly representing WES feedback (Figures 4.6 and 4.7). It should be reiterated that these conclusions are drawn from the results of the multi-model mean analysis, and that investigations into individual model performance and mean state biases should be pursued in future studies.

The results of this work bring together over two decades of research in tropical Atlantic variability and represent the first observational evidence for AMM growth, propagation, and decay driven by WES dynamics. This work also builds on the results of Chang et al. (2001) and others by illustrating the meridional extent to which air-sea coupling becomes important in sustaining SSTAs in the tropical Atlantic. Further, these results enhance our understanding of how meridional modes act as bridges between subtropical atmospheric variability and deep tropical SST variability. This can be readily applied to investigate similar modes of coupled variability in other basins (e.g., PMM). Our analysis also includes the first assessment of a large ensemble of CMIP5 models in their ability to produce realistic air-sea interactions in the tropical Atlantic.

Several important questions arise from the results of our study. For example, what is the role of air-sea interactions in maintaining SSTAs in the south tropical Atlantic? Our observational analysis showed little evidence that ocean-atmosphere interactions drive significant SST or surface wind changes through WES feedback. One hypothesis that could explain the discrepancy between the hemispheres is the lower number of surface wind observations in the South Atlantic relative to the North Atlantic. However, when we repeat Figures 4.2-4.4 using reanalysis products that assimilate satellite scatterometry observations, we find that the SH still shows little indication of air-sea coupling in the deep tropics (not shown). This may be an indication that low-cloud SST feedbacks, which are independent of surface latent heat flux anomalies and surface wind

convergences, are the dominant coupling mechanisms maintaining the SSTA in the SH (e.g., Evan et al. 2013; Tanimoto and Xie 2002).

It is also possible that the geometry of African coastline is unfavorable for WES feedback in the Southeast Atlantic. In particular, the African continent at around 15˚W limits the eastward extent of the warmest SSTA associated with the AMM. Therefore, the cross-equatorial surface wind anomalies forced by these SSTAs are limited to west of this longitude throughout the AMM's lifecycle (Figures 4.2 and 4.3). This leaves the Southeast Atlantic (e.g., the Gulf of Guinea) in a shadow zone for anti-symmetric Rossby waves that help propagate the anomalies associated with WES feedback westward (e.g., Xie 2004). Further, CMIP5 multi-model mean SST/U-wind lag correlation structure was reproduced more accurately in the SH than in the NH (Figure 4.8a). If we extrapolate the results of the NH and assume that the models poorly simulate air-sea interactions everywhere in the tropical Atlantic, then the fact that the models have skill in reproducing the SH SST/U-wind lag correlation may further highlight the insignificance of this type of air-sea interaction in generating and maintaining SH SSTAs. Based on this discussion, we feel a detailed investigation into the disparities between the NH and SH should be a focus of future work.

Coupled modes of tropical Atlantic variability like Atlantic Niño and the AMM are of high socioeconomic importance to the surrounding region. Therefore, future research efforts should build on the results of our observational analysis and aim to improve the representation of coupled interactions in climate models. Accomplishing this task would further enhance our understanding of air-sea interactions in the global tropics and increase our confidence in CMIP5 21st century climate change projections.

4.7 Acknowledgements

This material is based upon work supported in part by the National Science Foundation Graduate Research Fellowship (NSF; DGE-1144086). M.J.D is supported by the Jet Propulsion Laboratory at the California Institute of Technology, under a contract with the National Aeronautics and Space Administration. A.J.M is supported by the NSF (OCE1419306) and the National Oceanic and Atmospheric Administration (NOAA; NA14OAR4310276). We would like to thank Daniel J. Vimont for his helpful comments during the course of our study. We also thank Yu Kosaka for downloading and processing the CMIP5 data presented in Table 4.1. ERSSTv3b data set is freely available and maintained by NOAA's National Climate Data Center. NCEP Reanalysis data was provided by the NOAA/OAR/ESRL PSD, Boulder, Colorado, USA, from their web site at http://www.esrl.noaa.gov/psd/. We also express our gratitude to the World Climate Research Programme's Working Group on Coupled Modelling, which maintains CMIP. Additionally, we thank the climate modeling groups listed in Table 4.1 for producing their model output and making it available. Finally, we thank two anonymous reviewers for comments that improved the quality of this paper.

Chapter 4, in full, is a reprint of the material as it appears in Amaya, D. J., M. J. DeFlorio, A. J. Miller, and S.-P. Xie (2017), WES feedback and the Atlantic Meridional Mode: observations and CMIP5 comparisons, Climate Dynamics. The dissertation author was the primary investigator and author of this paper.

Table 4.1: The modeling center, country, model abbreviation, and number of ensemble members for each CMIP5 model used in this analysis.

Modeling center	CMIP5 model abbreviations	Number of runs
Centre for Australian Weather and Climate Research, Australia	ACCESS1-0	1
	ACCESS1-3	2
College of Global Change and Earth System Science, China	BNU-ESM	1
Centre for Meteorological Research, France	CNRM-CM5	10
Geophysical Fluid Dynamics Laboratory, USA	GFDL-ESM2G	1
	GFDL-ESM2 M	1
Institute for Numerical Mathematics, Russia	INM-CM4	1
Institute Pierre Simon Laplace, France	IPSL-CM5A-LR	6
	IPSL-CM5A-MR	3
	IPSL-CM5B-LR	1
University of Tokyo/NIES/JAMSTEC, Japan	MIROC5	5
Max Planck Institute for Meteorology, Germany	MPI-ESM-LR	3
	MPI-ESM-P	2
Meteorological Research Institute, Japan	MRI-CGCM3	5
	MRI-ESM1	1
Norwegian Climate Centre, Norway	NorESM1-M	3
	NorESM1-ME	1

Table 4.2: The first column lists all datasets (observations and CMIP5 models) used in this study. The second column is each model's MCA mode used in the multi-model mean for Figure 4.5. The corresponding EMCA mode used in the multi-model mean for Figures 4.6 and 4.7 is in parenthesis. The third column is the squared covariance fraction for the MCA (EMCA) mode indicated in the second column. The fourth column is the pattern correlation coefficient of the model MCA (EMCA) SSTA structure with the observed leading MCA (EMCA) mode. For the EMCA pattern correlation, the MAM SSTA structure was used. The last row is the average of each column, excluding the observations.

	MCA (EMCA) AMM mode	Covariance explained (%) by MCA (EMCA) AMM	Pattern correlation coefficient b/w model MCA (EMCA) and observations
Observations	1 (1)	66 (49)	1 (1)
ACCESS1-0	2 (1)	21 (55)	0.57 (0.60)
ACCESS1-3	2 (1)	22 (33)	0.74 (0.61)
BNU-ESM	2 (2)	19 (16)	0.82 (0.78)
CNRM-CM5	1 (1)	50 (39)	0.79 (0.70)
GFDL-ESM2G	1 (1)	46 (32)	0.80 (0.67)
GFDL-ESM2M	2 (2)	18 (9)	0.68 (0.53)
INM-CM4	2 (2)	18 (15)	0.60 (0.65)
IPSL-CM5A-LR	2 (3)	33 (11)	0.68 (0.84)
IPSL-CM5A-MR	1 (1)	42 (34)	0.56 (0.74)
IPSL-CM5B-LR	1 (1)	71 (60)	0.81 (0.76)
MIROC5	1 (1)	44 (51)	0.58 (0.59)
MPI-ESM-LR	1 (1)	44 (38)	0.88 (0.74)
MPI-ESM-P	1 (1)	41 (31)	0.78 (0.58)
MRI-CGCM3	1 (2)	36 (21)	0.65 (0.67)
MRI-ESM1	1 (1)	43 (50)	0.72 (0.63)
NorESM1-M	1 (3)	42 (10)	0.73 (0.77)
NorESM1-ME	4 (4)	6 (5)	0.56 (0.61)
Multi-model mean	1.53 (1.65)	35.06 (30)	0.70 (0.67)

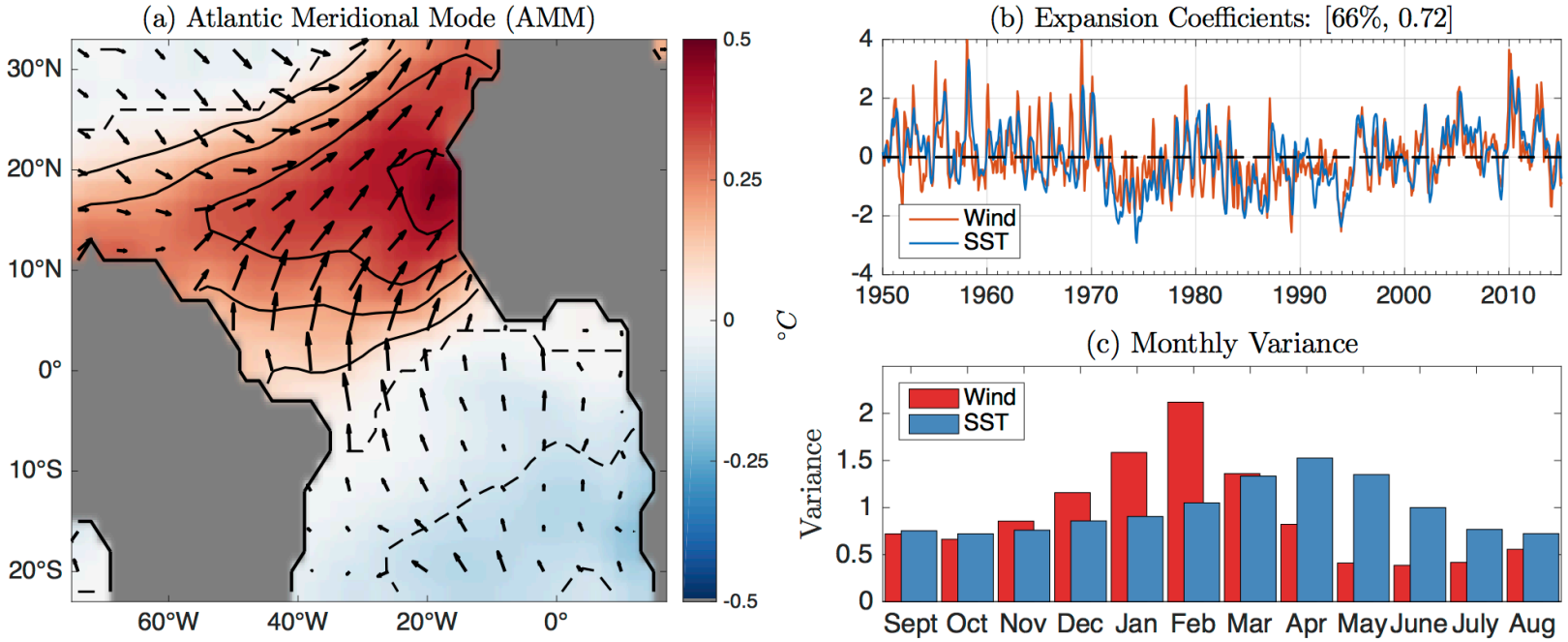

Figure 4.1: (a) The observed leading maximum covariance analysis (MCA) mode of SSTA (shading, ˚C) and 10-meter wind anomalies (arrows, m s^{-1}). (b) The corresponding left and right normalized expansion coefficients (EC). The first number in the brackets is the squared covariance fraction for the leading MCA mode; the second number is the correlation between the two ECs. (c) Month-to-month variance of the wind EC (red) and SST EC (blue).

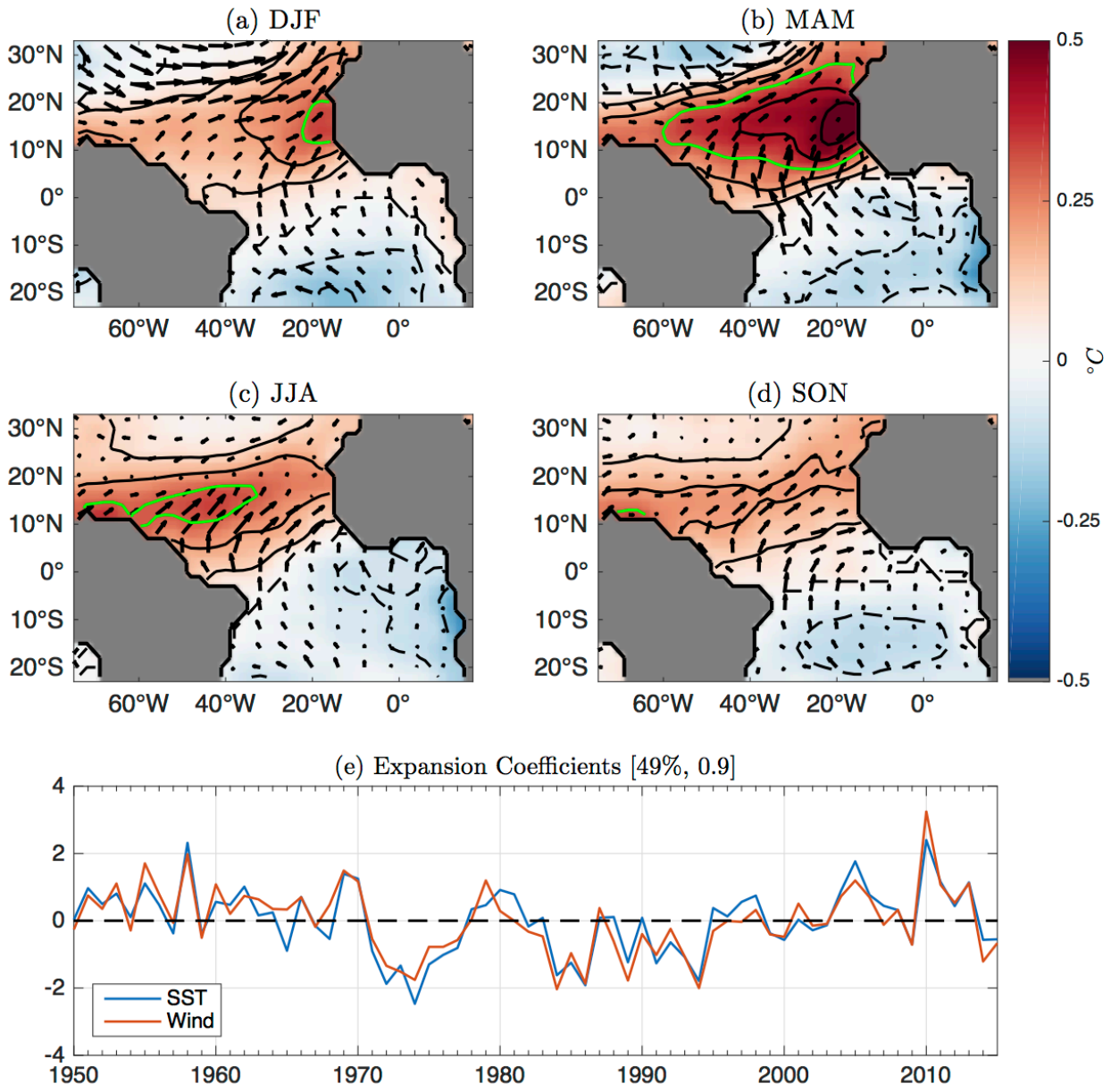

Figure 4.2: (a)-(d) The observed leading extended maximum covariance analysis (EMCA) mode of SSTA (shading/contours, ˚C) and 10-meter wind anomalies (arrows, m s^{-1}). The contour interval is 0.1˚C and the green line represents the 0.3˚C contour. (e) The corresponding left and right normalized expansion coefficients (EC). The first number in the brackets is the squared covariance fraction for the leading EMCA mode. The second number is the correlation between the two ECs, which indicates the strength of coupling between SST and winds in this region.

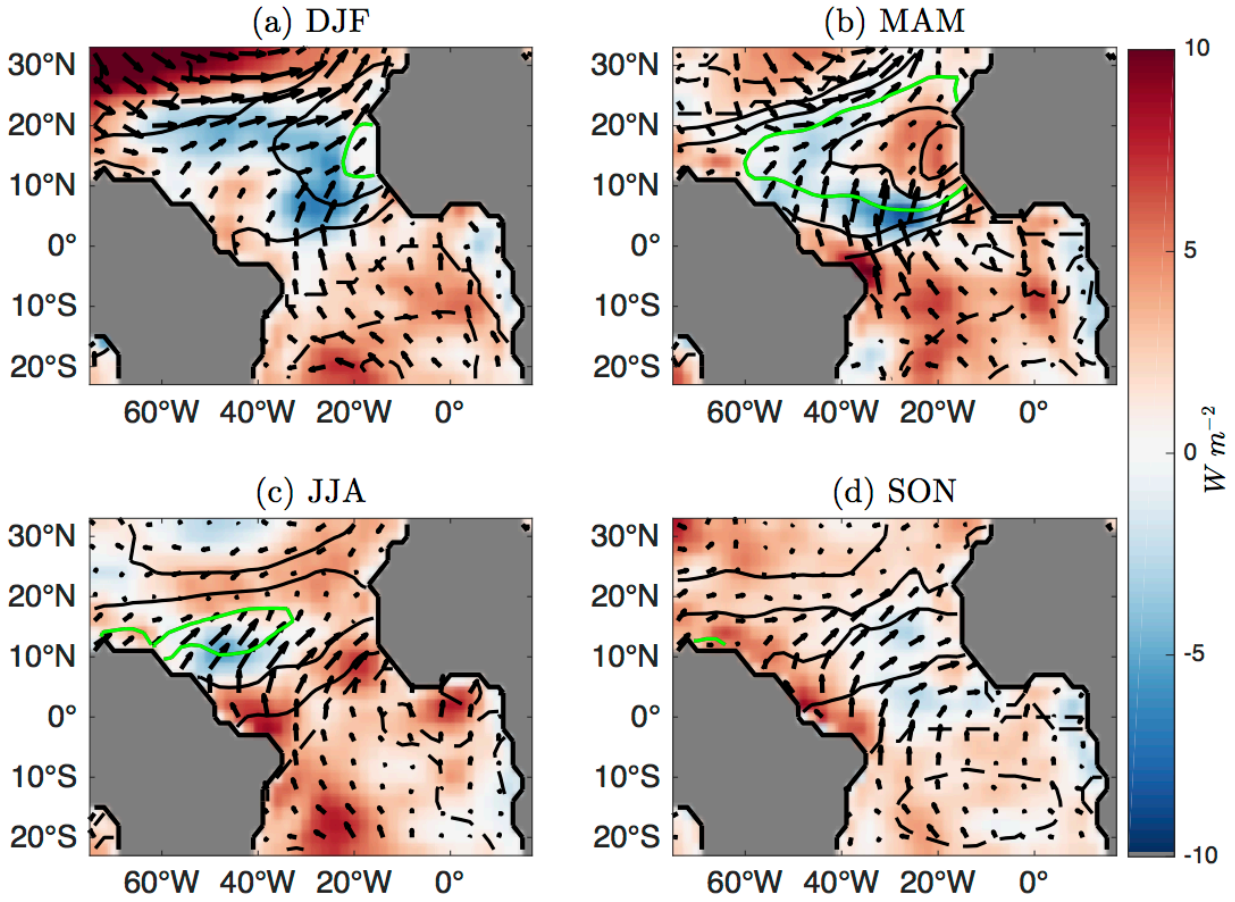

Figure 4.3: Regression of observed net surface latent heat flux (positive upward, shading, W m^{-2}) and 10-meter winds (arrows, m s^{-1}) onto the SST expansion coefficient in Figure 4.2e. Contours are the EMCA SSTA values shown in Figure 4.2. The contour interval is 0.1˚C and the green line represents the 0.3˚C contour.

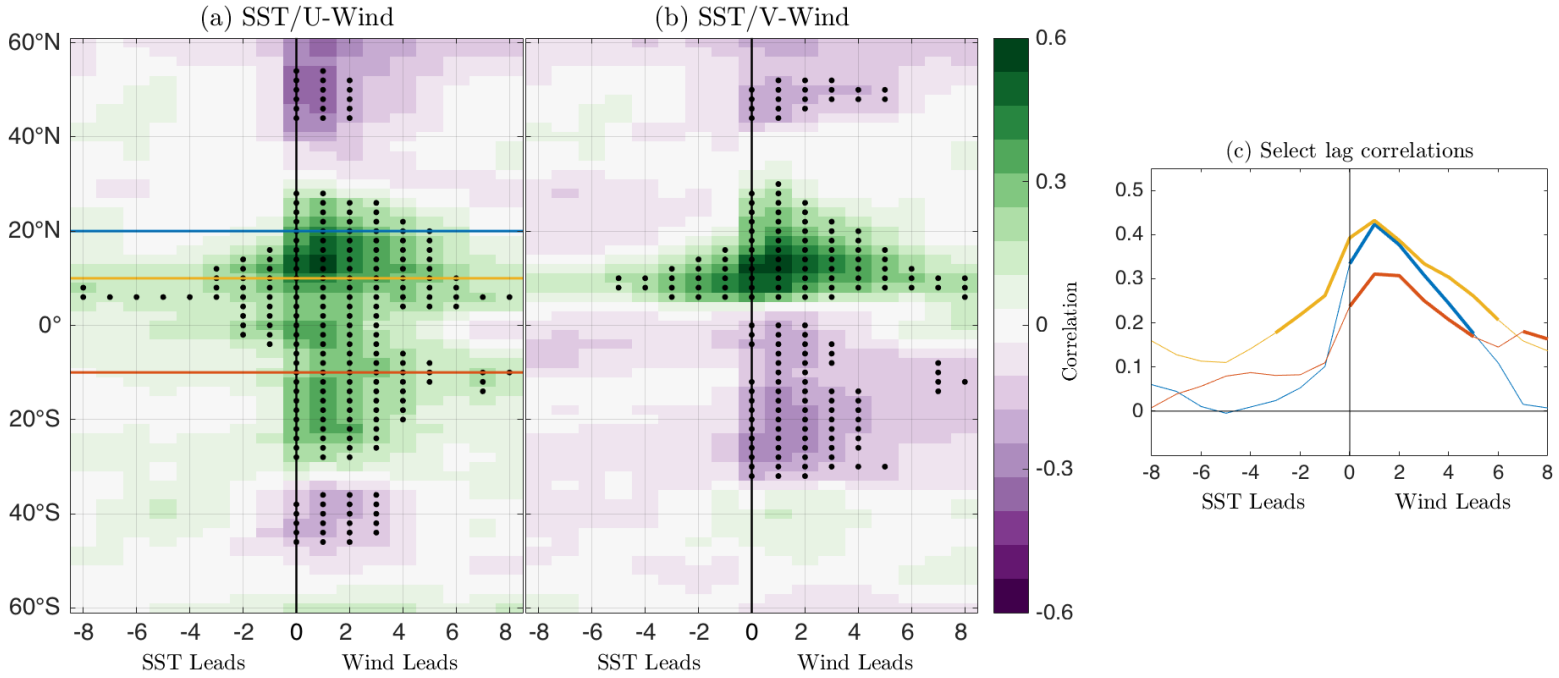

Figure 4.4: (a) Lag correlation (shading) between the observed zonal mean SSTA and 10-meter U-wind across the Atlantic basin. Horizontal colored lines indicate the select lag correlation curves shown in (c). (b) As in (a), but for the 10-meter V-wind. (c) Select lag correlation curves at 20˚N (blue), 10˚N (yellow), and 10˚S (red). Stippling in (a) and (b) and the bold parts of the curves in (c) indicates significance at 95% based on the e-folding timescale of the autocorrelation of the zonal mean SSTA at each latitude. The vertical black line denotes zero lag and the lags (shown on the x-axis) are in months.

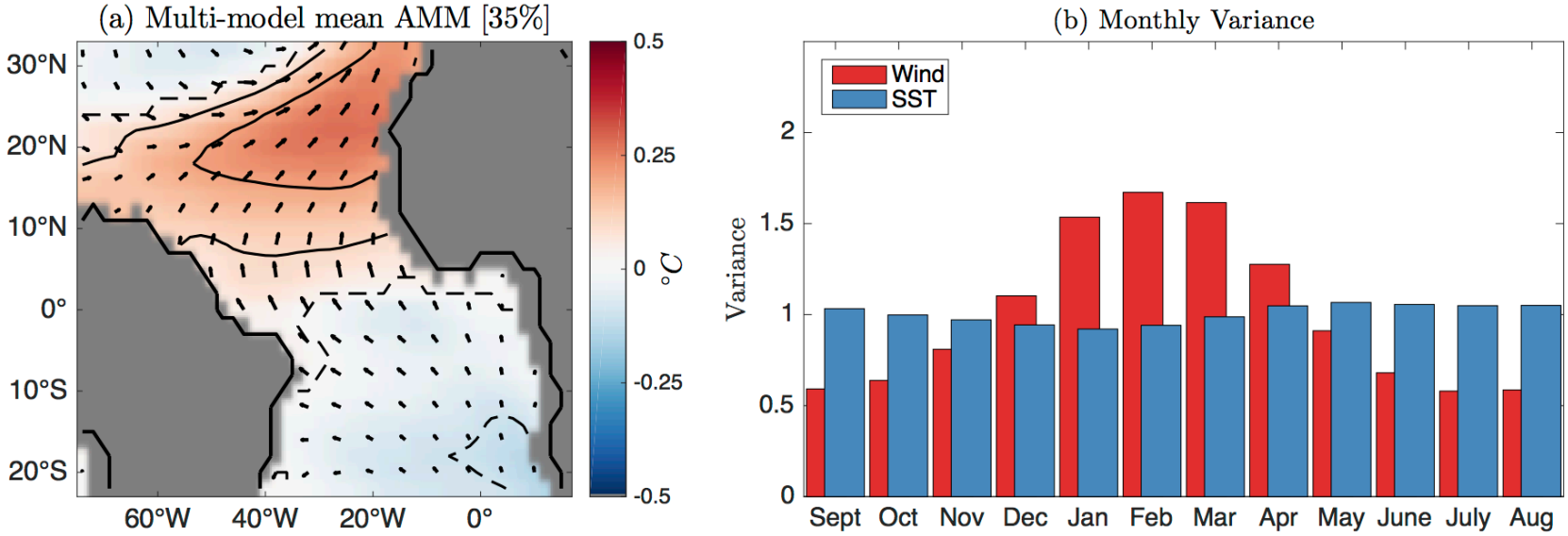

Figure 4.5: As in Figures 4.1a and 4.1c, but for the multi-model mean of the 17 CMIP5 models listed in Table 4.1. Note the different y-axis in (b).

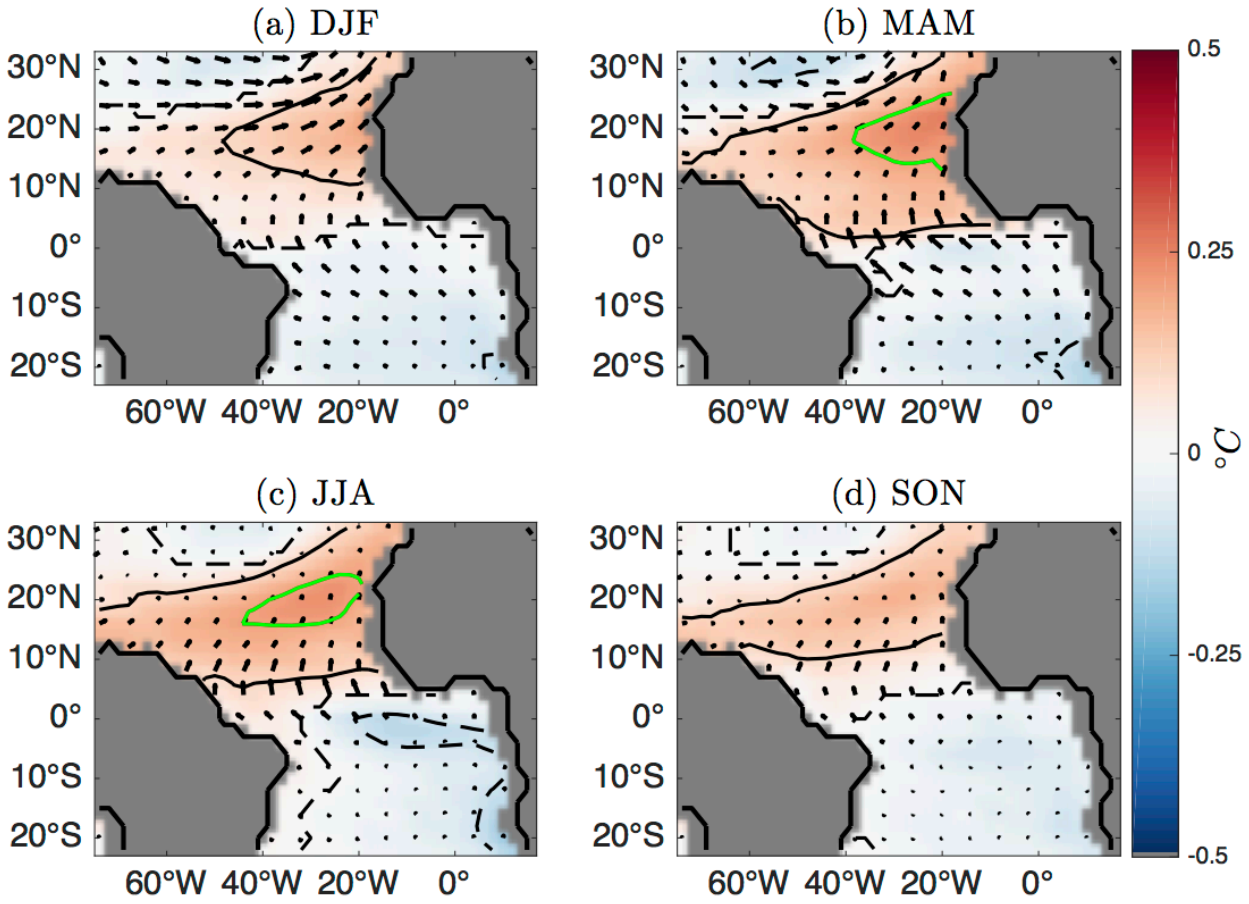

Figure 4.6: As in Figure 4.2, but for the multi-model mean of the 17 CMIP5 models listed in Table 4.1. The contour interval is 0.1˚C, but the green line now denotes the 0.2˚C contour.

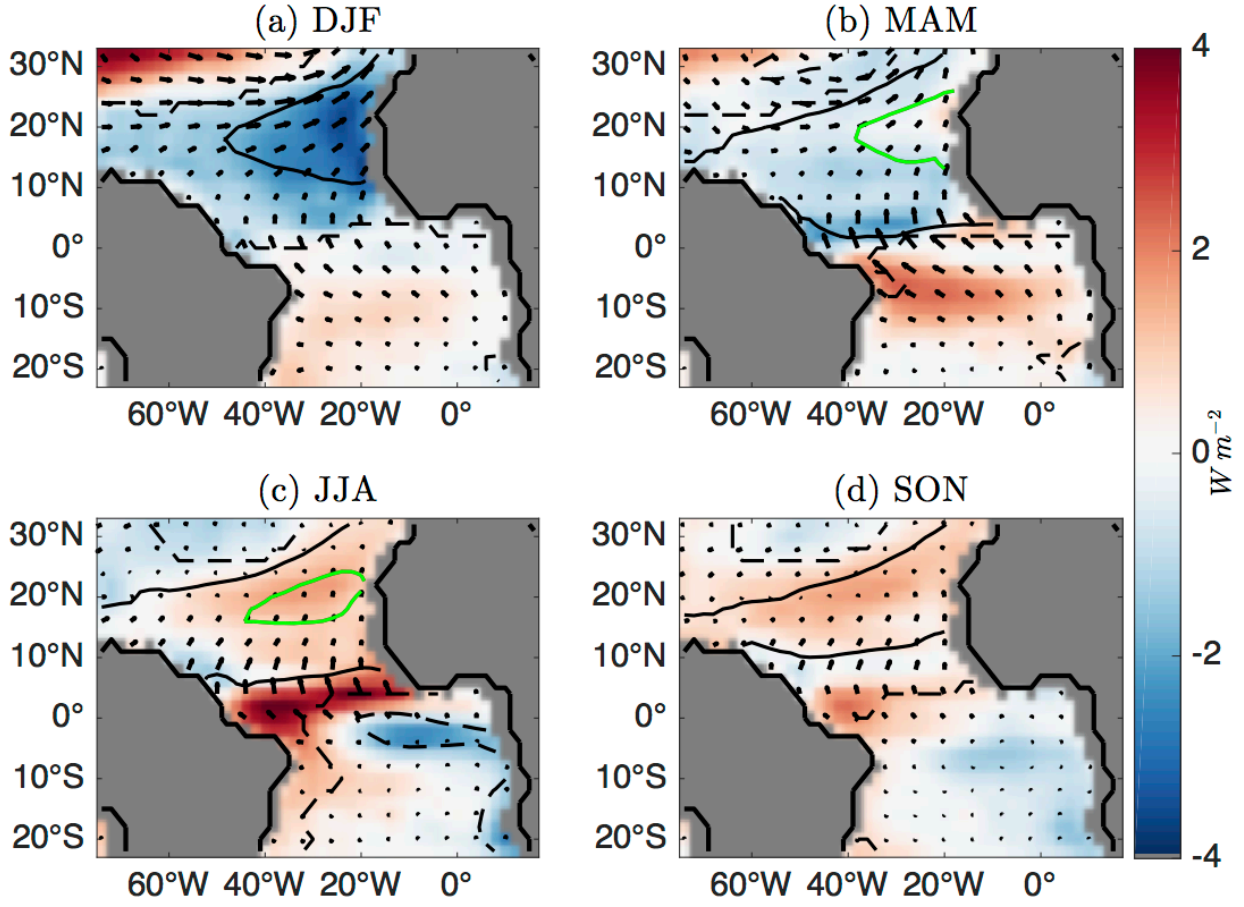

Figure 4.7: As in Figure 4.3, but for the multi-model mean of the 17 CMIP5 models listed in Table 4.1. The contour interval is 0.1˚C, but the green line now denotes the 0.2˚C contour. Note the different color scale between Figures 4.3 and 4.7.

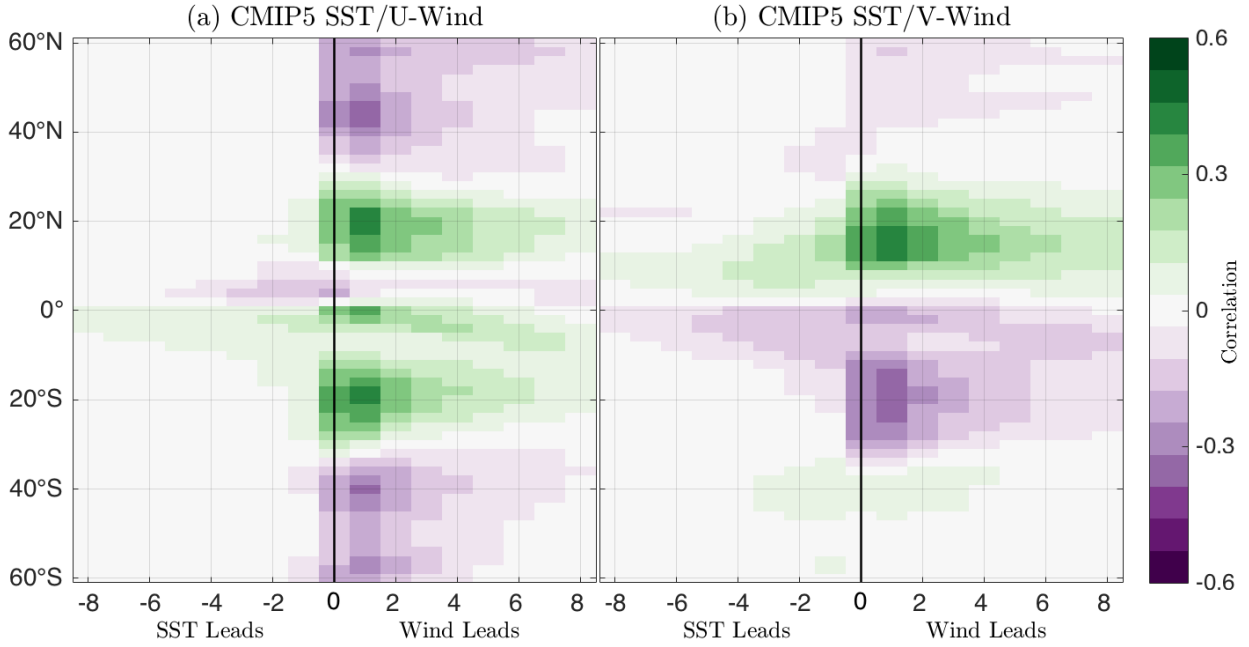

Figure 4.8: As in Figures 4.4a and 4.4b, but for the multi-model mean of the 17 CMIP5 models listed in Table 4.1.

Chapter 5

The North Pacific Pacemaker Effect on Historical ENSO and its Mechanisms

Abstract

Studies have indicated that North Pacific sea surface temperature (SST) variability can significantly modulate the El Niño-Southern Oscillation (ENSO), but there has been little effort to put extratropical-tropical interactions into the context of historical events. To quantify the role of the North Pacific in pacing the timing and magnitude of observed ENSO, we use a fully-coupled climate model to produce an ensemble of North Pacific Ocean-Global Atmosphere (nPOGA) SST pacemaker simulations. In nPOGA, SST anomalies are restored back to observations in the North Pacific (>15˚N), but are free to evolve throughout the rest of the globe. We find that the North Pacific SST has significantly influenced observed ENSO variability, accounting for approximately 15% of the total variance in boreal fall and winter. The connection between the North and tropical Pacific arises from two physical pathways: 1. A Wind-Evaporation-SST (WES) propagating mechanism, and 2. A Gill-like atmospheric response associated with anomalous deep convection in boreal summer and fall, which we refer to as the Summer Deep Convection (SDC) response. The SDC response accounts for 25% of the observed zonal wind variability around the equatorial dateline. On an event-by-event basis, nPOGA most closely reproduces the 2014-2015 and the 2015-2016 El Niños. In particular, we show that the 2015 Pacific Meridional Mode event increased wind forcing along the equator by 20%, potentially contributing to the extreme nature of the 2015-

2016 El Niño. Our results illustrate the significant role of extratropical noise in pacing the initiation and magnitude of ENSO events and may improve the predictability of ENSO on seasonal timescales.

5.1 Introduction

The El Niño-Southern Oscillation (ENSO) dominates interannual variability of the tropical Pacific coupled ocean-atmosphere system, impacting global weather and climate through atmospheric teleconnections (Horel and Wallace 1981). Historically, ENSO predictability research has focused on processes local to the tropics (e.g., Clarke 2014); however, over the past decade many studies have shown that mid-to-high latitude atmospheric variability can significantly influence ENSO evolution through ocean-atmosphere teleconnections (e.g., Vimont et al. 2001, 2009; Levine et al. 2017; Alexander et al. 2010). For example, stochastic fluctuations of the North Pacific Oscillation (NPO), a mode of atmospheric variability over the North Pacific (Rogers 1981), can initiate the so-called "Seasonal Footprinting Mechanism" (SFM; Vimont et al. 2001). The SFM describes the weakening of the North Pacific trade winds during boreal winter by the southern lobe of the NPO. This forces an anomalous latent heat flux (Q_{LH}) and leaves a "footprint" of sea surface temperature (SST) anomalies (SSTAs) extending from the coast of Baja California southwestward into the tropics. These SSTAs persist into boreal summer due to reinforcing feedbacks between the SST and the overlying circulation through latent and shortwave heat fluxes (Vimont et al. 2003b, 2009). This ultimately drives anomalous convection and atmospheric circulation anomalies in the deep tropics that can potentially trigger ENSO through enhanced ocean forcing (Vimont et al. 2003a,b).

The southwestward propagation of SST anomalies is a potentially important component of the SFM, and involves a series of interactions between surface wind anomalies, evaporation anomalies, and SSTAs. These coupled interactions, known as Wind-Evaporation-SST (WES) feedback (Xie and Philander 1994), signal the development of a Pacific Meridional Mode (PMM) event (Chiang and Vimont 2004). For a positive PMM event and for positive WES feedback in the Northern Hemisphere, the anomalous atmospheric response to warm SSTAs includes southwesterly flow on the southwestern edge of the maximum SST, which further weakens the northeasterly trades, producing an anomalous Q_{LH} that warms the ocean at that location. The net result is a southwestward propagation of the SSTAs and surface wind anomalies, which act to teleconnect ocean-atmosphere surface anomalies from the subtropics into the deep tropics (Liu and Xie 1994; Chiang and Vimont 2004; Vimont 2010; Martinez-Villalobos and Vimont 2017). While the southwestward propagation of SSTAs through the PMM appears to be an important component of the SFM, it is not clear whether such propagation is essential; in particular, it is possible that subtropical SSTAs themselves may be sufficient to excite a response in the tropics that can lead to ENSO variability. One intent of this study is to examine the possibility of a direct-forced tropical response to subtropical North Pacific SSTAs.

Several studies have attempted to quantify the extent to which North Pacific ocean-atmosphere variability can act as a precursor and predictor of ENSO. Vimont et al. (2003a) use a triad of global climate model (GCM) simulations to show that the SFM accounted for 20-40% of the model's interannual ENSO variability. Chang et al. (2007) use observational reanalysis data to suggest 12 out of the 17 ENSO events from 1958-2000 were preceded by PMM conditions in the subtropical North Pacific. Larson and Kirtman (2014) analyzed a set of hindcasts from the North American Multimodel Ensemble and showed some skill at predicting East Pacific El Niño events

when initialized with positive PMM conditions. Furthermore, Lu et al. (2017) show considerable skill in reproducing model ENSO when assimilating extratropical winds in a perfect-model framework. In forecast models, the PMM induced by internal variability of the extratropical atmosphere is an important source of uncertainty in predicting equatorial SSTs during the boreal spring (Ma et al. 2017).

These previous studies have advanced our understanding of the complex relationship between North Pacific SST variability and ENSO; however, there are still a variety of limitations that must be overcome in order to improve seasonal predictability of ENSO. For example, many PMM/ENSO studies are based on idealized climate model simulations with simplified or reduced model physics (Zhang et al. 2009; Alexander et al. 2010; Zhang et al. 2014b; Lu et al. 2017), which do not necessarily characterize the full extent of observed internal variability. In contrast, studies that have restricted themselves to observational reanalysis products suffer from reduced degrees of freedom given the limited observational record (Chang et al. 2007; Min et al. 2017). To overcome a limited sample size, several studies have analyzed long pre-industrial control simulations (Shin and An 2018; Sanchez et al. 2019); however, such methods must still contend with model biases in the tropical and North Pacific regions. Finally, there has been little effort to put North Pacific precursors in the context of the real-world ENSO events (Larson and Kirtman 2014; Lu and Liu 2018).

A reasonable approach to rectify many of these issues is to conduct a North Pacific SST pacemaker experiment. In a pacemaker experiment, a climate model is forced by the observed trajectory of SST in a specific region of the world's oceans, while allowing the model to freely evolve everywhere else (e.g., Deser et al. 2017). Forcing the model with observations ensures the model "sees" realistic variability free of model biases. The additional degrees of freedom afforded

by an ensemble of these simulations also make it possible to more accurately quantify the influence of regional SST variability on the observed time evolution of the climate system. Such multi-member pacemaker experiments have been successfully used to analyze real world teleconnections from the tropical Pacific (Kosaka and Xie 2013; Deser et al. 2017; Zhang et al. 2018) and from the North (Levine et al. 2017) and tropical Atlantic (Li et al. 2016).

In this study, we present the first North Pacific pacemaker experiment designed to investigate the connection between the North Pacific and ENSO in observations. We find that pacing the model with North Pacific SST provides significant skill in reproducing observed ENSO, especially in boreal fall and winter. These mid-latitude teleconnections are made possible through a combination of WES feedback-driven propagation in boreal spring, and a secondary pathway related to an interaction between North Pacific SSTAs and the mean Intertropical Convergence Zone (ITCZ). On an event-by-event basis, the clearest examples of the North Pacific influence on ENSO are the weak 2014-2015 El Niño and the extreme 2015-2016 El Niño. In particular, our results suggest that North Pacific SSTAs would have driven a more coherent 2014-2015 El Niño than observed if not for internal variations of tropical surface winds. Further, we find that equatorial wind forcing associated with the extreme 2015-2016 was significantly enhanced by the strongest North Pacific PMM event in at least the last 70 years. Our results take an important step towards quantifying North Pacific teleconnections within the context of historical ENSO events, and highlight the importance of recognizing the distinct pathways by which extratropical ocean-atmosphere variability can teleconnect into the tropics and influence ENSO.

The rest of this paper is organized as follows. In Section 5.2 we outline the experimental design of our model simulations and the observational data sets used. Section 5.3 and 5.4 assesses the pacemaker's ability to produce a physically consistent connection between the North Pacific

and the tropics. Section 5.5 discusses individual El Niño events, and Section 5.6 provides a summary with conclusions.

5.2 Data and methods

5.2.1 Model description

In this study, we use the Geophysical Fluid Dynamics Laboratory coupled model version 2.1 (Delworth et al. 2006; GFDL-CM2.1). GFDL-CM2.1 has land and atmosphere components with a horizontal resolution of ~2˚ latitude x 2.5˚ longitude and 24 vertical levels. The atmosphere model (GFDL-AM2.1) can be run as an uncoupled component by prescribing the lower boundary condition. The ocean has 50 vertical levels and a horizontal resolution of 1˚ for both latitude and longitude, with meridional resolution equatorward of 30˚ becoming progressively finer until it is 1/3˚ at the equator.

5.2.2 nPOGA and nATMO experimental design

To quantify the role of North Pacific SSTs in pacing the timing and magnitude of past ENSO events, we use GFDL-CM2.1 to produce an ensemble of North Pacific Ocean-Global Atmosphere (nPOGA) pacemaker simulations (Figure 5.1). SSTs north of 15˚N in the Pacific are restored to the model climatology plus the observed anomaly calculated from the Hadley Centre Global Sea Ice and Sea Surface Temperature version 1.1 (HadISST) dataset (Rayner et al. 2003). The model climatology is based on the 1920-2005 average daily climatology of 10 fully-coupled historical simulations, each forced with historical radiative forcing from the Coupled Model Intercomparison Project phase 5 (CMIP5; Taylor et al. 2012). Observed anomalies are based on monthly values that are linearly interpolated to daily before restoration.

The SST restoration is done by overriding the surface sensible heat flux to the ocean (F) where:

$$F = (1 - \alpha)F_* + \alpha \frac{ch\rho}{\tau}(SST' - SST'_*) \quad (5.1)$$

Primes denote anomalies, asterisks represent model-diagnosed values, c is the specific heat of sea water, h = 50 m is the typical depth of the ocean-mixed layer, ρ is the density of sea water, and τ = 10 days is the restoring timescale. The reference temperature (SST') indicates the HadISST anomaly. The weighting coefficient (α) ranges from 0-1, where 1 is full restoration and 0 is no restoration. In Figure 5.1, α = 1 within the Pacific Ocean north of 15˚N (solid black line). This value linearly decreases in a 5˚ buffer zone to α = 0 south of 10˚N in the Pacific (dashed line), and it is identically 0 everywhere else on the globe. nPOGA consists of a 10-member ensemble for 1950-2016. In addition to SST restoration, each member is initialized with slightly different initial conditions and forced with CMIP5 radiative forcings for 1950-2005 and Representative Concentration Pathway (RCP4.5) for 2006-2016.

It is important to assess whether atmospheric variability *outside* of the restoring region in nPOGA is the result of local tropical coupled feedbacks or is merely a "downstream" response to restored North Pacific SSTs. To isolate the influence of coupled feedbacks, we compare nPOGA to a 10-member ensemble of North Pacific, atmosphere-only (nATMO) runs. Ensemble members in nATMO use GFDL-AM2.1 in uncoupled mode and are forced with the same historical+RCP4.5 radiative forcings as nPOGA. Additionally, the lower boundary condition is set to the same SST values as nPOGA in the North Pacific (Figure 5.1), and the model climatological seasonal cycle everywhere else. Therefore, the ensemble mean of nATMO represents the direct SST driven response independent of tropical coupled feedbacks.

Finally, in Section 5.3 we compare nPOGA to the 10-member GFDL-CM2.1 historical+RCP4.5 simulation (HIST) available in the CMIP5 archive. HIST is forced by the same radiative forcings, but its internal variability is not constrained by the observations as in nPOGA. Therefore, we treat HIST as our control for this study.

5.2.3 Observational data sets and significance testing

nPOGA and nATMO simulated results are compared to HadISST and the Japanese 55-year Reanalysis (JRA-55; 1.25˚ x 1.25˚; Kobayashi et al. 2015). Comparisons between nPOGA/nATMO and JRA-55 are limited to their overlapping time periods (1958-2016). Results are qualitatively unchanged if we use the National Centers for Environmental Prediction/National Center for Atmospheric Research (NCEP/NCAR) reanalysis dataset for 1950-2016. In Section 5.4, we perform a composite analysis on the standardized Chiang and Vimont (2004) PMM SST Principal Component (hereafter PMM_{CV} index) in observations, which is made available by the Earth System Research Laboratory. For clarity, all data sets have been detrended, subjected to a 3-month running mean, and interpolated to the GFDL-CM2.1 atmospheric grid. Results are insensitive to changes in these data processing steps. Unless otherwise noted, statistical significance is determined using a Student's t-test at the 95% confidence level after correcting the degrees of freedom for lag-1 autocorrelation.

5.3 Comparing simulated ENSO to observations

To assess nPOGA's ability to simulate real-world ENSO events, we compare area averaged Niño indices (Figure 5.1 shaded boxes) in nPOGA and HadISST (Figure 5.2). The full timeseries correlations between observed and simulated ensemble mean ENSO are R = 0.25, 0.31, 0.34 for

Nino3, Nino3.4, and Nino4, respectively. The latter two correlations are significant at the 80% confidence level. While these correlations are not strongly significant, the values compare well to correlations of the same observed indices with our control experiment (R = -0.01, -0.01, 0.01; not shown). nPOGA's skill is more readily apparent when comparing seasonally averaged correlations (Figure 5.3). The HIST control simulation does not significantly reproduce observed ENSO variability in any season (not shown); however, nPOGA produces a 95% significant correlation with observed Nino3 from September-January and with observed Nino3.4 and Nino4 from August-April. The persistent skill in the West/Central Pacific (i.e., Nino4 region) throughout the year is interesting, and suggests that the North Pacific SST-forced variability is more closely related to Central Pacific (CP) ENSO than East Pacific events, which is consistent with previous studies (Furtado et al. 2012; Vimont et al. 2014; Lin et al. 2015).

Are nPOGA simulated ENSO events preceded by observed PMM events as we might expect? Figure 5.4 shows scatter plots of October-November-December (OND) Niño indices for the nPOGA ensemble mean (y-axis) and HadISST (x-axis). The shading of each circle denotes the magnitude of PMM_{CV} in the *preceding* February-April (FMA). Consistent with Figure 5.3, there is a significant positive relationship between nPOGA simulated ENSO and observed ENSO (R = 0.38, 0.40, and 0.39 for Nino3, Nino3.4 and Nino4, respectively). Additionally, the shading indicates that El Niño events in nPOGA tend to be preceded by positive PMM events, while La Niña events tend to be preceded by negative PMM events (R = 0.48, 0.44, and 0.38). Interestingly, the PMM_{CV}/ENSO relationship seems to be more consistent for El Niño events than La Niña events, particularly in Nino4 where nPOGA La Niña events are not as well simulated compared to observations. Additionally, the nPOGA ENSO events are generally weaker than in observations. This is consistent with a similar analysis conducted by Lu and Liu (2018) and is likely because the

nPOGA ENSO values are the ensemble average, and only represent the potential strength of ENSOs forced by the North Pacific.

5.4 Investigating physical mechanisms in nPOGA

What are the physical mechanisms connecting the North Pacific restoring region in nPOGA to the freely evolving tropical Pacific? Answering this would allow us to better understand why and how nPOGA succeeds at reproducing observed ENSO variability on an event-by-event basis. To begin, we present Hovmöller diagrams that are constructed with nPOGA and nATMO model output and are composited on high "PMM years" (Figure 5.6). In order to highlight the evolution of nPOGA North Pacific SSTs, the Hovmöllers are separated into two pathways (Figure 5.5): Path A, which stretches northeast-to-southwest from point 0 at 25˚N, 122˚W to point 6 at 1˚N, 178˚W, and Path B, which runs west-to-east along the equatorial Pacific averaged 3˚S-3˚N.

Model variables are composited along these paths when the April-May-June (AMJ) standardized PMM_{CV} is greater than 0.5 standard deviations (N = 19 positive PMM events x 10 ensemble members = 190 independent samples). When this occurs, it is considered a positive "PMM year" and the data from January of that year (Year 0) through April of the following year (Year 1) are added to the composite. We choose to composite on AMJ because PMM_{CV} variance is highest in this season (Chiang and Vimont 2004), and we focus on warm PMM events because of the more coherent relationship between nPOGA and observed El Niño events (Figure 5.4). Results are insensitive to the choice of compositing season.

5.4.1 WES-driven teleconnections to the deep tropics

Figure 5.6 shows the ensemble mean Hovmöller composites of SSTAs, Q_{LH} anomalies, and zonal 10m wind anomalies along Paths A and B for nPOGA (left column) and nATMO (right column). Recall that SSTAs in the restoring region (right of vertical black lines) are identical between nPOGA and nATMO. Outside of the restoring region, nPOGA is completely free to evolve and anomalies here are the result of North Pacific SST forcing plus local coupled feedbacks (see Data and methods). Whereas in nATMO, there are no SSTAs outside the restoring region, so atmospheric anomalies here are solely the result of "downstream" North Pacific SST forcing.

Focusing first on the nPOGA Hovmöller composites (Figure 5.6; left column), the evolution of SSTAs in the restoring region along Path A follow the expected lifecycle of a positive PMM event, with warm anomalies peaking in the subtropical North Pacific during boreal spring and largely persisting throughout boreal summer and fall (e.g., Vimont et al. 2009; Alexander et al. 2010). Outside of the restoring region where the model is free to evolve, there is a tongue of warm SSTAs that propagates from the edge of the buffer zone in April (0), southwestward along Path A, arriving on the equator in July (0). Co-located with these propagating SSTAs are a band of positive Q_{LH} anomalies. These Q_{LH} anomalies are consistent with coincident westerly U10 anomalies that would tend to weaken the background easterly trade winds, reduce evaporative cooling at the surface, and warm the ocean.

The strong spatial continuity, persistence, and southwestward propagation of the SSTAs, Q_{LH} anomalies, and U10 anomalies is consistent with WES feedback theory (Xie and Philander 1994; Amaya et al. 2017), and suggests restoring North Pacific SST in nPOGA excites local air-sea coupled feedbacks that can teleconnect the forced signal into the deep tropics. This conclusion is supported by the nATMO Hovmöller composite (right column), which does not show significant

surface wind anomalies outside of the restoring region from January (0) to June (0). The nATMO results do, however, show surface wind and Q_{LH} anomalies within the buffer zone that are larger than nPOGA during this time period, particularly around point 3 of Path A. It is possible that the surface winds are stronger due to the reduced SSTA gradient in nPOGA relative to nATMO. Further, nATMO Q_{LH} anomalies are likely larger because there is not an interactive ocean to dampen these fluxes (Barsugli and Battisti 1998). In contrast, the nPOGA ocean model becomes increasingly interactive within the buffer zone moving equatorward of 15˚N, which would tend to dampen fluxes there. Additionally, while changes in low cloud fraction have also been shown to contribute to the evolution of subtropical North Pacific SSTAs through a modification of downwelling surface shortwave radiation (e.g., Vimont et al. 2009), we do not find evidence that increased shortwave anomalies are required to drive these propagating SSTAs in nPOGA. Instead, positive downwelling shortwave anomalies only act to reinforce the warm SSTAs within the restoring region (not shown).

Once the WES-driven SSTAs and U10 anomalies arrive on the equator, they grow in magnitude and persist into the following year (Figure 6, left column, Path A), suggesting the presence of additional local feedbacks that act to amplify the signal. The downward latent heat flux anomalies from July (0) to November (0) in Path A of both the nPOGA and nATMO simulations indicate a potential role for WES feedback to continue amplifying the western equatorial Pacific SSTs (note that in the nPOGA simulation these downward flux anomalies occur over positive SSTAs, indicating an important role for wind speed variations). At the same time, the westerly wind anomalies can excite dynamical feedbacks that amplify SST across the basin.

Further evidence of this can be seen in nPOGA Path B. This east-west Hovmöller plot shows warm, El Niño-like SSTAs beginning to grow during May (0) in the eastern equatorial

Pacific, while significant westerly wind anomalies persist in the western equatorial Pacific. The position of the warm SSTAs in the east relative to the remote wind forcing in the west suggests the importance of ocean dynamics (e.g., downwelling Kelvin waves) in maintaining the warm SSTAs on the equator. From June (0) to March (1), the SSTA maximum strengthens and spreads from east to west as the U10 anomalies also grow in the west and central equatorial Pacific, both ultimately peaking in November (0). These results suggest that North Pacific SSTAs alone, through a WES-driven teleconnection, are sufficient to drive equatorial westerly wind anomalies that can initiate Bjerknes feedbacks and generate an El Niño event in the model.

5.4.2 Mean state interactions and "downstream" forcing of tropical winds

Interestingly, the nATMO Hovmöller diagrams (Figure 5.6, right column) also show significant surface wind anomalies from July (0) to November (0) extending from the restoring region in the subtropical North Pacific (Path A) all the way to the equator (Path B). This suggests that a component of the equatorial westerly wind anomalies in nPOGA are a direct response to the restored North Pacific SSTs. To investigate this relationship further, we compare the nATMO SSTAs and U10 anomalies from Figure 5.6 with nATMO precipitation anomalies (mm day^{-1}; colored contours) composited along Path A (Figure 5.7). For reference, we also plot the position of the climatological ITCZ (gray shading) by showing precipitation averaged in the Pacific 150˚E-100˚W at each latitude indicated by the upper x-axis.

Figure 5.7 shows a dipole of precipitation anomalies persisting from March (0) to November (0), with increased precipitation over the warm SSTAs in the restoring region, and decreased precipitation along the edge of the buffer zone. This precipitation pattern is consistent with anomalous convection driven by increased surface wind convergence over the warm SSTAs,

and would tend to produce an anomalous northward shift of the climatological ITCZ. Though the precipitation anomalies persist in time along with the warmest SSTAs, the U10 anomalies do not significantly extend toward the equator until late boreal summer into boreal fall. This can be explained by the timing of the warmest subtropical SSTAs relative to the position of the mean ITCZ during its seasonal migration. In boreal spring, when the PMM peaks, the ITCZ is closest to the equator and is less sensitive to off-equatorial SSTAs. In contrast, during the late summer and fall, the ITCZ is furthest north and is more easily influenced by the persistent warm conditions in the subtropical North Pacific.

This atmospheric response can be seen clearly in the horizontal view of nATMO August-September-October (ASO) composited SSTAs, precipitation anomalies, sea level pressure anomalies (SLPAs), and surface wind anomalies (Figure 5.8). In Figure 5.8a, the largest precipitation response is from 180˚ to the Mexican coastline. The atmospheric circulation induced by the associated convective heating is generally consistent with the tropical atmospheric response to an off-equatorial heat source (e.g., Gill 1980), which produces the significant surface winds seen in Figure 5.6 (right column). Figure 5.9 further illustrates the importance of the late summertime subtropical SSTAs to this equatorial wind response by comparing ASO SSTAs averaged from 15˚N-25˚N, 150˚W-120˚W (black box, Figure 5.8a) to a westerly wind index (U_{eq}) computed by averaging nATMO zonal wind anomalies from 3˚S-3˚N, 170˚E-170˚W (black box, Figure 5.8b). Consistent with the composite analysis, we find that the nATMO U_{eq} index is significantly correlated with the prescribed subtropical SSTAs (R = 0.68).

While Figures 5.7-5.9 illustrate the strong seasonality of the uncoupled response, we note that Vimont et al. (2009) report a similar seasonality using coupled simulations. Further, Vimont

et al. (2009) indicate that ocean-atmosphere coupling tends to amplify the downstream U10 response and can drive it even closer to the equator during late boreal summer and boreal fall.

5.4.3 Quantifying the "Summer Deep Convection" response in observations

The analysis of nATMO in Figures 5.6-5.9 highlights the striking interaction between the mean ITCZ and warm subtropical SSTAs that are related to the persistence of the PMM into boreal summer. This interaction provides a second pathway for the North Pacific to reenergize WES feedback, remotely influence the deep tropics, and interact with ENSO. For clarity, we introduce the term "Summer Deep Convection" (SDC) response to refer to this additional teleconnective pathway. The SDC response as seen in Figure 5.8 is reminiscent of results outlined by Vimont et al. (2001) and others, who focused on the overall evolution of the SFM by analyzing the impact of summertime subtropical SSTs on the tropical atmosphere. Indeed, Figure 4b in Vimont et al. (2001) compares well with Figure 5.8 of this study. Given that nATMO is forced by observations, we can utilize our simulations to cleanly isolate the impact of the SDC response on historical equatorial surface winds. Equatorial winds around the dateline are routinely used as an indicator and predictor of ENSO conditions. Thus, such an analysis could potentially improve ENSO predictability on seasonal timescales.

Figure 5.10a shows ASO averaged HadISST SSTAs (shading) and JRA-55 10m wind anomalies (black arrows) composited on the same AMJ PMM_{CV} events as in Figures 5.6-5.8. Overlaid in green arrows are ensemble mean nATMO composite wind anomalies in ASO. Since nATMO is forced by observed SSTAs north of 15˚N, we can compare the magnitude and direction

of the observed (black) and simulated (green) winds to gain some intuition for how the observed wind field is impacted by the SDC-forced wind anomalies.

In both observations and nATMO, there is a basin-wide anomalous cyclonic circulation centered around 20˚N that is associated with the thermally driven low-pressure center. There are slight differences in wind magnitude in the restoring region, which may be due to the difference in sample size between the nATMO and observed composites (190 versus 19 samples, respectively). Nevertheless, the close overall agreement between the two wind fields suggests the observed wind structure is largely a direct response to the underlying SSTAs. South of the restoring region, the magnitude of the nATMO winds decreases relative to observations due to the absence of amplifying effects from coupled feedbacks. However, along the equator, the nATMO winds continue to show some skill in simulating the observed winds, particularly around the dateline, indicating that the SDC response may significantly contribute to the time variability of observed westerly winds in this region.

To quantify the equatorial westerly wind variance explained by North Pacific SSTAs in observations, we create a westerly wind index by averaging 10m zonal wind anomalies from 3˚S-3˚N, 170˚E-170˚W (black box, Figure 5.10a). We then correlate seasonally averaged values of this index between nATMO and JRA-55 from 1958-2016. This process is repeated with nPOGA for comparison, and the results are shown in Figure 5.10b. nATMO only produces a significant correlation with observations in late boreal summer and early boreal fall, which is consistent with our hypothesis that subtropical North Pacific SSTAs are most effective at remotely influencing the deep tropics when the mean ITCZ is furthest north (Figures 5.7). Based on this calculation, about 25% of the observed time variability of August-October equatorial U10 anomalies can be explained by the remote SDC response in the North Pacific.

In comparison, nPOGA explains significant portions of the observed U10 index through much of the year, with separate peaks in May and August. This first peak explains 20% of the variance and can be interpreted as the contribution to the observed equatorial U10 variance by surface winds forced by local air-sea interactions such as WES feedback. The second peak explains about 25% of the variance and is likely also due to the SDC response. The decrease in correlation after the August peak may be due to other ocean-atmosphere interactions, which are present in nPOGA and not nATMO. This would add additional noise to nPOGA that may lower the overall correlation. This highlights the difficulty of separating the nPOGA wind contribution due to mixed layer coupled feedbacks (e.g., WES feedback) relative to coupled feedbacks involving a dynamical ocean (e.g., Bjerknes feedback). Ideally, additional comparisons would be made to an atmospheric model coupled to a mixed-layer ocean, but that is beyond the scope of this study. We encourage future modeling efforts on this topic.

5.5 The 2014-2016 ENSO cycle, a case study

We showed that in nPOGA, ENSO events can be initiated by local air-sea interactions (i.e. WES feedback and Bjerknes feedback) excited by restored North Pacific SSTAs. These tropical signals can also be amplified and/or reinforced in boreal summer by locally uncoupled surface winds generated by the subtropical SDC response. In the real world, the efficacy of these different teleconnections to influence the development of an ENSO event would depend on the internal state of the tropics when the North Pacific signal “arrives”. This signal-to-noise problem is further highlighted by the large spread in Niño indices among nPOGA ensemble members, which makes an event-by-event comparison between the model and observations difficult (Figure 5.2).

However, nPOGA does show remarkable reproducibility of several ENSO events, including the weak 2014-2015 El Niño and the extreme 2015-2016 El Niño. Given the broad scientific interest in these two El Niños (e.g., Hu and Fedorov 2016; Maeda et al. 2016; Levine and McPhaden 2016; Hu and Fedorov 2017; Siler et al. 2017), a more in-depth comparison between nPOGA, nATMO, and observations during this time period is appropriate. In this section we will take advantage of the physical intuition developed in Section 5.4 to analyze the 2014-2016 ENSO cycle as a case study.

5.5.1 The weak 2014-2015 El Niño

Figure 5.11 shows similar Hovmöller diagrams to Figure 5.6, but for the weak 2014-2015 El Niño event in observations (left column) and the ensemble means of nPOGA (middle column) and nATMO (right column). Note the different wind scales. Focusing first on observed Path B, we see significant westerly U10 anomalies centered around 160˚E from January-May 2014. These westerly wind events drove a series of downwelling Kelvin waves that suppressed upwelling and lead to warm SSTAs in the eastern equatorial Pacific beginning in May 2014. The strength of these wind events in conjunction with the magnitude of the eastern equatorial SSTAs and subsurface thermocline anomalies led many in the scientific community to believe a strong El Niño was developing (Pacific ENSO Update, 2014).

However, a series of easterly wind events in the western equatorial Pacific during summer 2014 stunted the development of the El Niño by suppressing the positive Bjerknes feedback critical to its growth (Hu and Fedorov 2016). JRA-55 does not show easterly wind anomalies during this time period, but there is a pronounced weakening of the westerly wind anomalies in June-July 2014 (Figure 5.11, left column, Path B). As a result, the developing 2014 El Niño weakens

substantially, and never quite recovers. Instead, the observed SSTAs remain fragmented around the Central Pacific, and the U10 anomalies in the West Pacific do not amplify, suggesting Bjerknes feedback does not fully establish.

Comparing to the nPOGA ensemble mean (Figure 5.11, left and middle columns, Path B), we find the pacemaker experiment does a remarkable job of simulating the overall timing and magnitude of the main 2014 El Niño. However, the initial westerly wind anomalies observed in winter/spring 2014 and the first observed SSTA maxima in boreal summer are not seen in nPOGA, suggesting that in reality they were the result of processes independent of the North Pacific. Following these events, nPOGA features a series of consistent westerly U10 anomalies west of 180˚ from April-August 2014 which give rise to an El Niño event that evolves more smoothly than observations.

The general consistency between the nPOGA and observed equatorial SST and wind anomalies during this time period suggests the real-world evolution of the 2014 El Niño was influenced by the North Pacific. This connection can be further diagnosed by comparing Figure 5.11 (Path A) to the composites presented in Figure 5.6. In each upper panel of Figure 5.11, the SSTAs depict a moderate positive PMM event evolving from spring 2014 to winter 2015. The time evolution of SSTAs in the restoring region is not as coherent as the canonical PMM event seen in Figure 5.6, even showing a temperature increase throughout the year instead of dampening as in the composite. The different SSTA evolution may be expected, as 2014 represents a single PMM event, and therefore provides an indication of the diversity present among all events.

Despite these differences, Figure 5.11 shows a general southwestward propagation of SSTAs in observations (Path A, left column) and in nPOGA (Path A, middle column), suggesting the presence of similar coupled processes to the composite. We indeed see evidence of WES

feedback via a band of positive Q_{LH} anomalies and co-located westerly U10 anomalies extending from the restoring region southwestward towards the equator from boreal spring to summer. In observations, there is a similar, albeit less coherent, propagating band of Q_{LH} and U10 anomalies from May-Sep 2014. nATMO (Figure 5.11, Path A, right column) fails to reproduce these winds, further supporting the role of local air-sea coupling in nPOGA and observations. Interestingly, we also note nATMO does not show a clear SDC response during summer 2014. This is peculiar given the strength of the warm SSTAs used to force the model (Figure 5.9). We will discuss this in more detail in Section 5.5.3.

To analyze the influence of the North Pacific on the weak 2014-2015 El Niño event, we also compare horizontal plots of SSTAs, Q_{LH}, and surface wind anomalies (Figure 5.12a-d). In FMA 2014, the warm PMM SSTAs are completely enveloped by positive Q_{LH} anomalies, suggesting that the ocean has not yet forced an atmospheric response (Vimont et al. 2003a). In May-July (MJJ) 2014 (Figure 5.12c), observations show a tilted dipole of Q_{LH} anomalies, with positive anomalies around 0˚-20˚N, 140˚E-180˚ and negative anomalies to the northeast around 10˚N-25˚N, 190˚W-220˚W. Co-located with the positive Q_{LH} anomalies are surface southwesterly anomalies extending south from 20˚N. In combination with the surface wind anomalies, the MJJ Q_{LH} dipole further supports the hypothesis that WES feedback was active in observations (Amaya et al. 2017), ultimately forming westerly winds on the equator in FMA and MJJ 2014.

Figures 5.12b and 5.12d depict the evolution of nPOGA during the same time periods. Note the different wind scales. In response to the restored SSTAs, nPOGA produces surface southwesterly anomalies converging in the subtropics near the edge of the buffer zone. In MJJ, there is a tilted Q_{LH} dipole with positive Q_{LH} and southwesterly anomalies from 0˚-10˚, 140˚E-170˚E that are very similar to observations (Figures 5.12c and 5.12d). As such, nPOGA features

comparable equatorial wind anomalies in the West Pacific that are favorable for the development of an El Niño in the model.

There are, however, some notable differences between nPOGA and observations. For example, observations show persistent southeasterly surface wind anomalies in the eastern equatorial and southeast tropical Pacific that are co-located with cool SSTAs. These signals are not reproduced in nPOGA, suggesting that they are independent of North Pacific forcing. The observed southeasterly surface wind anomalies in the eastern Pacific may instead be related to a long-term trend in cross-equatorial flow driven by multidecadal cooling in the southeastern Pacific (e.g, Amaya et al. 2015) and/or warming in the tropical Atlantic (Hu and Fedorov 2018).

Despite these differences, the combined results of Figure 5.11 and Figure 5.12a-d lead us to conclude that late boreal spring to early boreal summer equatorial wind forcing associated with the 2014-2015 El Niño was significantly impacted by North Pacific SSTAs through the WES feedback propagating mechanism outlined in Section 5.4. Further, the smooth, unbroken evolution of these equatorial winds in nPOGA suggests that the North Pacific forcing may have generated a more consistent 2014-2015 El Niño event if not for tropical internal variations.

5.5.2 The extreme 2015-2016 El Niño

Figure 5.13 shows the same Hovmöller transects as in Figure 5.11, but for the extreme 2015-2016 El Niño event. Note the change in colorbar and wind scale. In early 2015, the remnants of the 2014-2015 El Niño can be seen as a zonal dipole of positive SSTAs in the central equatorial Pacific and neutral SSTAs in the eastern equatorial Pacific (Figure 5.13, left column, Path B). A series of westerly wind events in the western Pacific from January-May 2015 then act to drive downwelling Kelvin waves, thereby warming eastern Pacific SSTAs and amplifying the zonal

wind response along the equator. Throughout the rest of the year, the SSTAs grow in amplitude, culminating in one of the warmest El Niño events on record.

Concurrently, the observed Path A shows the evolution of the strongest positive PMM event in at least the last 70 years, as indicated by the red circle in Figure 5.9. During this event, the warm SSTAs propagate along with a band of positive Q_{LH} and westerly anomalies southwestward from the subtropics in March 2015 to the equator around July 2015, indicating a positive WES feedback. This result is further supported by Figure 5.12e, which shows the tell-tale dipole of Q_{LH} anomalies, co-located southwesterly U10 anomalies, and cross-equatorial flow in FMA 2015. By MJJ, wind-driven ocean dynamics produce a developing El Niño response in the eastern equatorial Pacific (Figure 5.12g).

nPOGA captures many of these features, producing an El Niño event that peaks in November-January 2015 and results from a band of westerly wind events beginning in April 2015 (Figure 5.13, middle column, Path B). However, the WES feedback response is less clear in the model. Instead, the restored SSTAs appear disconnected and unrelated to the tropical anomalies (Figure 5.13, middle column, Path A). The reason for this discrepancy may be due, in part, to the different evolutions of the 2014-2015 El Niño event in observations and the nPOGA ensemble mean. In reality, the developing 2014 El Niño faltered, and ultimately failed to initiate a significant Bjerknes response, which left the equatorial Pacific in a CP El Niño-like state in the early parts of 2015 (Figure 5.12e). In contrast, without the interference of internal tropical variations, the nPOGA ensemble mean shows a 2014 El Niño that persists into 2015. These lingering warm anomalies appear to drive an anomalous surface wind convergence along the eastern equatorial Pacific (Figure 5.12f), preventing efficient WES feedback interactions outside the restoring region.

Whereas in observations, the more neutral eastern equatorial Pacific leaves the tropical atmosphere more sensitive to subtropical SSTA forcing.

By running an ensemble of nPOGA experiments, we have sampled a range of possible internal tropical states with which the restored North Pacific SSTAs may interact. As a result, there is a small subset of ensemble members whose 2014-2015 El Niño declines in a similar manner to observations. In these runs, the absence of warm eastern equatorial waters allows the tropical surface winds to more directly respond to the subtropical SST forcing, producing a more consistent WES feedback (not shown). This result and the results of Figure 5.12e and 12f support our interpretation above and suggest a more detailed investigation into the interaction between North Pacific teleconnections and different internal tropical states is warranted. Such an analysis is outside the scope of the current work, but we do plan to thoroughly investigate the nPOGA ensemble spread in a future study.

Our analysis of the observations in Figures 5.12 and 5.13 suggests WES feedback contributed to the early development of the observed 2015-2016 El Niño. There is also evidence that the equatorial wind forcing was amplified in summer 2015 by a significant SDC response. This is indicated by the nATMO ensemble mean winds, which extend from the subtropics to the equator in Figure 5.13 (right column). Figures 5.14b and 5.14d show the nATMO ensemble mean atmospheric response for ASO 2015. The northward shifted ITCZ, the zonal SLPA dipole in the subtropics, and the significant westerly surface wind anomalies on the equator are all very similar to the composite structures seen in Figure 5.8. By averaging zonal wind anomalies around the dateline (Figure 5.8b, black box) in observations and nATMO, we calculate that the SDC-effect increased the strength of surface winds along the equator by 20% in ASO 2015, potentially contributing the extreme nature of the 2015-2016 El Niño.

5.5.3 Differences in the 2014 and the 2015 SDC responses

The importance of the SDC response to the development of the 2015-2016 El Niño event stands in stark contrast to the 2014-2015 El Niño event, which did not produce significant equatorial winds in nATMO (Figure 5.11, right column). This is peculiar given the strength of the subtropical SSTAs in ASO 2014, which are among the warmest since 1950 (Figure 5.9). To investigate the source of the different atmospheric responses, Figure 5.14 shows the nATMO precipitation anomalies, surface wind anomalies, SLPAs, and SSTAs for ASO 2014 (Figure 5.14a and 14c) and ASO 2015 (Figure 5.14b and 14d). Note the different colorbars and precipitation contour intervals.

Compared to 2015, the warm SSTAs in 2014 are generally weaker and extend further northward and westward. In ASO 2014, the main convective response has been broken up into two distinct maxima in the western and eastern North Pacific, which results in fragmented circulation anomalies (Figures 5.14a and 5.14c). In contrast, the precipitation peak in ASO 2015 is spread more uniformly throughout the eastern North Pacific. As a result, the convective center in ASO 2015 generates a broad and coherent cyclonic circulation (Figure 5.14b and 14d) that compares well with the earlier composites (Figure 5.8).

These different equatorial wind responses may be due to the horizontal displacement of the warmest SSTAs in 2014 relative to 2015, which could account for the circulation differences in the subtropics and the extent to which they project along the equator. Another possibility could be that the subtropical SSTAs in 2014 were simply too weak to generate a coherent shift in the ITCZ. However, Figure 5.9 shows that there are years with comparably warm subtropical SSTAs that produce a more significant equatorial wind response. Regardless of precise mechanisms, Figures

5.9 and 5.14 illustrate the potential importance of the strength and pattern of subtropical SSTAs to the summertime tropical atmospheric response. Targeted modeling experiments are needed to determine the sensitivity of the tropical atmosphere to different regional subtropical SSTA perturbations.

5.6 Summary and discussion

In this study, we have presented the first North Pacific pacemaker experiment designed to investigate the connection between the North Pacific and ENSO in the historical record. We found that teleconnections driven by North Pacific SSTAs can account for a significant fraction of observed ENSO variability since 1950, especially in boreal fall and winter. These teleconnections (as summarized in Figure 5.15) are made possible, in part, by an interaction between SSTAs, latent heat flux anomalies, and surface wind anomalies known as WES feedback (Xie and Philander 1994; Amaya et al. 2017), which propagates the restored North Pacific forcing into the deep tropics during boreal spring and summer (Phase 2, Figure 5.15).

We also compared our nPOGA results to an ensemble of atmosphere-only runs, and identified an important secondary pathway for the North Pacific to influence tropical ocean-atmosphere variability during late boreal summer and fall. This second teleconnection is related to earlier work that focused on the evolution of the SFM (e.g., Vimont et al. 2001, 2003a,b), and stems from an interaction between North Pacific SSTAs and the mean position of the ITCZ during its seasonal migration. During the late summer, persistent PMM-related SSTAs force an anomalous northward shift of the ITCZ, which results in thermally driven circulation anomalies that resemble the atmospheric response to an off-equatorial heat source (Gill 1980). This process, which we refer to as the Summer Deep Convection (SDC) response, produces significant surface

winds along the equator that can influence equatorial SSTAs and ENSO through WES feedback and ocean dynamics (Phase 3, Figure 15). We showed that the SDC response accounts for about 25% of the observed equatorial zonal wind time variability during late boreal summer and early boreal fall.

The nPOGA simulation's overall skill is generally consistent with a recent study by Lu and Liu (2018), which assessed the extratropical impact on historical ENSO by assimilating observed ocean and atmosphere data at varying latitudes in a fully-coupled spectral model. In particular, the correlations between nPOGA-simulated ENSO and observations are comparable to those reported by Lu and Liu (2018) when they assimilated only ocean data poleward of 10˚ or 15˚. Despite these similarities, our work is more targeted at quantifying the physical mechanisms that connect the North Pacific to the tropics. This is different from Lu and Liu (2018), who assimilate data in both hemispheres simultaneously and at all longitudes.

Building on the physical intuition laid out in Section 5.4, we then analyzed the weak 2014-2015 El Niño and the extreme 2015-2016 El Niño as case studies in nPOGA. Our results suggested that the development of the 2014-2015 El Niño was aided by a positive WES feedback teleconnection from the North Pacific, which drove significant westerly winds on the equator and generated an El Niño in the model. This confirms earlier speculation by Di Lorenzo and Mantua (2016), who hypothesized that the 2013-2015 North Pacific marine heat wave (Bond et al. 2015; Amaya et al. 2016) may have included a positive PMM event that contributed to the development of the 2014-2015 El Niño. Our study suggested these interactions did occur in reality; however, internal tropical variations severely limited the effectiveness of 2014 PMM in creating a smoothly evolving 2014-2015 El Niño (Hu and Fedorov 2016).

The extreme 2015-2016 El Niño was preceded by the warmest subtropical North Pacific SSTAs in at least the last 70 years (Figure 5.9, red circle). We presented observational evidence that these 2015 SSTAs generated a positive WES feedback, which propagated the North Pacific surface anomalies into the deep tropics where they could influence equatorial ocean dynamics. In addition to WES feedback, we showed that North Pacific SSTAs triggered a robust SDC response during boreal fall 2015. As a result, the large-scale circulation anomalies drove surface wind anomalies along the equatorial Pacific and enhanced ocean forcing by 20% during this time period, potentially contributing to the extreme nature of the 2015-2016 El Niño.

By providing observational context, our analysis has highlighted several key points that should be considered in future research. First, we echo previous studies pointing to the impact of the tropical internal state on the efficacy of North Pacific teleconnections (e.g., Vimont et al. 2009; Alexander et al. 2010; Park et al. 2013). The atmospheric response to North Pacific SSTAs is small relative to similar perturbations in the tropics. Thus, the effectiveness of North Pacific teleconnections is heavily modulated by the timing of the signal's "arrival" relative to the timing of tropical noise, which can include atmospheric modulations across the tropics such as the Madden-Julian Oscillation (Kim et al. 2018) and the build-up or recent discharge of ocean heat content in the West Pacific upper ocean (Jin 1997).

Second, nPOGA focuses on North Pacific teleconnections; however, the South Pacific has also been shown to be an important source of equatorial Pacific variability (Zhang et al. 2014a; Lu et al. 2017; You and Furtado 2017; Larson et al. 2018). A more detailed analysis of observed South Pacific teleconnections and how they interact with signals from the North Pacific would improve our understanding of ENSO. As a result, we plan to analyze a South Pacific pacemaker experiment in a future study.

Finally, while our experimental design addresses many of the limitations found in previous studies (e.g., observed forcing, increased degrees of freedom), we acknowledge the well-known ENSO biases present in GFDL-CM2.1 (Wittenberg et al. 2006). Generally, GFDL-CM2.1 ENSO events are too strong, occur too frequently, and are not clearly seasonally phase locked. The fact that nPOGA exhibits such skill in spite of these model errors is a testament to the robust physical connection between the North and tropical Pacific. However, the possibility that our results may be model dependent cannot be completely ruled out. Therefore, a comprehensive comparison with other realistic models will be important moving forward.

5.7 Acknowledgements

D.J.A is supported by the National Science Foundation Graduate Research Fellowship (NSF; DGE-1144086). Y.K. is supported by the Japan Society for the Promotion of Science (18H01278 and 18H01281), the Japan Science and Technology Agency through Belmont Forum CRA "InterDec", and the Japan Ministry of Education, Culture, Sports, Science and Technology through the Integrated Research Program for Advancing Climate Models. S.P.X. and W.Z. are supported by the NSF (1637450). Y.Z. is supported by the China Scholarship Council (201706330016). A.J.M is supported by the NSF (OCE1419306) and the National Oceanic and Atmospheric Administration (NOAA; NA17OAR4310106). We would like to thank Manu Di Lorenzo, Giovanni Liguori, and Dan Vimont (who also served as a referee) for their helpful comments during the course of our study. We further thank two anonymous referees who provided additional insightful comments that greatly improved the clarity and focus of our results. We also express our gratitude to the World Climate Research Programme's Working Group on Coupled Modelling, which maintains CMIP.

Chapter 5, in part, has been submitted for publication of the material as it may appear in Amaya D. J., Y. Kosaka, W. Zhou, Y. Zhang, S. P. Xie, and A. J. Miller (2019), The North Pacific pacemaker effect on historical ENSO and its mechanisms. Journal of Climate. In revision. The dissertation author was the primary investigator and author of this paper.

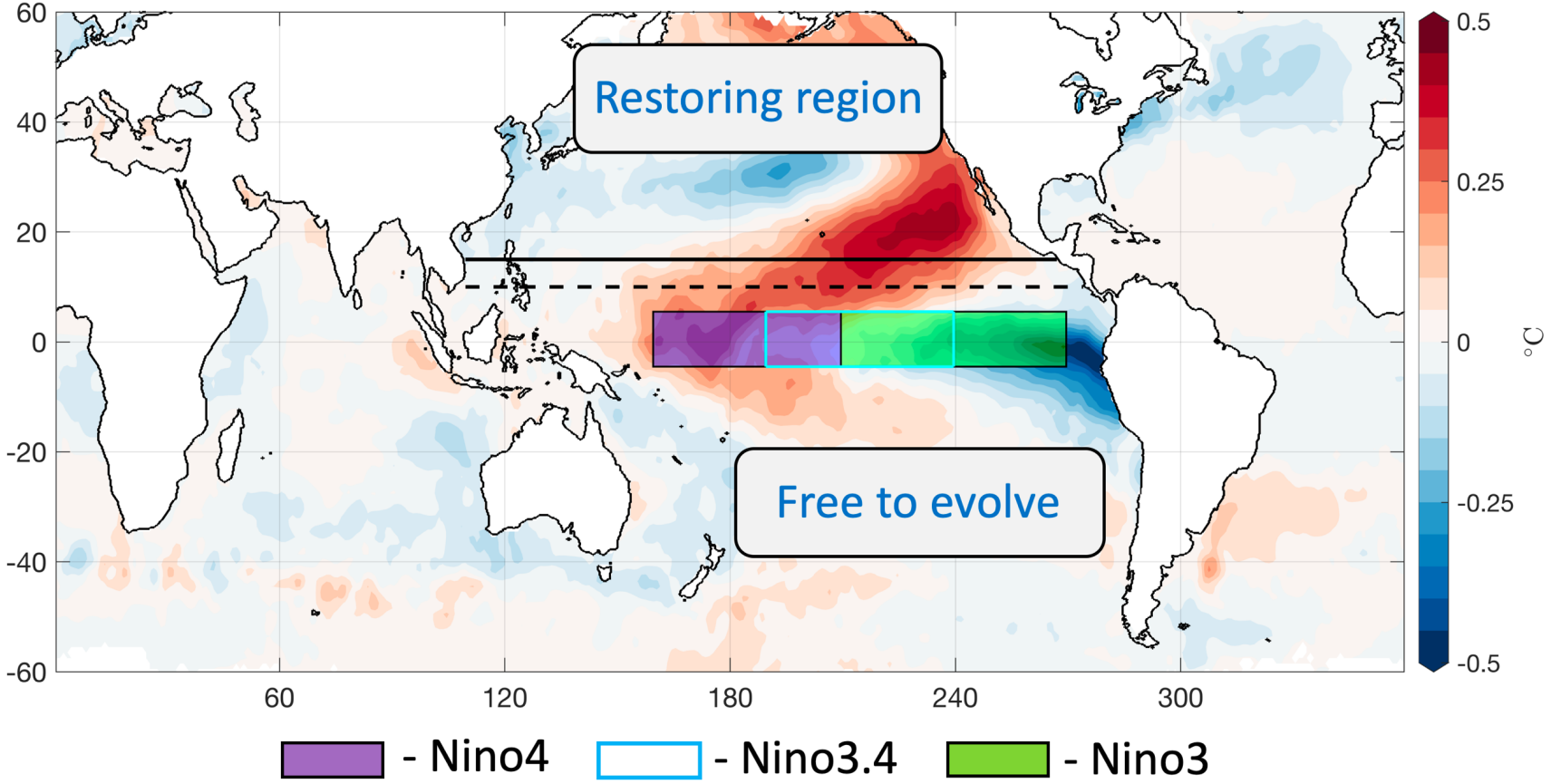

Figure 5.1: North Pacific Ocean-Global Atmosphere (nPOGA) experimental design. SSTs are restored to the model climatology plus historical anomaly in the Pacific Ocean north of 15˚N (solid black line). There is a 5˚ linearly decreasing buffer zone from 15˚N to 10˚N (dashed black line). Colored shading represents HadISST SSTAs regressed on the PMM_{CV} index. Shaded boxes indicate different Niño indices used in this study.

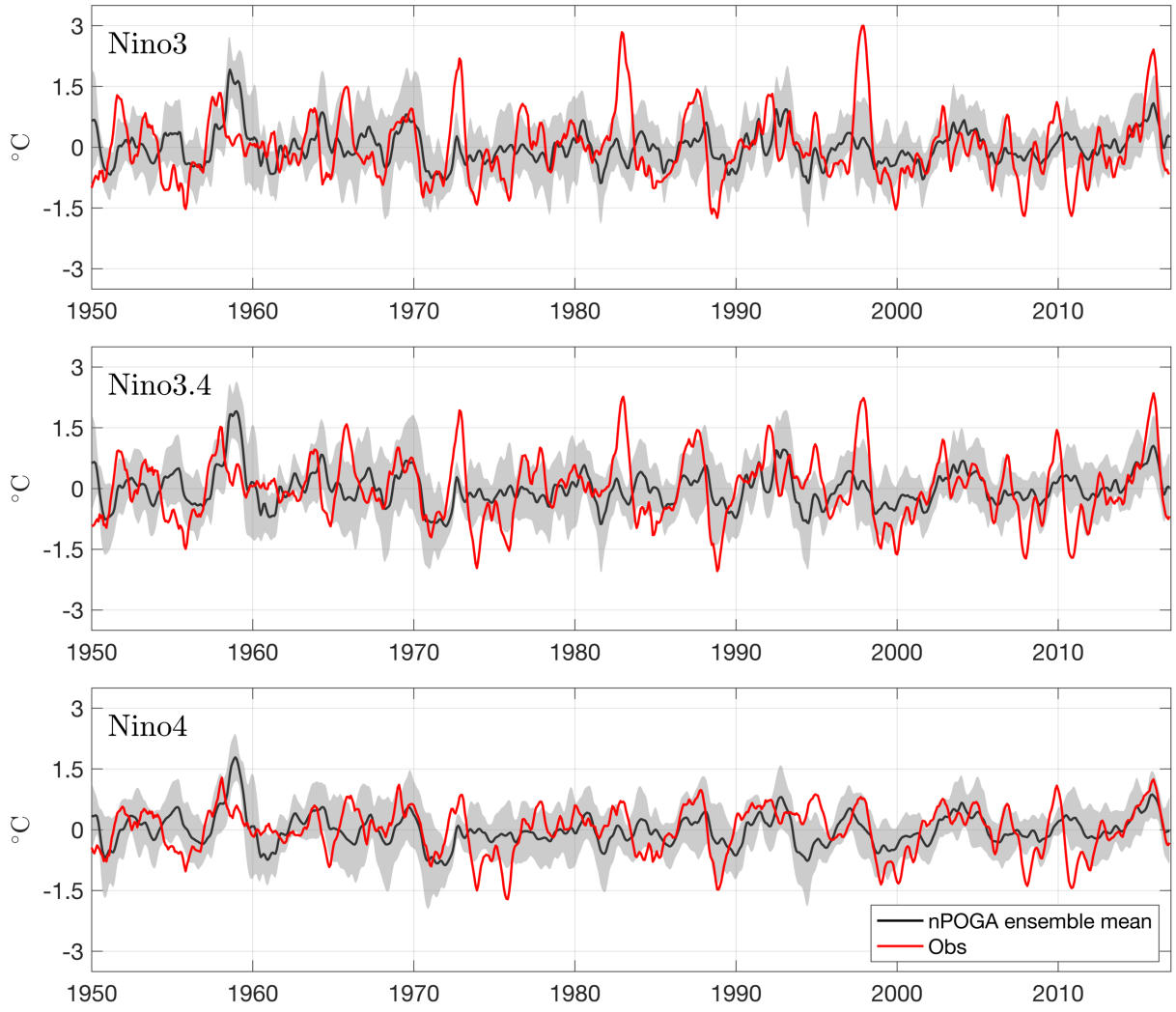

Figure 5.2: nPOGA and observed box averaged Niño indices (shown in Figure 5.1). Red line in each panel is the observed Niño index and the black line represents the nPOGA ensemble mean simulated Niño index. Shading denotes the 95% confidence ensemble standard error.

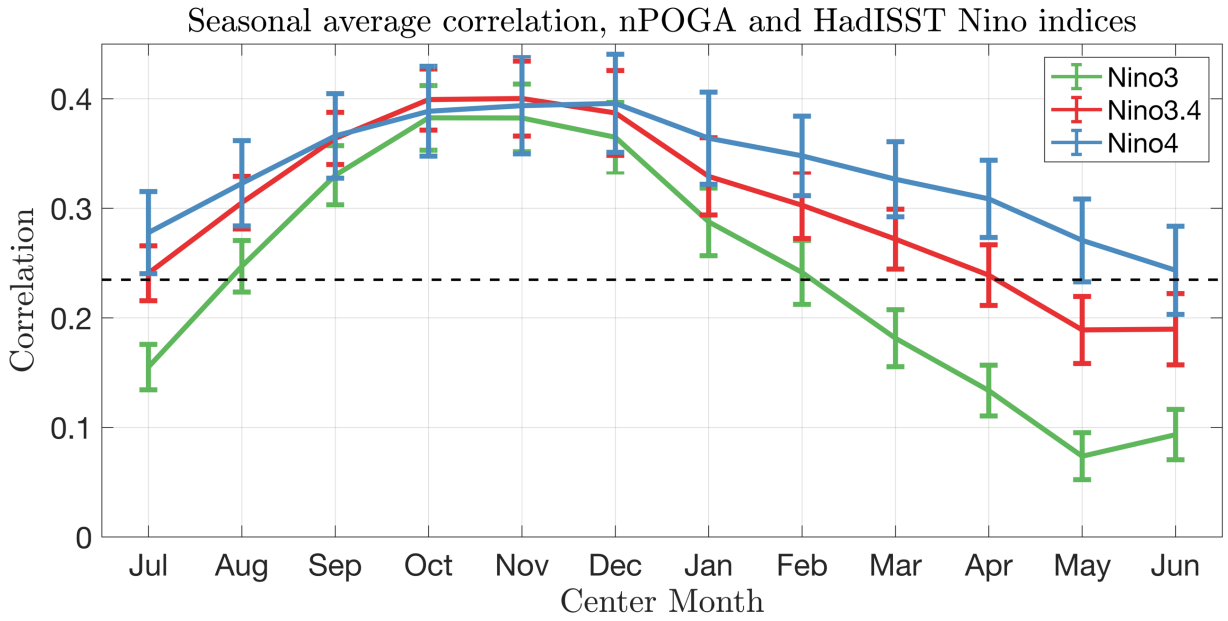

Figure 5.3: Seasonal average correlations of nPOGA and HadISST Niño indices. Error bars indicate the 95% confidence ensemble standard error, and the horizontal dashed line indicates a 95% significant correlation after accounting for lag-1 autocorrelation.

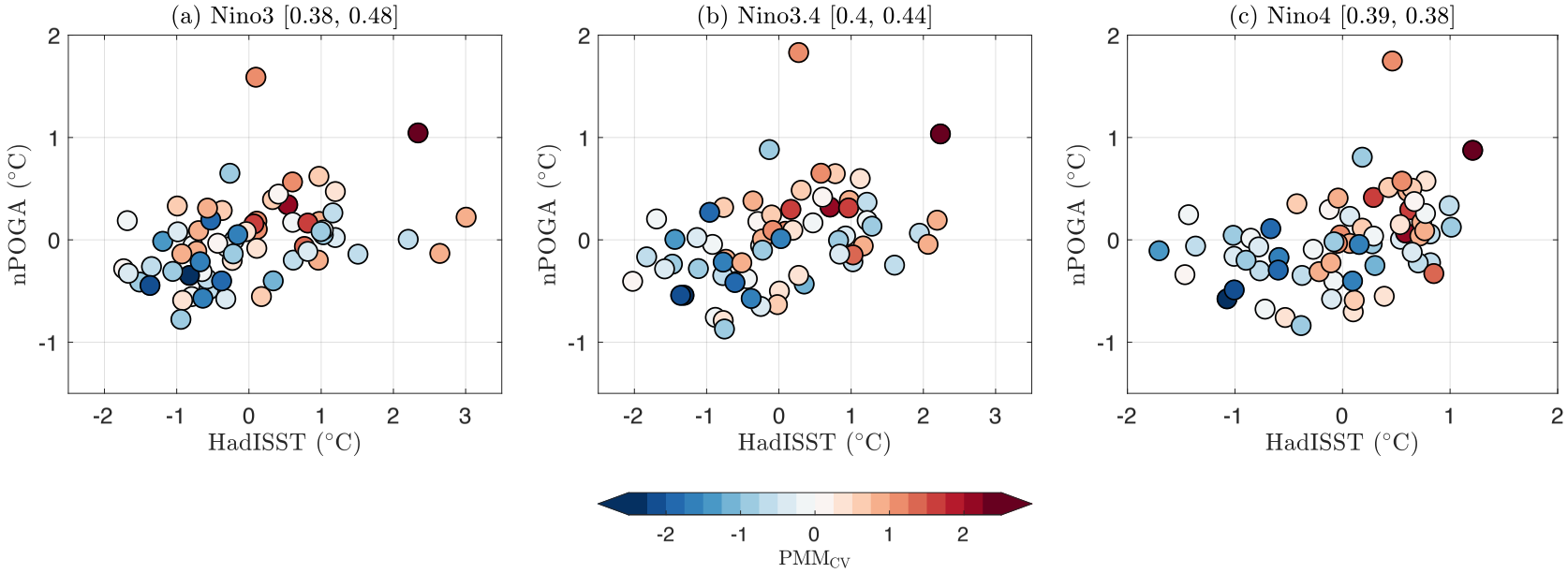

Figure 5.4: Scatter of OND Niño indices in HadISST (x-axis) versus ensemble average of nPOGA (y-axis). Shading of each circle indicates the magnitude of PMM$_{CV}$ in *preceding* FMA. The first number in each title is the correlation of ensemble mean nPOGA and observed ENSO for that index, and the second number is the correlation of OND nPOGA ENSO with the preceding FMA PMM$_{CV}$. All correlations are significant at the 95% confidence level.

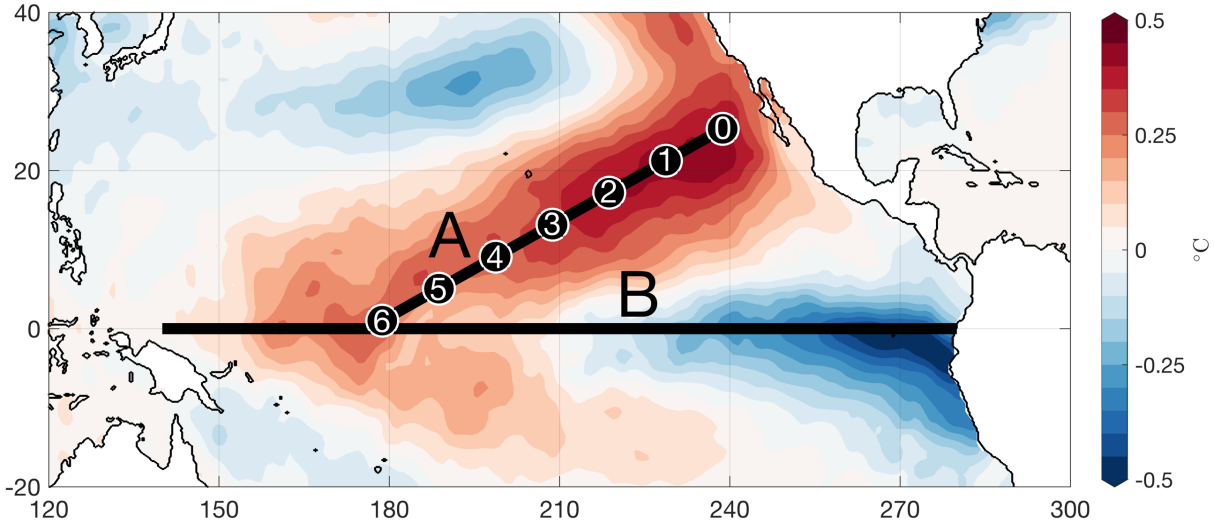

Figure 5.5: Schematic illustrating Hovmöller transect paths used for Figures 5.6, 5.7, 5.11, and 5.13. Path A follows northeast-to-southwest trajectory from point 0 at 25˚N, 122˚W to point 6 at 1˚N, 178˚W. Path B runs west-to-east along the equatorial Pacific Ocean averaged 3˚S-3˚N. Colored shading represents HadISST SSTAs regressed on the PMM_{CV} index.

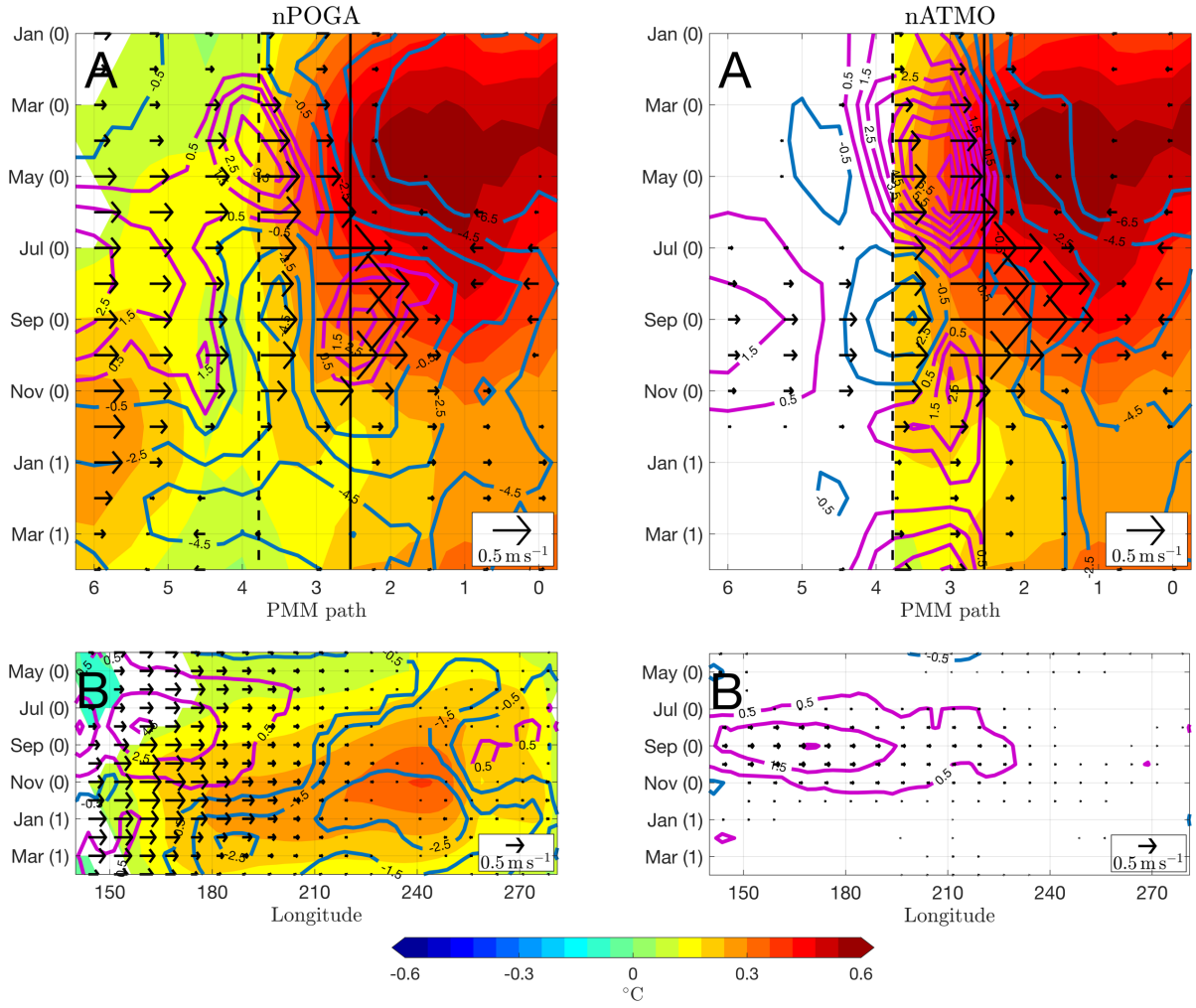

Figure 5.6: nPOGA (left column) and nATMO (right column) ensemble mean Hovmöllers composited on the PMM_{CV} index (see text), and following Paths A and B shown in Figure 5.5. Shading denotes SSTAs (˚C), colored contours indicate latent heat flux anomalies (W m^{-2}; positive downward), and arrows represent the zonal component of the 10m wind (m s^{-1}). The solid black line indicates the edge of the SST restoring region (see Section 5.2), and the dashed black line indicates the edge of the buffer zone. Results are shown only when significant at the 95% confidence level.

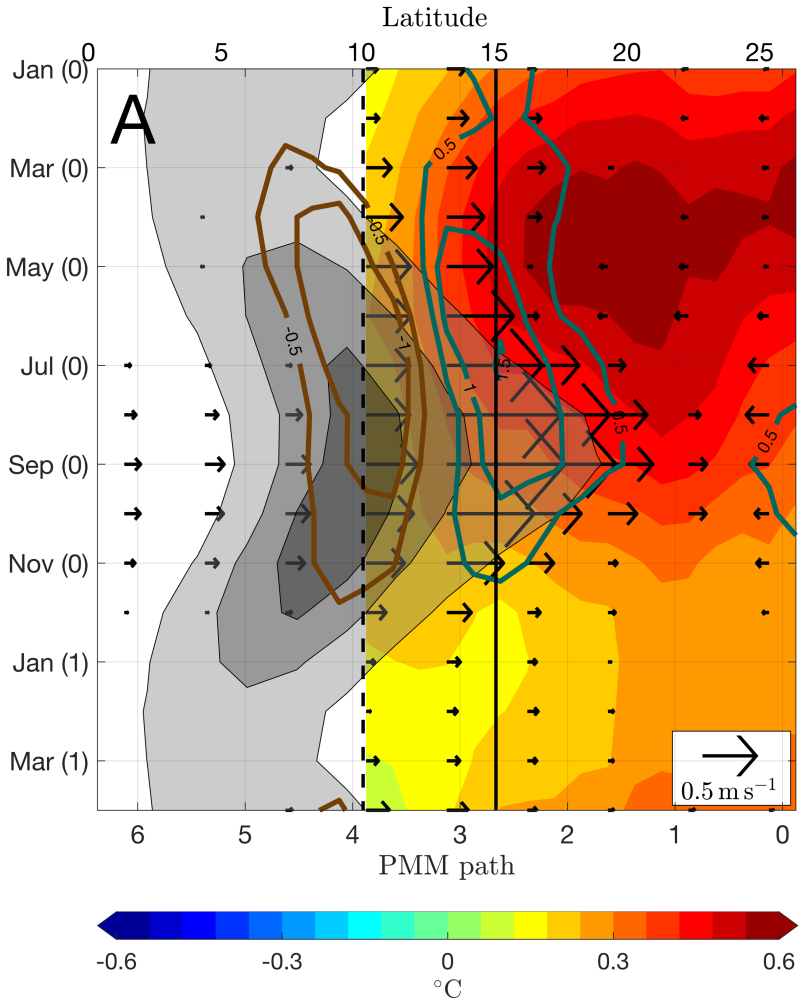

Figure 5.7: Same as Figure 5.6 (top right), except colored contours are now precipitation anomalies (mm day^{-1}). Gray shading denotes the climatological precipitation averaged in the Pacific 150˚E-100˚W (4, 8, and 12 mm day^{-1} from the light to heavy shading, respectively), representing the ITCZ. Note this gray shading follows the latitudinal lines indicated by the upper x-axis and is not averaged along Path A.

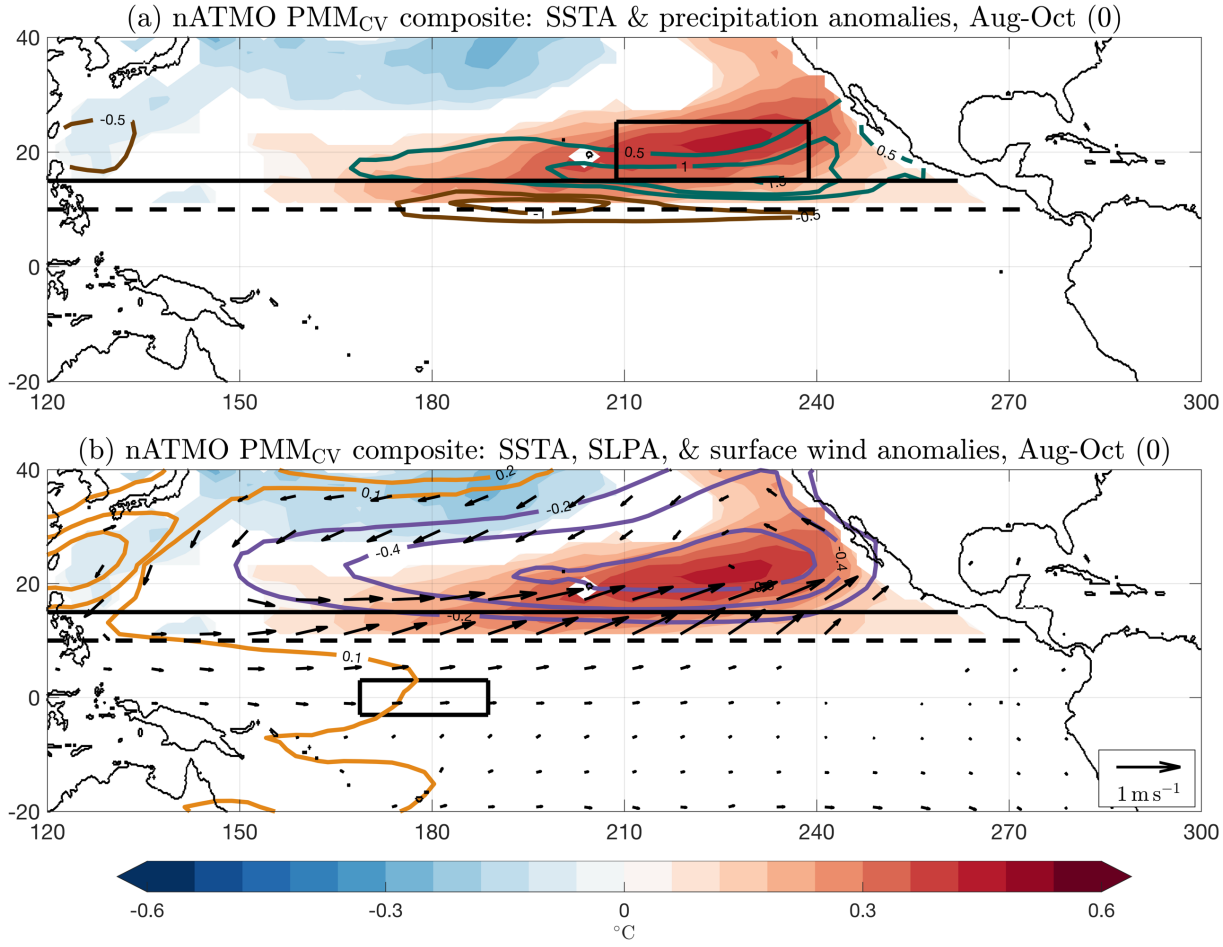

Figure 5.8: (a) nATMO ensemble mean SSTA (˚C; shading) and precipitation anomalies (mm day^{-1}; colored contours) composited on same PMM$_{CV}$ events as Figure 5.6, but for August-October (0). (b) Same SSTAs as in (a), overlaid with SLPA (hPa; colored contours) and 10m wind anomalies (m s^{-1}). Solid and shaded black horizontal lines denote the edge of the SST restoring region and buffer zone, respectively. Black boxes in (a) and (b) refer to calculations made for Figure 5.9 (see text).

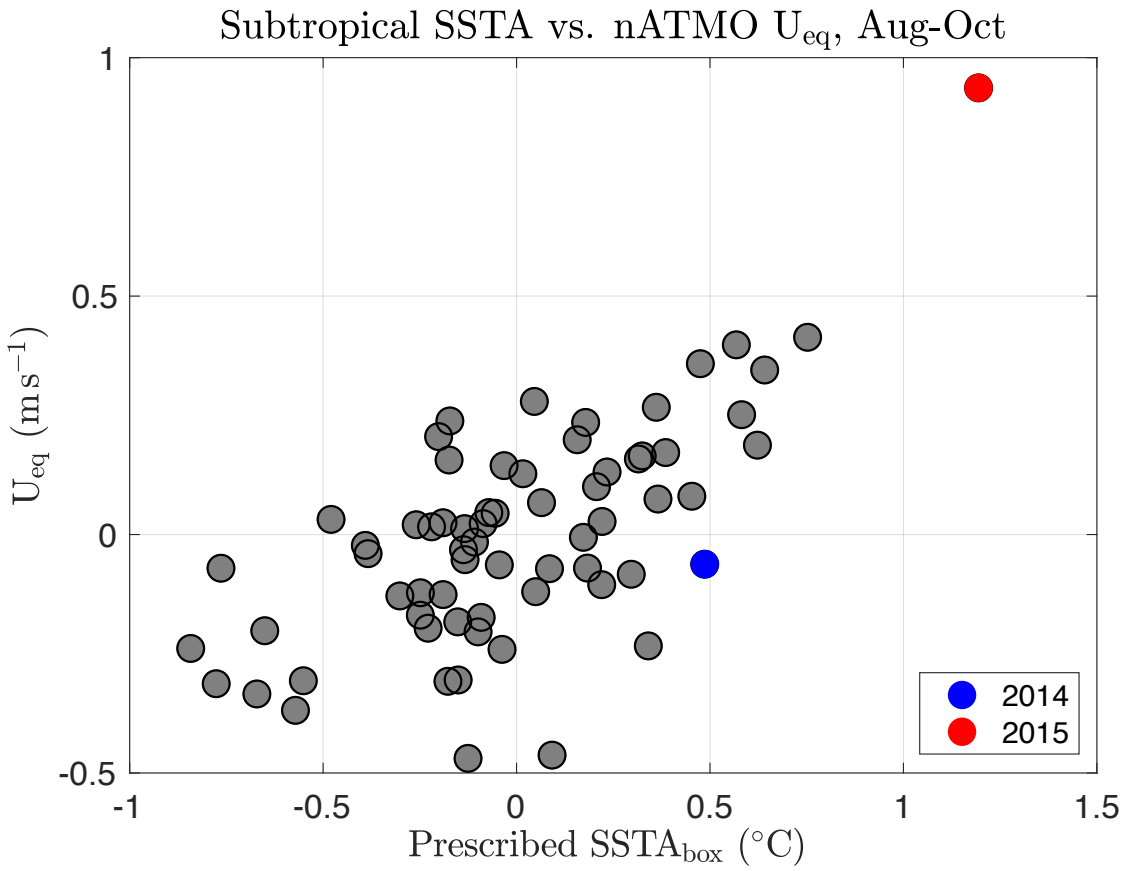

Figure 5.9: Scatter of SSTA (˚C) used to force nATMO, averaged in the subtropical black box in Figure 5.8a (x-axis), versus nATMO ensemble mean zonal wind anomalies (m s^{-1}) averaged in the equatorial black box in Figure 5.8b (y-axis). Blue and red dots represent values for 2014 and 2015, respectively.

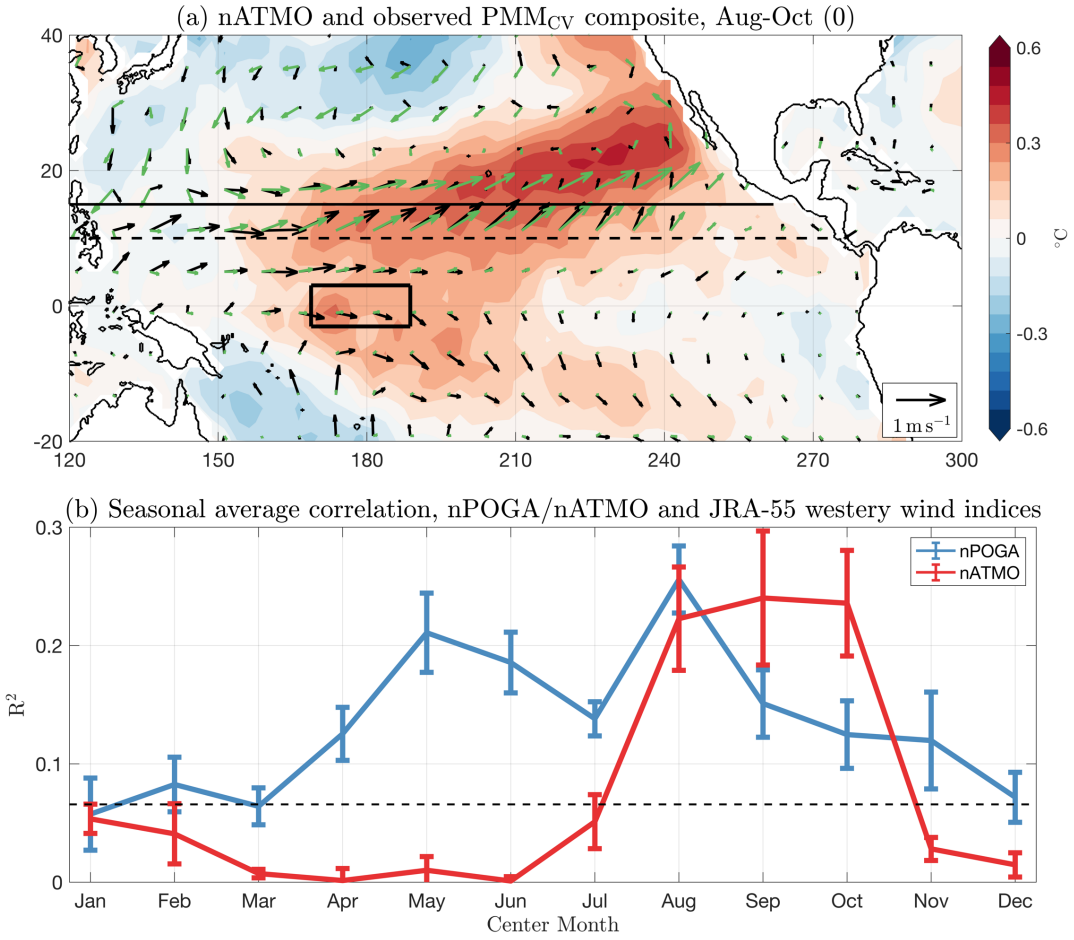

Figure 5.10: (a) Observed SSTA (°C; shading) and 10m wind anomalies (m s^{-1}; black arrows) composited on same PMM_{CV} events as in Figure 5.6, but for August-October (0). Green arrows are nATMO ensemble mean winds for the same composite period. (b) Seasonal R^2-value between JRA-55 U10 anomalies and nPOGA (blue) and nATMO (red) averaged in the equatorial black box in (a). Error bars indicate the 95% confidence ensemble standard error, and the horizontal dashed line indicates a 95% significant R^2-value after accounting for lag-1 autocorrelation.

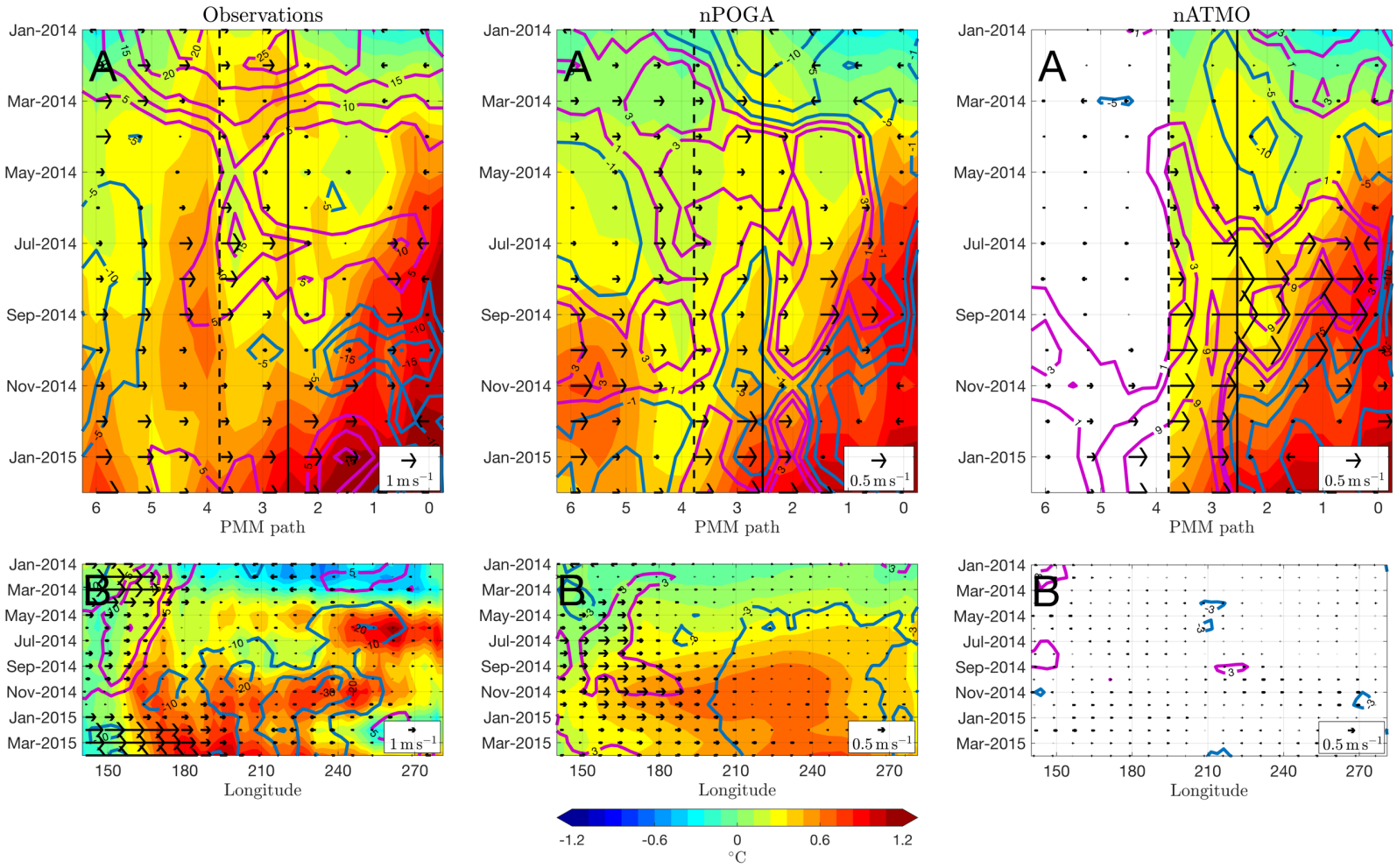

Figure 5.11: Same as Figure 5.6, except Hovmöllers across the 2014-2015 El Niño event in observations (left column), nPOGA ensemble mean (middle column), and nATMO (right column). For clarity, nPOGA and nATMO winds are scaled by 2 relative to observations.

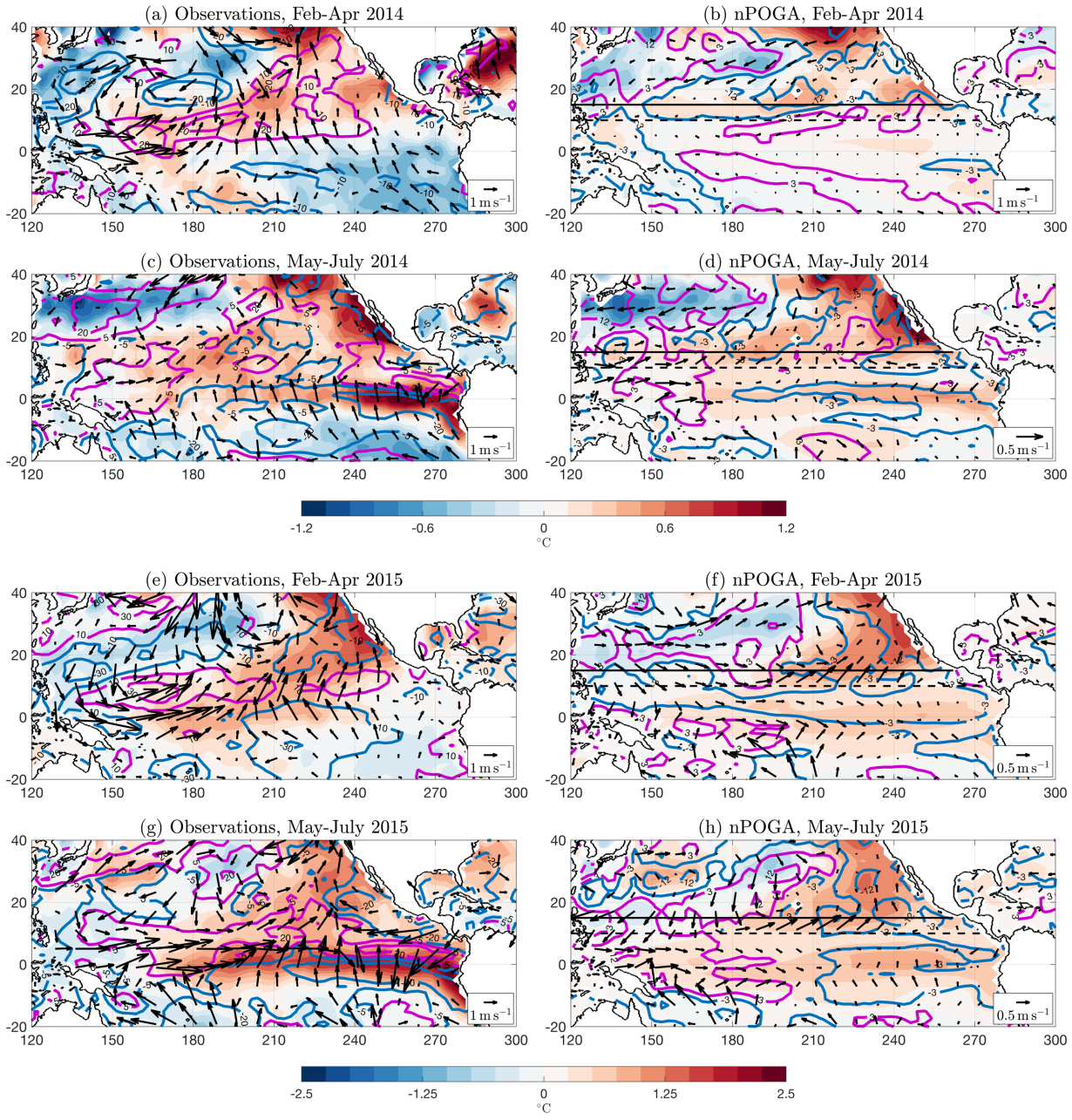

Figure 5.12: In all panels shading is SSTAs (˚C), black arrows are 10m wind anomalies (m s^{-1}), and colored contours are latent heat flux anomalies (W m^{-2}; positive downward). (a) and (c) show observations averaged for February-April 2014 and May-July 2014, respectively. (b) and (d) show nPOGA ensemble mean values averaged over the same seasons. (e)-(h) are of the same format as (a)-(d), but for 2015. For clarity, nPOGA winds are scaled by 2 relative to observations.

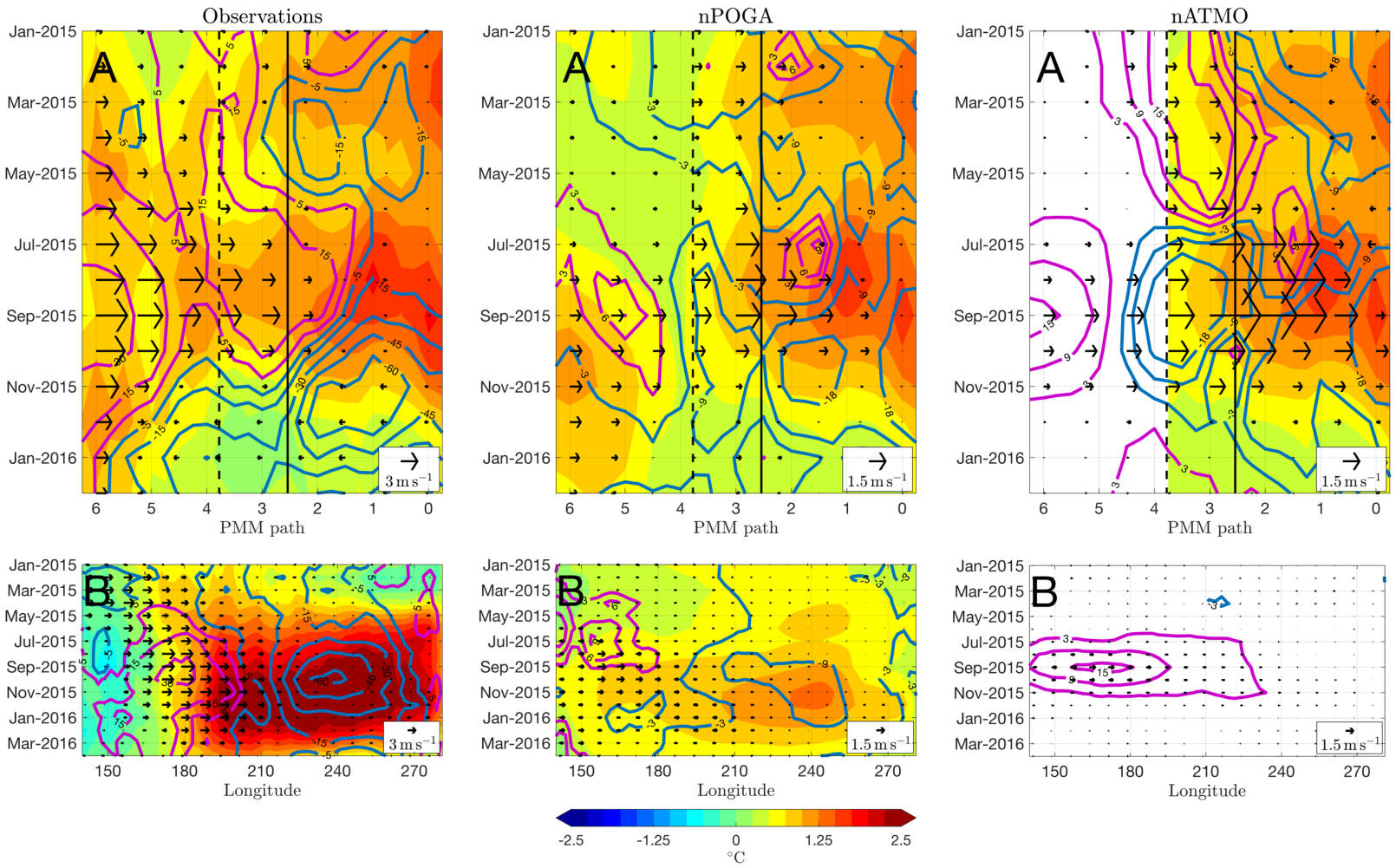

Figure 5.13: Same as Figure 5.11, except for the 2015-2016 El Niño event in observations (left column), nPOGA ensemble mean (middle column), and nATMO (right column). For clarity, nPOGA and nATMO winds are scaled by 2 relative to observations.

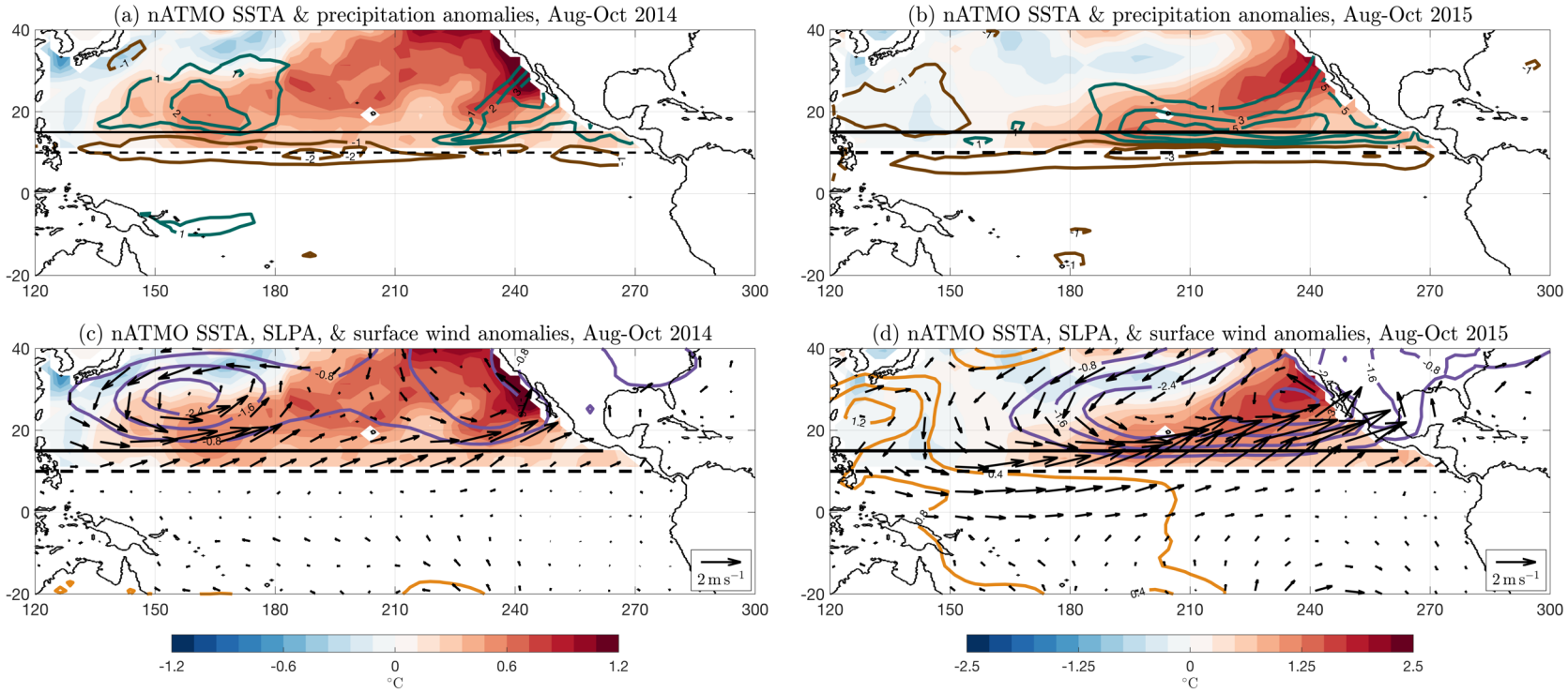

Figure 5.14: Same as Figure 5.8, except for August-October 2014 (a) and (c), August-October 2015 (b) and (d).

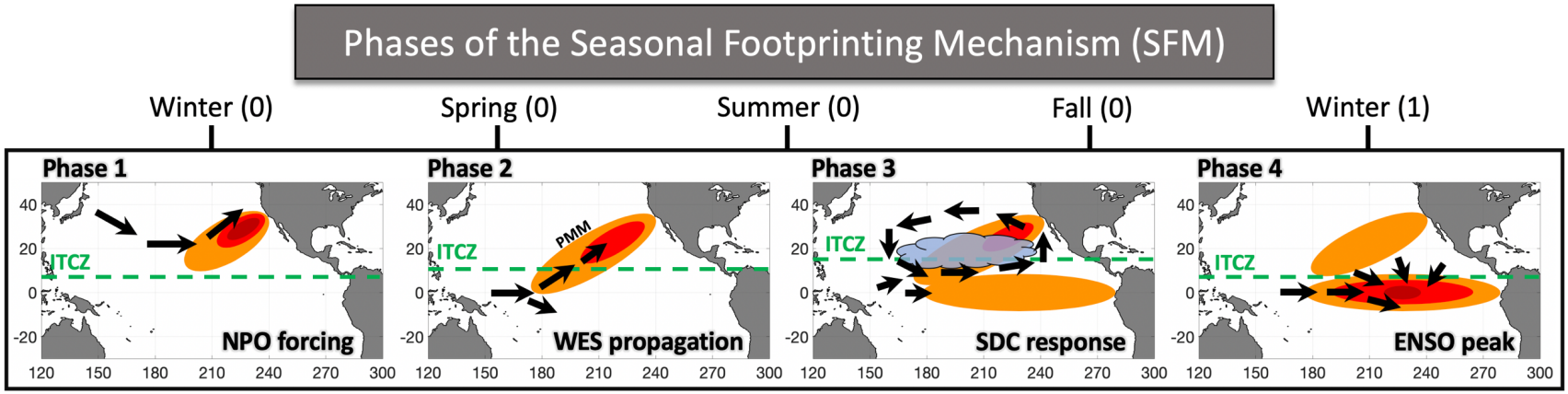

Figure 5.15: Schematic summarizing the Phases of the Seasonal Footprinting Mechanism (SFM) as described in this study. Colored shading denotes SSTAs. Black arrows are surface wind anomalies. Dashed green line is approximate position of the mean ITCZ. Shaded cloud represents anomalous precipitation. Upper axis depicts approximate timing of Phases from Winter of Year 0 to Winter of Year 1. Phases are as follows: *Phase 1* NPO-forced modulation of trade wind strength leaves SST "footprint" through anomalous latent heat flux. *Phase 2* Footprint SSTAs reinforced by mixed-layer feedbacks. Surface anomalies teleconnected to the deep tropics for the first time via PMM WES propagation mechanism, creating ENSO-favorable equatorial winds. *Phase 3* Mean ITCZ at northerly-most extent and sensitive to persistent PMM SSTAs. Surface anomalies teleconnected to the deep tropics for the second time via SDC response. ENSO conditions are reinforced. WES feedback and ENSO conditions are reinforced. *Phase 4* Subtropical anomalies dampen, Bjerknes feedback takes hold, and ENSO reaches its peak.

Chapter 6

Conclusions and comments

6.1 Summary of major contributions

In this dissertation, global coupled climate model simulations and modern observational data sets were utilized to investigate the physical underpinnings governing internal climate variability on seasonal-to-decadal timescales. The main objectives of this work focused on improved understanding of the two-way interactions between the tropics and extratropics through ocean-atmosphere teleconnections. We then further analyzed the multidecadal modulation of forced climate change signals by these internal variations.

In Chapter 2, we combine gridded ocean reanalysis data with in situ measurements from the TAO/TRITON buoy array to investigate multidecadal trends in ocean circulation along the equatorial Pacific. Our analysis showed that the wind-driven surface and subsurface ocean circulation effectively "spun-up" in response to a consistent increase in easterly wind stress from 1990-2009. It was found that equatorial surface waters were anomalously advected further westward during this time period, resulting in changes to surface SSH and the zonal thermocline depth gradient across the Pacific. As a result, the EUC intensified at a rate of 6.9 cm s^{-1} $decade^{-1}$ and equatorial upwelling increased at a rate of 2.0 x 10^{-4} cm s^{-1} $decade^{-1}$, which contributed to multidecadal cooling of tropical Pacific SST and, through atmospheric teleconnections, the global warming hiatus (Kosaka and Xie 2013). Further, we identified a seasonal dependence in these long-term trends, with the most significant trends occurring during boreal winter.

Motivated by the results of Chapter 2, the research presented in Chapter 3 sought to relate these decadal tropical Pacific SST trends to the observed expansion of the zonal mean Hadley Cell. To accomplish this goal, we developed a statistical technique that exploited a multivariate, cross-sectional view of the Hadley Cell edge to draw out leading modes of internal and forced Hadley Cell width variability from coupled climate simulations. We found that internal Hadley Cell width variations are strongly linked to tropical Pacific SST, while the long-term secular expansion of the Hadley Cell is related to prescribed historical forcings (e.g., greenhouse gas increase, ozone depletion, volcanic eruptions). Combined, the internal and forced modes explained 70% of interannual Hadley Cell width variations in the model. Additionally, we showed that the internal mode significantly modulates the rate of forced Hadley Cell width change in observations, such that the superposition of tropical Pacific forcing and anthropogenic forcing resulted in accelerated Hadley Cell expansion since 1980.

While Chapters 2 and 3 primarily focused on tropical Pacific climate modes and their impact on extratropical climate, Chapters 3 and 4 investigated mechanisms by which extratropical ocean-atmosphere variability can significantly influence tropical climate. In Chapter 3, we developed a novel statistical decomposition of lagged covariance matrices to isolate the spatiotemporal evolution of surface climate variables related to the AMM. Applying this technique to gridded reanalysis data sets revealed that an AMM event is initiated in boreal winter by stochastic extratropical atmospheric forcing, which generates SST anomalies in the subtropical surface ocean through turbulent heat flux anomalies. The SST anomalies are then amplified and translated southwestward into the deep tropics as the result of a series of air-sea interactions between surface winds, evaporation, and SST (e.g., WES feedback). A comparison to the CMIP5

archive reveals that climate models tend to poorly simulate these coupled feedbacks, which may be due to long-standing biases in tropical Atlantic SST and surface winds.

Chapter 4 explored these extratropical-tropical teleconnections further by quantifying the relationship between North Pacific ocean-atmosphere variability and the timing and magnitude of observed ENSO events. This was accomplished by using a fully-coupled climate model to produce the first ensemble of North Pacific SST pacemaker experiments (nPOGA). In these simulations, SST anomalies were restored back to the observed values within the North Pacific (>15˚N), but were free to evolve throughout the rest of the globe. Utilizing the nPOGA ensemble mean, we showed that teleconnections driven by North Pacific SST anomalies account for a significant fraction of observed ENSO variability since 1950, especially in boreal fall and winter. In particular, our simulations showed remarkable skill in reproducing the weak 2014-2015 El Niño and the extreme 2015-2016 El Niño. We further investigated the physical pathways that link North Pacific SST anomalies to tropical Pacific climate. They were: 1. A WES-driven propagation of surface anomalies associated with the PMM in boreal spring and summer, and 2. A Gill-like atmospheric response associated with anomalous deep convection in boreal summer and fall, which we refer to as the Summer Deep Convection (SDC) response.

6.2 Pathways forward

The research presented in this dissertation improves understanding of the physical mechanisms controlling key internal climate modes, and takes a significant step towards quantifying tropical-extratropical interactions. These results may improve the predictability of ENSO on seasonal timescales as well as enhance our understanding of the tropical Pacific ocean-atmosphere state during decadal transitions to hiatus periods. We further identify important

deficiencies in modern climate models that, if corrected, may improve the overall simulation of coupled climate variability. Additionally, our work illustrates the importance of internal noise in modulating forced climate signals, which can significantly impact public perception of climate change risk (e.g., as during the global warming hiatus).

Moving forward, there are several outstanding questions stemming from this dissertation that should be focus of future research. For example, to what extent does zonal mean Hadley Cell expansion project on regional scales where impacts are felt? Preliminary studies on this topic show promise in regressing regional variables of interest on zonal mean Hadley Cell width metrics (e.g., Schmidt and Grise 2017), while others have also made progress by decomposing the meridional streamfunction into regional components using the Helmholtz Decomposition (Staten et al. 2019). Regardless, future work is needed to elucidate the regional manifestation of the zonal mean Hadley Cell response to internal and forced variations.

With respect to the PMM-ENSO relationship outlined in Chapter 5, how would an altered tropical mean state impact North Pacific teleconnections to the tropics? Early work on this topic indicates that WES feedback may amplify as a result of global warming (Liguori and Di Lorenzo 2018; Sanchez et al. 2019), which implies a potential enhanced role for the PMM in future ENSO variability. However, climate model simulations also suggest that the distribution of ENSO events could fundamentally change in a warmer world (Cai et al. 2015), which would impact the PMM-ENSO relationship as well. Further, the northward positioned mean ITCZ has been shown to be a limiting factor in the PMM's interaction with the deep tropics (Zhang et al. 2014b). Paleoclimate proxy-based reconstructions of past hydroclimate change have revealed substantial meridional shifts in the zonal mean ITCZ in response to large-scale climate forcing (Schneider et al. 2014). Therefore, it is reasonable to hypothesize that the relative impact of the PMM on ENSO has not

been constant throughout history. Moving forward, it will become increasingly important to untangle these mean state relationships in past and future climates.

Finally, what role does the PMM play in tropical Pacific decadal climate variations and multiyear ENSO events? There is substantial evidence to suggest that the PMM can significantly contribute to tropical Pacific decadal variability (Di Lorenzo et al. 2015; You and Furtado 2018; Liguori and Di Lorenzo 2019); however, the importance of these interactions and the extent to which they may improve decadal predictability of the tropical Pacific remains unclear. Additionally, while most research has been focused on the PMM's impact on ENSO, there has been comparably less work on ENSO's influence on the PMM (Stuecker 2018). ENSO's projection on the NPO may reenergize subtropical coupled dynamics during boreal winter (Di Lorenzo et al. 2015). As a result, ENSO-forced PMM may play an important role in multiyear ENSO events (Yu and Fang 2018; DiNezio et al. 2017) and the transition between El Niño and La Niña (Park et al. 2013). Further investigation into these topics would improve our understanding of the PMM and its role in the climate system.

Chapter 7

References

Alexander, M. A., and J. D. Scott, 1997: Surface flux variability over the North Pacific and North Atlantic oceans. *J. Clim.*, **10**, 2963–2978, doi:10.1175/1520-0442(1997)010<2963:SFVOTN>2.0.CO;2.

——, D. J. Vimont, P. Chang, and J. D. Scott, 2010: The impact of extratropical atmospheric variability on ENSO: Testing the seasonal footprinting mechanism using coupled model experiments. *J. Clim.*, **23**, 2885–2901, doi:10.1175/2010JCLI3205.1.

Allen, R. J., and O. Ajoku, 2016: Future aerosol reductions and widening of the northern tropical belt. *J. Geophys. Res. Atmos.*, **121**, 6765–6786, doi:10.1002/2016JD024803.

——, and M. Kovilakam, 2017: The Role of Natural Climate Variability in Recent Tropical Expansion. *J. Clim.*, JCLI-D-16-0735.1, doi:10.1175/JCLI-D-16-0735.1.

——, S. C. Sherwood, J. R. Norris, and C. S. Zender, 2012: Recent Northern Hemisphere tropical expansion primarily driven by black carbon and tropospheric ozone. *Nature*, **485**, 350–354, doi:10.1038/nature11097.

——, J. R. Norris, and M. Kovilakam, 2014: Influence of anthropogenic aerosols and the Pacific Decadal Oscillation on tropical belt width. *Nat. Geosci.*, **7**, 270–274, doi:10.1038/ngeo2091.

Amaya, D. J., and G. R. Foltz, 2014: Impacts of canonical and Modoki El Niño on tropical Atlantic SST. *J. Geophys. Res. Ocean.*, **119**, 777–789, doi:10.1002/2013JC009476.

——, S. P. Xie, A. J. Miller, and M. J. McPhaden, 2015: Seasonality of tropical Pacific decadal trends associated with the 21st century global warming hiatus. *J. Geophys. Res. Ocean.*, **120**, 6782–6798, doi:10.1002/2015JC010906.

——, N. E. Bond, A. J. Miller, and M. J. Deflorio, 2016: The evolution and known atmospheric forcing mechanisms behind the 2013-2015 North Pacific warm anomalies. *US CLIVAR Var.*, **14**, 1–6.

——, M. J. DeFlorio, A. J. Miller, and S. P. Xie, 2017: WES feedback and the Atlantic Meridional Mode: observations and CMIP5 comparisons. *Clim. Dyn.*, **49**, 1665–1679, doi:10.1007/s00382-016-3411-1.

——, N. Siler, S. P. Xie, and A. J. Miller, 2018: The interplay of internal and forced modes of Hadley Cell expansion: lessons from the global warming hiatus. *Clim. Dyn.*, **51**, 305–319, doi:10.1007/s00382-017-3921-5.

Archer, C. L., and K. Caldeira, 2008: Historical trends in the jet streams. *Geophys. Res. Lett.*, **35**, L08803, doi:10.1029/2008GL033614.

Armour, K. C., J. Marshall, J. R. Scott, A. Donohoe, and E. R. Newsom, 2016: Southern Ocean warming delayed by circumpolar upwelling and equatorward transport. *Nat. Geosci.*, **9**, 549–554, doi:10.1038/ngeo2731.

Ashok, K., S. K. Behera, S. A. Rao, H. Weng, and T. Yamagata, 2007: El Niño Modoki and its possible teleconnection. *J. Geophys. Res. Ocean.*, **112**, C11007, doi:10.1029/2006JC003798.

Balmaseda, M. A., K. E. Trenberth, and E. Källén, 2013: Distinctive climate signals in reanalysis of global ocean heat content. *Geophys. Res. Lett.*, **40**, 1754–1759, doi:10.1002/grl.50382.

Barnston, A. G., and R. E. Livezey, 1987: Classification, Seasonality and Persistence of Low-Frequency Atmospheric Circulation Patterns. *Mon. Weather Rev.*, **115**, 1083–1126, doi:10.1175/1520-0493(1987)115<1083:csapol>2.0.co;2.

Barsugli, J. J., and D. S. Battisti, 1998: The Basic Effects of Atmosphere–Ocean Thermal Coupling on Midlatitude Variability*. *J. Atmos. Sci.*, **55**, 477–493, doi:10.1175/1520-0469(1998)055<0477:tbeoao>2.0.co;2.

Bender, F. A. M., V. Ramanathan, and G. Tselioudis, 2012: Changes in extratropical storm track cloudiness 1983-2008: Observational support for a poleward shift. *Clim. Dyn.*, **38**, 2037–2053, doi:10.1007/s00382-011-1065-6.

Bevan, J. M., and M. G. Kendall, 2006: *Rank Correlation Methods.* 74 pp.

Bjerknes, J., 1969: Atmospheric teleconnections from the equatorial Pacific. *Mon. Weather Rev.*, **97**, 163–172, doi:10.1175/1520-0493(1969)097<0163:ATFTEP>2.3.CO;2.

Bond, N. A., M. F. Cronin, H. Freeland, and N. J. Mantua, 2015: Causes and impacts of the 2014 warm anomaly in the NE Pacific. *Geophys. Res. Lett.*, **42**, 3414–3420, doi:10.1002/2015GL063306.

Bosilovich, M., and Coauthors, 2015: MERRA-2 : Initial Evaluation of the Climate. *NASA Tech. Rep. Ser. Glob. Model. Data Assim.*, **43**, doi:NASA/TM–2015-104606/Vol. 43.

Bretherton, C. S., C. Smith, and J. M. Wallace, 1992: An Intercomparison of Methods for Finding Coupled Patterns in Climate Data. *J. Clim.*, **5**, 541–560, doi:10.1175/1520-0442(1992)005<0541:AIOMFF>2.0.CO;2.

Breugem, W.-P., W. Hazeleger, and R. J. Haarsma, 2006: Multimodel study of tropical Atlantic variability and change. *Geophys. Res. Lett.*, **33**, 1–5, doi:10.1029/2006GL027831.

Brown, P. T., W. Li, and S.-P. Xie, 2015: Regions of significant influence on unforced global mean surface air temperature variability in climate models. *J. Geophys. Res. Atmos.*, **120**, 480–494, doi:10.1002/2014JD022576.

Cai, W., and Coauthors, 2015: ENSO and greenhouse warming. *Nat. Clim. Chang.*, **5**, 849–859, doi:10.1038/nclimate2743.

Capotondi, A., and Coauthors, 2015: Understanding enso diversity. *Bull. Am. Meteorol. Soc.*, **96**, 921–938, doi:10.1175/BAMS-D-13-00117.1.

Carton, J. A., and B. Huang, 2002: Warm Events in the Tropical Atlantic. *J. Phys. Oceanogr.*, **24**, 888–903, doi:10.1175/1520-0485(1994)024<0888:weitta>2.0.co;2.

Cayan, D. R., T. Das, D. W. Pierce, T. P. Barnett, M. Tyree, and A. Gershunov, 2010: Future dryness in the southwest US and the hydrology of the early 21st century drought. *Proc. Natl. Acad. Sci.*, **107**, 21271–21276, doi:10.1073/pnas.0912391107.

Chang, P., L. Ji, and H. Li, 1997: A decadal climate variation in the tropical Atlantic Ocean from thermodynamic air-sea interactions.[Letter]. *Nature*, **385**, 516–518.

——, L. Ji, and R. Saravanan, 2001: A hybrid coupled model study of tropical Atlantic variability. *J. Clim.*, **14**, 361–390, doi:10.1175/1520-0442(2001)013<0361:AHCMSO>2.0.CO;2.

——, L. Zhang, R. Saravanan, D. J. Vimont, J. C. H. Chiang, L. Ji, H. Seidel, and M. K. Tippett, 2007: Pacific meridional mode and El Niño - Southern oscillation. *Geophys. Res. Lett.*, **34**, 1–5, doi:10.1029/2007GL030302.

Chen, S., K. Wei, W. Chen, and L. Song, 2014: Regional changes in the annual mean hadley circulation in recent decades. *J. Geophys. Res.*, **119**, 7815–7832, doi:10.1002/2014JD021540.

Chen, X., and K.-K. Tung, 2014: Varying planetary heat sink led to global-warming slowdown and acceleration. *Science (80-.).*, **345**, 897–903, doi:10.1126/science.1254937.

Chen, X., and J. M. Wallace, 2015: ENSO-like variability: 1900-2013. *J. Clim.*, **28**, 9623–9641, doi:10.1175/JCLI-D-15-0322.1.

Chiang, J. C. H., and D. J. Vimont, 2004: Analogous Pacific and Atlantic meridional modes of tropical atmosphere-ocean variability. *J. Clim.*, **17**, 4143–4158, doi:10.1175/JCLI4953.1.

——, Y. Kushnir, and A. Giannini, 2002: Deconstructing Atlantic Intertropical Convergence Zone variability: Influence of the local cross-equatorial sea surface temperature gradient and remote forcing from the eastern equatorial Pacific. *J. Geophys. Res.*, **107**, doi:10.1029/2000jd000307.

Choi, J., S. W. Son, J. Lu, and S. K. Min, 2014: Further observational evidence of Hadley cell widening in the Southern Hemisphere. *Geophys. Res. Lett.*, **41**, 2590–2597, doi:10.1002/2014GL059426.

Clarke, A. J., 2014: El Niño Physics and El Niño Predictability. *Ann. Rev. Mar. Sci.*, doi:10.1146/annurev-marine-010213-135026.

Cohen, J. L., J. C. Furtado, M. Barlow, V. A. Alexeev, and J. E. Cherry, 2012: Asymmetric

seasonal temperature trends. *Geophys. Res. Lett.*, **39**, doi:10.1029/2011GL050582.

Cronin, M. F., and Coauthors, 2013: Formation and erosion of the seasonal thermocline in the Kuroshio Extension Recirculation Gyre. *Deep. Res. Part II Top. Stud. Oceanogr.*, **85**, 62–74, doi:10.1016/j.dsr2.2012.07.018.

CSIRO (Commonwealth Scientific and Industrial Research Organisation), 2012: Climate and Water Availability in South-eastern Australia: A Synthesis of Findings from Phase 2 of the South Eastern Australian Climate Initiative (SEACI). 41.

Czaja, A., P. van der Vaart, and J. Marshall, 2002: A diagnostic study of the role of remote forcing in tropical Atlantic variability. *J. Clim.*, **15**, 3280–3290, doi:10.1175/1520-0442(2002)015<3280:ADSOTR>2.0.CO;2.

Dai, A., J. C. Fyfe, S.-P. Xie, and X. Dai, 2015: Decadal modulation of global surface temperature by internal climate variability. *Nat. Clim. Chang.*, **5**, 555–559, doi:10.1038/nclimate2605.

Davis, N. A., and T. Birner, 2013: Seasonal to multidecadal variability of the width of the tropical belt. *J. Geophys. Res. Atmos.*, **118**, 7773–7787, doi:10.1002/jgrd.50610.

Davis, S. M., and K. H. Rosenlof, 2012: A multidiagnostic intercomparison of tropical-width time series using reanalyses and satellite observations. *J. Clim.*, **25**, 1061–1078, doi:10.1175/JCLI-D-11-00127.1.

Deflorio, M. J., S. J. Ghan, B. Singh, A. J. Miller, D. R. Cayan, L. M. Russell, and R. C. J. Somerville, 2014: Semidirect dynamical and radiative effect of north african dust transport on lower tropospheric clouds over the subtropical north atlantic in CESM 1.0. *J. Geophys. Res.*, **119**, 8284–8303, doi:10.1002/2013JD020997.

Delworth, T. L., and Coauthors, 2006: GFDL's CM2 Global Coupled Climate Models. Part I: Formulation and Simulation Characteristics. *J. Clim.*, **19**, 643–674, doi:10.1175/JCLI3629.1.

Deser, C., M. A. Alexander, S.-P. Xie, and A. S. Phillips, 2010: Sea Surface Temperature Variability: Patterns and Mechanisms. *Ann. Rev. Mar. Sci.*, **2**, 115–143, doi:10.1146/annurev-marine-120408-151453.

——, I. R. Simpson, K. A. McKinnon, and A. S. Phillips, 2017: The Northern Hemisphere extratropical atmospheric circulation response to ENSO: How well do we know it and how do we evaluate models accordingly? *J. Clim.*, **30**, 5059–5082, doi:10.1175/JCLI-D-16-0844.1.

DiNezio, P. N., C. Deser, Y. Okumura, and A. Karspeck, 2017: Predictability of 2-year La Niña events in a coupled general circulation model. *Clim. Dyn.*, **49**, 4237–4261, doi:10.1007/s00382-017-3575-3.

Drenkard, E. J., and K. B. Karnauskas, 2014: Strengthening of the pacific equatorial undercurrent in the SODA reanalysis: Mechanisms, ocean dynamics, and implications. *J. Clim.*, **27**, 2405–2416, doi:10.1175/JCLI-D-13-00359.1.

Easterling, D. R., and M. F. Wehner, 2009: Is the climate warming or cooling? *Geophys. Res. Lett.*, **36**, doi:10.1029/2009GL037810.

Enfield, D. B., and A. M. Mestas-Nuñez, 1999: Multiscale variabilities in global sea surface temperatures and their relationships with tropospheric climate patterns. *J. Clim.*, **12**, 2719–2733, doi:10.1175/1520-0442(1999)012<2719:MVIGSS>2.0.CO;2.

England, M. H., and Coauthors, 2014: Recent intensification of wind-driven circulation in the Pacific and the ongoing warming hiatus. *Nat. Clim. Chang.*, **4**, 222–227, doi:10.1038/nclimate2106.

Evan, A. T., R. J. Allen, R. Bennartz, and D. J. Vimont, 2013: The modification of sea surface temperature anomaly linear damping time scales by stratocumulus clouds. *J. Clim.*, **26**, 3619–3630, doi:10.1175/JCLI-D-12-00370.1.

Folland, C. K., 2002: Relative influences of the Interdecadal Pacific Oscillation and ENSO on the South Pacific Convergence Zone. *Geophys. Res. Lett.*, **29**, 1643, doi:10.1029/2001GL014201.

——, T. N. Palmer, and D. E. Parker, 1986: Sahel rainfall and worldwide sea temperatures, 1901-85. *Nature*, **320**, 602–607, doi:10.1038/320602a0.

Foltz, G. R., and M. J. McPhaden, 2010: Abrupt equatorial wave-induced cooling of the Atlantic cold tongue in 2009. *Geophys. Res. Lett.*, **37**, doi:10.1029/2010GL045522.

——, ——, and R. Lumpkin, 2012: A strong atlantic meridional mode event in 2009: The role of mixed: Layer dynamics. *J. Clim.*, **25**, 363–380, doi:10.1175/JCLI-D-11-00150.1.

——, C. Schmid, and R. Lumpkin, 2013: Seasonal cycle of the mixed layer heat budget in the northeastern tropical atlantic ocean. *J. Clim.*, **26**, 8169–8188, doi:10.1175/JCLI-D-13-00037.1.

Frankignoul, C., and E. Kestenare, 2005: Air-sea interactions in the tropical Atlantic: A view based on lagged rotated maximum covariance analysis. *J. Clim.*, **18**, 3874–3890, doi:10.1175/JCLI3498.1.

Frankignoul, C., E. Kestenare, M. Botzet, A. F. Carril, H. Drange, A. Pardaens, L. Terray, and R. Sutton, 2004: An intercomparison between the surface heat flux feedback in five coupled models, COADS and the NCEP reanalysis. *Clim. Dyn.*, **22**, 373–388, doi:10.1007/s00382-003-0388-3.

Fu, Q., and P. Lin, 2011: Poleward shift of subtropical jets inferred from satellite-observed lower-stratospheric temperatures. *J. Clim.*, **24**, 5597–5603, doi:10.1175/JCLI-D-11-00027.1.

Furtado, J. C., E. Di Lorenzo, B. T. Anderson, and N. Schneider, 2012: Linkages between the North Pacific Oscillation and central tropical Pacific SSTs at low frequencies. *Clim. Dyn.*, **39**, 2833–2846, doi:10.1007/s00382-011-1245-4.

Fyfe, J. C., and N. P. Gillett, 2014: Recent observed and simulated warming. *Nat. Clim. Chang.*, **4**, 150–151, doi:10.1038/nclimate2111.

——, and Coauthors, 2016: Making sense of the early-2000s warming slowdown. *Nat. Clim. Chang.*, **6**, 224–228, doi:10.1038/nclimate2938.

Garfinkel, C. I., D. W. Waugh, and L. M. Polvani, 2015: Recent Hadley cell expansion: The role of internal atmospheric variability in reconciling modeled and observed trends. *Geophys. Res. Lett.*, **42**, 10,824-10,831, doi:10.1002/2015GL066942.

Garreaud, R. D., and D. S. Battisti, 1999: Interannual (ENSO) and interdecadal (ENSO-like) variability in the Southern Hemisphere tropospheric circulation. *J. Clim.*, **12**, 2113–2123, doi:10.1175/1520-0442(1999)012<2113:IEAIEL>2.0.CO;2.

Gill, A. E., 1980: Some simple solutions for heat-induced tropical circulation. *Q. J. R. Meteorol. Soc.*, **106**, 447–462, doi:10.1002/qj.49710644905.

Grassi, B., G. Redaelli, P. O. Canziani, and G. Visconti, 2012: Effects of the PDO phase on the tropical belt width. *J. Clim.*, **25**, 3282–3290, doi:10.1175/JCLI-D-11-00244.1.

Guemas, V., F. J. Doblas-Reyes, I. Andreu-Burillo, and M. Asif, 2013: Retrospective prediction of the global warming slowdown in the past decade. *Nat. Clim. Chang.*, **3**, 649–653, doi:10.1038/nclimate1863.

Hansen, J., M. Sato, R. Ruedy, K. Lo, D. W. Lea, and M. Medina-Elizade, 2006: Global temperature change. *Proc. Natl. Acad. Sci.*, **103**, 14288–14293, doi:10.1073/pnas.0606291103.

——, R. Ruedy, M. Sato, and K. Lo, 2010: Global surface temperature change. *Rev. Geophys.*, **48**, doi:10.1029/2010RG000345.

——, M. Sato, P. Kharecha, and K. Von Schuckmann, 2011: Earth's energy imbalance and implications. *Atmos. Chem. Phys.*, **11**, 13421–13449, doi:10.5194/acp-11-13421-2011.

Hartmann, D. J., and Coauthors, 2013: Observations: Atmosphere and Surface. *Clim. Chang. 2013 Phys. Sci. Basis. Contrib. Work. Gr. I to Fifth Assess. Rep. Intergov. Panel Clim. Chang.*, 159–254, doi:10.1017/CBO9781107415324.008.

Hastenrath, S., and L. Heller, 1977: Dynamics of climatic hazards in northeast Brazil. *Q. J. R. Meteorol. Soc.*, **103**, 77–92, doi:10.1002/qj.49710343505.

Hoerling, M. P., J. Eischeid, J. Perlwitz, X. Quan, T. Zhang, and P. Pegion, 2012: On the increased frequency of mediterranean drought. *J. Clim.*, **25**, 2146–2161, doi:10.1175/JCLI-D-11-00296.1.

Horel, J. D., and J. M. Wallace, 1981: Planetary-scale phenomena associated with the Southern Oscillation. *Mon. Wea. Rev.*, **109**, 813–829, doi:10.1175/1520-0493(1981)109<0813:PSAPAW>2.0.CO;2.

Hu, S., and A. V. Fedorov, 2016: Exceptionally strong easterly wind burst stalling El Niño of 2014. *Proc. Natl. Acad. Sci.*, **113**, 2005–2010, doi:10.1073/pnas.1514182113.

——, and ——, 2017: The extreme El Niño of 2015–2016: the role of westerly and easterly wind bursts, and preconditioning by the failed 2014 event. *Climate Dynamics*.

——, and ——, 2018: Cross-equatorial winds control El Niño diversity and change. *Nat. Clim. Chang.*, **8**, 798–802, doi:10.1038/s41558-018-0248-0.

Hu, Y., and Q. Fu, 2007: Observed poleward expansion of the Hadley circulation since 1979. *Atmos. Chem. Phys. Discuss.*, **7**, 9367–9384, doi:10.5194/acpd-7-9367-2007.

Hu, Y., L. Tao, and J. Liu, 2013: Poleward expansion of the hadley circulation in CMIP5 simulations. *Adv. Atmos. Sci.*, **30**, 790–795, doi:10.1007/s00376-012-2187-4.

Hwang, Y.-T., S.-P. Xie, C. Deser, and S. M. Kang, 2017: Connecting Tropical Climate Change with Southern Ocean Heat Uptake. *Geophys. Res. Lett.*, 2017GL074972, doi:10.1002/2017GL074972.

Jin, F.-F., 1997: An Equatorial Ocean Recharge Paradigm for ENSO. Part I: Conceptual Model. *J. Atmos. Sci.*, **54**, 811–829, doi:10.1175/1520-0469(1997)054<0811:AEORPF>2.0.CO;2.

Johanson, C. M., and Q. Fu, 2009: Hadley cell widening: Model simulations versus observations. *J. Clim.*, **22**, 2713–2725, doi:10.1175/2008JCLI2620.1.

Johnson, G. C., B. M. Sloyan, W. S. Kessler, and K. E. McTaggart, 2002: Direct measurements of upper ocean currents and water properties across the tropical Pacific during the 1990s. *Prog. Oceanogr.*, **52**, 31–61, doi:10.1016/S0079-6611(02)00021-6.

Kalnay, E., and Coauthors, 1996: The NCEP/NCAR 40-year reanalysis project. *Bull. Am. Meteorol. Soc.*, **77**, 437–471, doi:10.1175/1520-0477(1996)077<0437:TNYRP>2.0.CO;2.

Kang, S. M., L. M. Polvani, J. C. Fyfe, and M. Sigmond, 2011: Impact of Polar Ozone Depletion on Subtropical Precipitation. *Science (80-.).*, **332**, 951–954, doi:10.1126/science.1202131.

Karl, T. R., and Coauthors, 2015: Possible artifacts of data biases in the recent global surface warming hiatus. *Science (80-.).*, **348**, 1469–1472, doi:10.1126/science.aaa5632.

Karnauskas, K. B., and C. C. Ummenhofer, 2014: On the dynamics of the Hadley circulation and subtropical drying. *Clim. Dyn.*, **42**, 2259–2269, doi:10.1007/s00382-014-2129-1.

Katsman, C. a, and G. J. Van Oldenborgh, 2011: Tracing the upper ocean ’s ‘missing heat.’ *Am. Geophys. Union*, **38**, 1–16, doi:10.1038/nature07080.Eden.

Kaufmann, R. K., H. Kauppi, M. L. Mann, and J. H. Stock, 2011: Reconciling anthropogenic climate change with observed temperature 1998-2008. *Proc. Natl. Acad. Sci. U. S. A.*, **108**, 11790–11793, doi:10.1073/pnas.1102467108.

Kay, J. E., and Coauthors, 2015: The community earth system model (CESM) large ensemble project : A community resource for studying climate change in the presence of internal climate variability. *Bull. Am. Meteorol. Soc.*, **96**, 1333–1349, doi:10.1175/BAMS-D-13-00255.1.

Keenlyside, N. S., M. Latif, J. Jungclaus, L. Kornblueh, and E. Roeckner, 2008: Advancing decadal-scale climate prediction in the North Atlantic sector. *Nature*, **453**, 84–88, doi:10.1038/nature06921.

Kim, H., F. Vitart, and D. E. Waliser, 2018: Prediction of the Madden–Julian Oscillation: A Review. *J. Clim.*, **31**, 9425–9443, doi:10.1175/JCLI-D-18-0210.1.

Kim, Y. H., S. K. Min, S. W. Son, and J. Choi, 2017: Attribution of the local Hadley cell widening in the Southern Hemisphere. *Geophys. Res. Lett.*, **44**, 1015–1024, doi:10.1002/2016GL072353.

Kintisch, E., 2014: Is Atlantic holding Earth's missing heat? *Science (80-.).*, **345**, 860–861, doi:10.1126/science.345.6199.860.

Kobayashi, S., and Coauthors, 2015: The JRA-55 Reanalysis: General Specifications and Basic Characteristics. *J. Meteorol. Soc. Japan. Ser. II*, **93**, 5–48, doi:10.2151/jmsj.2015-001.

Köhl, A., 2015: Evaluation of the GECCO2 ocean synthesis: Transports of volume, heat and freshwater in the atlantic. *Q. J. R. Meteorol. Soc.*, **141**, 166–181, doi:10.1002/qj.2347.

——, and D. Stammer, 2008: Variability of the Meridional Overturning in the North Atlantic from the 50-Year GECCO State Estimation. *J. Phys. Oceanogr.*, **38**, 1913–1930, doi:10.1175/2008jpo3775.1.

Kosaka, Y., and S.-P. Xie, 2013: Recent global-warming hiatus tied to equatorial Pacific surface cooling. *Nature*, **501**, 403–407, doi:10.1038/nature12534.

——, and ——, 2016: The tropical Pacific as a key pacemaker of the variable rates of global warming. *Nat. Geosci.*, **9**, 669–673, doi:10.1038/ngeo2770.

Kovilakam, M., and S. Mahajan, 2015: Black carbon aerosol-induced Northern Hemisphere tropical expansion. *Geophys. Res. Lett.*, **42**, 4964–4972, doi:10.1002/2015GL064559.

Larson, S. M., and B. P. Kirtman, 2014: The pacific meridional mode as an ENSO precursor and predictor in the North American multimodel ensemble. *J. Clim.*, **27**, 7018–7032, doi:10.1175/JCLI-D-14-00055.1.

——, K. V. Pegion, and B. P. Kirtman, 2018: The South Pacific meridional mode as a thermally driven source of ENSO amplitude modulation and uncertainty. *J. Clim.*, **31**, 5127–5145, doi:10.1175/JCLI-D-17-0722.1.

Lee, T., and M. J. McPhaden, 2010: Increasing intensity of El Niño in the central-equatorial Pacific. *Geophys. Res. Lett.*, **37**, 1–5, doi:10.1029/2010GL044007.

Levine, A. F. Z., and M. J. McPhaden, 2016: How the July 2014 easterly wind burst gave the 2015–2016 El Niño a head start. *Geophys. Res. Lett.*, **43**, 6503–6510, doi:10.1002/2016GL069204.

——, ——, and D. M. W. Frierson, 2017: The impact of the AMO on multidecadal ENSO variability. *Geophys. Res. Lett.*, doi:10.1002/2017GL072524.

Li, C., J. S. von Storch, and J. Marotzke, 2013: Deep-ocean heat uptake and equilibrium climate response. *Clim. Dyn.*, **40**, 1071–1086, doi:10.1007/s00382-012-1350-z.

Li, X., S. P. Xie, S. T. Gille, and C. Yoo, 2016: Atlantic-induced pan-tropical climate change over the past three decades. *Nat. Clim. Chang.*, **6**, 275–279, doi:10.1038/nclimate2840.

Liguori, G., and E. Di Lorenzo, 2018: Meridional Modes and Increasing Pacific Decadal Variability Under Anthropogenic Forcing. *Geophys. Res. Lett.*, **45**, 983–991, doi:10.1002/2017GL076548.

——, and ——, 2019: Separating the North and South Pacific Meridional Modes Contributions to ENSO and Tropical Decadal Variability. *Geophys. Res. Lett.*, **46**, 906–915, doi:10.1029/2018GL080320.

Lin, C.-Y., J.-Y. Yu, and H.-H. Hsu, 2015: CMIP5 model simulations of the Pacific meridional mode and its connection to the two types of ENSO. *Int. J. Climatol.*, **35**, 2352–2358, doi:10.1002/joc.4130.

Liu, H., C. Wang, S. K. Lee, and D. Enfield, 2013: Atlantic warm pool variability in the CMIP5 simulations. *J. Clim.*, **26**, 5315–5336, doi:10.1175/JCLI-D-12-00556.1.

Liu, Z., and S. Xie, 1994: Equatorward Propagation of Coupled Air–Sea Disturbances with Application to the Annual Cycle of the Eastern Tropical Pacific. *J. Atmos. Sci.*, **51**, 3807–3822, doi:10.1175/1520-0469(1994)051<3807:EPOCAD>2.0.CO;2.

Di Lorenzo, E., and N. Mantua, 2016: Multi-year persistence of the 2014/15 North Pacific marine heatwave. *Nat. Clim. Chang.*, **6**, 1042–1047, doi:10.1038/nclimate3082.

——, G. Liguori, N. Schneider, J. C. Furtado, B. T. Anderson, and M. A. Alexander, 2015: ENSO and meridional modes: A null hypothesis for Pacific climate variability. *Geophys. Res. Lett.*, **42**, 9440–9448, doi:10.1002/2015GL066281.

Lu, F., Z. Liu, Y. Liu, S. Zhang, and R. Jacob, 2017: Understanding the control of extratropical atmospheric variability on ENSO using a coupled data assimilation approach. *Clim. Dyn.*, **48**, 3139–3160, doi:10.1007/s00382-016-3256-7.

Lu, J., G. Chen, and D. M. W. Frierson, 2008: Response of the zonal mean atmospheric circulation to El Niño versus global warming. *J. Clim.*, **21**, 5835–5851, doi:10.1175/2008JCLI2200.1.

Lucas, C., and H. Nguyen, 2015: Regional charachteristics of tropical expansion and the role of climate variability. *J. Geophys. Res. Atmos.*, **120**, 1–16, doi:10.1002/2015JD023130.

——, B. Timbal, and H. Nguyen, 2014: The expanding tropics: A critical assessment of the observational and modeling studies. *Wiley Interdiscip. Rev. Clim. Chang.*, **5**, 89–112, doi:10.1002/wcc.251.

Ma, J., S. P. Xie, and H. Xu, 2017: Contributions of the North Pacific meridional mode to ensemble spread of ENSO prediction. *J. Clim.*, **30**, 9167–9181, doi:10.1175/JCLI-D-17-0182.1.

Maeda, S., Y. Urabe, K. Takemura, T. Yasuda, and Y. Tanimoto, 2016: Active Role of the ITCZ and WES Feedback in Hampering the Growth of the Expected Full-Fledged El Niño in 2014. *Sola*, **12**, 17–21, doi:10.2151/sola.2016-004.

Mantsis, D. F., S. C. Sherwood, R. J. Allen, and L. Shi, 2017: Natural variations of tropical width and recent trends. *Geophys. Res. Lett.*, doi:10.1002/2016GL072097.

Mantua, N. J., S. R. Hare, Y. Zhang, J. M. Wallace, and R. C. Francis, 1997: A Pacific Interdecadal Climate Oscillation with Impacts on Salmon Production. *Bull. Am. Meteorol. Soc.*, **78**, 1069–1079, doi:10.1175/1520-0477(1997)078<1069:APICOW>2.0.CO;2.

Marotzke, J., and P. M. Forster, 2015: Forcing, feedback and internal variability in global temperature trends. *Nature*, **517**, 565–570, doi:10.1038/nature14117.

Marshall, J., C. Hill, L. Perelman, and A. Adcroft, 1997: Hydrostatic, quasi-hydrostatic, and nonhydrostatic ocean modeling. *J. Geophys. Res. C Ocean.*, **102**, 5733–5752, doi:10.1029/96JC02776.

Martinez-Villalobos, C., and D. J. Vimont, 2017: An analytical framework for understanding tropical meridional modes. *J. Clim.*, **30**, 3303–3323, doi:10.1175/JCLI-D-16-0450.1.

McGregor, S., A. Timmermann, M. F. Stuecker, M. H. England, M. Merrifield, F.-F. Jin, and Y. Chikamoto, 2014: Recent Walker circulation strengthening and Pacific cooling amplified by Atlantic warming. *Nat. Clim. Chang.*, **4**, 888–892, doi:10.1038/nclimate2330.

McPhaden, M. J., and D. Zhang, 2004: Pacific Ocean circulation rebounds. *Geophys. Res. Lett.*, **31**, 4–7, doi:10.1029/2004GL020727.

——, and Coauthors, 1998: The Tropical Ocean-Global Atmosphere observing system: A decade of progress. *J. Geophys. Res. Ocean.*, **103**, 14169–14240, doi:10.1029/97JC02906.

——, T. Lee, and D. McClurg, 2011: El Niño and its relationship to changing background conditions in the tropical Pacific Ocean. *Geophys. Res. Lett.*, **38**, 2–5, doi:10.1029/2011GL048275.

Meehl, G. A., J. M. Arblaster, J. T. Fasullo, A. Hu, and K. E. Trenberth, 2011: Model-based evidence of deep-ocean heat uptake during surface-temperature hiatus periods. *Nat. Clim. Chang.*, **1**, 360–364, doi:10.1038/nclimate1229.

——, A. Hu, J. M. Arblaster, J. T. Fasullo, and K. E. Trenberth, 2013: Externally forced and internally generated decadal climate variability associated with the interdecadal pacific

oscillation. *J. Clim.*, **26**, 7298–7310, doi:10.1175/JCLI-D-12-00548.1.

Mehta, V. M., and T. Delworth, 1995: Decadal variability of the tropical Atlantic Ocean surface temperature in shipboard measurements and in a global ocean- atmosphere model. *J. Clim.*, **8**, 172–190, doi:10.1175/1520-0442(1995)008<0172:DVOTTA>2.0.CO;2.

Merrifield, M. A., P. R. Thompson, and M. Lander, 2012: Multidecadal sea level anomalies and trends in the western tropical Pacific. *Geophys. Res. Lett.*, **39**, doi:10.1029/2012GL052032.

Min, Q., J. Su, and R. Zhang, 2017: Impact of the south and north pacific meridional modes on the El Niño-Southern Oscillation: Observational analysis and comparison. *J. Clim.*, **30**, 1705–1720, doi:10.1175/JCLI-D-16-0063.1.

Min, S.-K., and S.-W. Son, 2013: Multimodel attribution of the Southern Hemisphere Hadley cell widening: Major role of ozone depletion. *J. Geophys. Res. Atmos.*, **118**, 3007–3015, doi:10.1002/jgrd.50232.

Morales, M. S., and Coauthors, 2012: Precipitation changes in the South American Altiplano since 1300AD reconstructed by tree-rings. *Clim. Past*, **8**, 653–666, doi:10.5194/cp-8-653-2012.

Newman, M., and Coauthors, 2016: The Pacific decadal oscillation, revisited. *J. Clim.*, **29**, 4399–4427, doi:10.1175/JCLI-D-15-0508.1.

Nguyen, H., A. Evans, C. Lucas, I. Smith, and B. Timbal, 2013: The hadley circulation in reanalyses: Climatology, variability, and Change. *J. Clim.*, **26**, 3357–3376, doi:10.1175/JCLI-D-12-00224.1.

Nobre, P., and J. Shukla, 1996: Variations of sea surface temperature, wind stress, and rainfall over the tropical Atlantic and South America. *J. Clim.*, **9**, 2464–2479, doi:10.1175/1520-0442(1996)009<2464:VOSSTW>2.0.CO;2.

Okumura, Y., S. P. Xie, A. Numaguti, and Y. Tanimoto, 2001: Tropical Atlantic air-sea interaction and its influence on the NAO. *Geophys. Res. Lett.*, **28**, 1507–1510, doi:10.1029/2000GL012565.

Park, J. Y., S. W. Yeh, J. S. Kug, and J. Yoon, 2013: Favorable connections between seasonal footprinting mechanism and El Niño. *Clim. Dyn.*, **40**, 1169–1181, doi:10.1007/s00382-012-1477-y.

Pohlmann, H., J. H. Jungclaus, A. Köhl, D. Stammer, and J. Marotzke, 2009: Initializing decadal climate predictions with the GECCO oceanic synthesis: Effects on the North Atlantic. *J. Clim.*, **22**, 3926–3938, doi:10.1175/2009JCLI2535.1.

Polo, I., B. Rodríguez-Fonseca, T. Losada, and J. García-Serrano, 2008: Tropical atlantic variability modes (1979-2002). Part I: Time-evolving SST modes related to West African rainfall. *J. Clim.*, **21**, 6457–6475, doi:10.1175/2008JCLI2607.1.

Polvani, L. M., M. Previdi, and C. Deser, 2011a: Large cancellation, due to ozone recovery, of

future Southern Hemisphere atmospheric circulation trends. *Geophys. Res. Lett.*, **38**, doi:10.1029/2011GL046712.

——, D. W. Waugh, G. J. P. Correa, and S.-W. Son, 2011b: Stratospheric Ozone Depletion: The Main Driver of Twentieth-Century Atmospheric Circulation Changes in the Southern Hemisphere. *J. Clim.*, **24**, 795–812, doi:10.1175/2010JCLI3772.1.

Power, S., T. Casey, C. Folland, A. Colman, and V. Mehta, 1999: Inter-decadal modulation of the impact of ENSO on Australia. *Clim. Dyn.*, **15**, 319–324, doi:10.1007/s003820050284.

Previdi, M., and B. G. Liepert, 2007: Annular modes and Hadley cell expansion under global warming. *Geophys. Res. Lett.*, **34**, doi:10.1029/2007GL031243.

Richter, I., S. K. Behera, T. Doi, B. Taguchi, Y. Masumoto, and S.-P. Xie, 2014: What controls equatorial Atlantic winds in boreal spring? *Clim. Dyn.*, **43**, 3091–3104, doi:10.1007/s00382-014-2170-0.

Riehl, H., 1950: On the Role of the Tropics in the General Circulation of the Atmosphere. *Tellus*, **2**, 1–17, doi:10.1111/j.2153-3490.1950.tb00306.x.

Robinson, W. A., 2002: On the midlatitude thermal response to tropical warmth. *Geophys. Res. Lett.*, **29**, 31, doi:10.1029/2001GL014158.

Rogers, J. C., 1981: The North Pacific Oscillation. *J. Climatol.*, doi:10.1002/joc.3370010106.

Ruiz-Barradas, A., J. A. Carton, and S. Nigam, 2003: Role of the atmosphere in climate variability of the tropical Atlantic. *J. Clim.*, **16**, 2052–2065, doi:10.1175/1520-0442(2003)016<2052:ROTAIC>2.0.CO;2.

Sanchez, S. C., D. J. Amaya, A. J. Miller, S.-P. Xie, and C. D. Charles, 2019: The Pacific Meridional Mode over the last millennium. *Clim. Dyn.*, doi:10.1007/s00382-019-04740-1.

Schmidt, D. F., and K. M. Grise, 2017: The Response of Local Precipitation and Sea Level Pressure to Hadley Cell Expansion. *Geophys. Res. Lett.*, **44**, 10,573-10,582, doi:10.1002/2017GL075380.

Schneider, T., T. Bischoff, and G. H. Haug, 2014: Migrations and dynamics of the intertropical convergence zone. *Nature*, **513**, 45–53, doi:10.1038/nature13636.

Seager, R., N. Harnik, Y. Kushnir, W. A. Robinson, and J. Miller, 2003: Mechanisms of hemispherically symmetric climate variability. *J. Clim.*, **16**, 2960–2978, doi:10.1175/1520-0442(2003)016<2960:MOHSCV>2.0.CO;2.

——, N. Naik, and G. A. Vecchi, 2010: Thermodynamic and dynamic mechanisms for large-scale changes in the hydrological cycle in response to global warming. *J. Clim.*, **23**, 4651–4668, doi:10.1175/2010JCLI3655.1.

Seidel, D. J., and W. J. Randel, 2006: Variability and trends in the global tropopause estimated

from radiosonde data. *J. Geophys. Res. Atmos.*, **111**, D21101, doi:10.1029/2006JD007363.

——, Q. Fu, W. J. Randel, and T. J. Reiohler, 2008: Widening of the tropical belt in a changing climate. *Nat. Methods*, **1**, 21–24, doi:10.1038/ngeo.2007.38.

Shepherd, T. G., 2014: Atmospheric circulation as a source of uncertainty in climate change projections. *Nat. Geosci.*, **7**, 703–708, doi:10.1038/NGEO2253.

Shin, S. J., and S. Il An, 2018: Interdecadal Change in the Relationship Between the North Pacific Oscillation and the Pacific Meridional Mode and Its Impact on ENSO. *Asia-Pacific J. Atmos. Sci.*, **54**, 63–76, doi:10.1007/s13143-017-0060-1.

Siler, N., Y. Kosaka, S. P. Xie, and X. Li, 2017: Tropical ocean contributions to California's surprisingly dry El Niño of 2015/16. *J. Clim.*, **30**, 10067–10079, doi:10.1175/JCLI-D-17-0177.1.

Smith, D. M., S. Cusack, A. W. Colman, C. K. Folland, G. R. Harris, and J. M. Murphy, 2007: Improved surface temperature prediction for the coming decade from a global climate model. *Science (80-.).*, **317**, 796–799, doi:10.1126/science.1139540.

Smith, T. M., R. W. Reynolds, T. C. Peterson, and J. Lawrimore, 2008: Improvements to NOAA's historical merged land-ocean surface temperature analysis (1880-2006). *J. Clim.*, **21**, 2283–2296, doi:10.1175/2007JCLI2100.1.

Solomon, S., K. H. Rosenlof, R. W. Portmann, J. S. Daniel, S. M. Davis, T. J. Sanford, and G. K. Plattner, 2010: Contributions of stratospheric water vapor to decadal changes in the rate of global warming. *Science (80-.).*, **327**, 1219–1223, doi:10.1126/science.1182488.

Solomon, S., J. S. Daniel, R. R. Neely, J. P. Vernier, E. G. Dutton, and L. W. Thomason, 2011: The persistently variable "background" stratospheric aerosol layer and global climate change. *Science (80-.).*, **333**, 866–870, doi:10.1126/science.1206027.

Sousa, P. M., R. M. Trigo, P. Aizpurua, R. Nieto, L. Gimeno, and R. Garcia-Herrera, 2011: Trends and extremes of drought indices throughout the 20th century in the Mediterranean. *Nat. Hazards Earth Syst. Sci.*, **11**, 33–51, doi:10.5194/nhess-11-33-2011.

Staten, P. W., K. M. Grise, S. M. Davis, K. Karnauskas, and N. Davis, 2019: Regional Widening of Tropical Overturning: Forced Change, Natural Variability, and Recent Trends. *J. Geophys. Res. Atmos.*, doi:10.1029/2018JD030100.

Sterl, A., 2004: On the (in)homogeneity of reanalysis products. *J. Clim.*, **17**, 3866–3873, doi:10.1175/1520-0442(2004)017<3866:OTIORP>2.0.CO;2.

Stuecker, M. F., 2018: Revisiting the Pacific Meridional Mode. *Sci. Rep.*, **8**, doi:10.1038/s41598-018-21537-0.

Sutton, R. T., S. P. Jewson, and D. P. Rowell, 2000: The elements of climate variability in the tropical Atlantic region. *J. Clim.*, **13**, 3261–3284, doi:10.1175/1520-

0442(2000)013<3261:TEOCVI>2.0.CO;2.

Takahashi, C., and M. Watanabe, 2016: Pacific trade winds accelerated by aerosol forcing over the past two decades. *Nat. Clim. Chang.*, **6**, 768–774, doi:10.1038/nclimate2996.

Tanimoto, Y., and S.-P. Xie, 2004: Inter-hemispheric Decadal Variations in SST, Surface Wind, Heat Flux and Cloud Cover over the Atlantic Ocean. *J. Meteorol. Soc. Japan*, **80**, 1199–1219, doi:10.2151/jmsj.80.1199.

Tao, L., Y. Hu, and J. Liu, 2016: Anthropogenic forcing on the Hadley circulation in CMIP5 simulations. *Clim. Dyn.*, **46**, 3337–3350, doi:10.1007/s00382-015-2772-1.

Taylor, K. E., R. J. Stouffer, and G. A. Meehl, 2012: An overview of CMIP5 and the experiment design. *Bull. Am. Meteorol. Soc.*, **93**, 485–498, doi:10.1175/BAMS-D-11-00094.1.

Trenberth, K. E., D. P. Stepaniak, J. W. Hurrell, M. Fiorino, K. E. Trenberth, D. P. Stepaniak, J. W. Hurrell, and M. Fiorino, 2001: Quality of Reanalyses in the Tropics. *J. Clim.*, **14**, 1499–1510, doi:10.1175/1520-0442(2001)014<1499:QORITT>2.0.CO;2.

——, J. T. Fasullo, G. Branstator, and A. S. Phillips, 2014: Seasonal aspects of the recent pause in surface warming. *Nat. Clim. Chang.*, **4**, 911–916, doi:10.1038/nclimate2341.

Vimont, D. J., 2010: Transient growth of thermodynamically coupled variations in the tropics under an equatorially symmetric mean state. *J. Clim.*, **23**, 5771–5789, doi:10.1175/2010JCLI3532.1.

——, and J. P. Kossin, 2007: The Atlantic Meridional Mode and hurricane activity. *Geophys. Res. Lett.*, **34**, doi:10.1029/2007GL029683.

——, D. S. Battisti, and A. C. Hirst, 2001: Footprinting: A seasonal connection between the tropics and mid-latitudes. *Geophys. Res. Lett.*, **28**, 3923–3926, doi:10.1029/2001GL013435.

——, ——, and ——, 2003a: The seasonal footprinting mechanism in the CSIRO general circulation models. *J. Clim.*, doi:10.1175/1520-0442(2003)016<2653:TSFMIT>2.0.CO;2.

——, J. M. Wallace, and D. S. Battisti, 2003b: The seasonal footprinting mechanism in the Pacific: Implications for ENSO. *J. Clim.*, **16**, 2668–2675, doi:10.1175/1520-0442(2003)016<2668:TSFMIT>2.0.CO;2.

——, M. A. Alexander, and A. Fontaine, 2009: Midlatitude excitation of tropical variability in the pacific: The role of thermodynamic coupling and seasonality. *J. Clim.*, **22**, 518–534, doi:10.1175/2008JCLI2220.1.

——, ——, and M. Newman, 2014: Optimal growth of Central and East Pacific ENSO events. *Geophys. Res. Lett.*, **41**, 4027–4034, doi:10.1002/2014GL059997.

Wang, H., S.-P. Xie, H. Tokinaga, Q. Liu, and Y. Kosaka, 2016: Detecting cross-equatorial wind change as a fingerprint of climate response to anthropogenic aerosol forcing. *Geophys. Res.*

Lett., **43**, 3444–3450, doi:10.1002/2016GL068521.

Watanabe, M., H. Shiogama, H. Tatebe, M. Hayashi, M. Ishii, and M. Kimoto, 2014: Contribution of natural decadal variability to global warming acceleration and hiatus. *Nat. Clim. Chang.*, **4**, 893–897, doi:10.1038/nclimate2355.

Waugh, D. W., C. I. Garfinkel, L. M. Polvani, D. W. Waugh, C. I. Garfinkel, and L. M. Polvani, 2015: Drivers of the Recent Tropical Expansion in the Southern Hemisphere: Changing SSTs or Ozone Depletion? *J. Clim.*, **28**, 6581–6586, doi:10.1175/JCLI-D-15-0138.1.

Wittenberg, A. T., A. Rosati, N. C. Lau, and J. J. Ploshay, 2006: GFDL's CM2 global coupled climate models. Part III: Tropical Pacific climate and ENSO. *J. Clim.*, **19**, 698–722, doi:10.1175/JCLI3631.1.

WMO (World Meteorological Organization), 1957: Meteorology—a three-dimensional science. Second session of the Commission for Aerology. *WMO Bulletin,* **4**, 134–138.

Wu, S., L. Wu, Q. Liu, and S.-P. Xie, 2010: Development processes of the tropical pacific meridional mode. *Adv. Atmos. Sci.*, **27**, 95–99, doi:10.1007/s00376-009-8067-x.

Wunsch, C., and P. Heimbach, 2006: Estimated Decadal Changes in the North Atlantic Meridional Overturning Circulation and Heat Flux 1993–2004. *J. Phys. Oceanogr.*, doi:10.1175/jpo2957.1.

Xie, S.-P., 2004: The Shape of Continents, Air-Sea Interaction, and the Rising Branch of the Hadley Circulation. 121–152.

——, and S. G. H. Philander, 1994: A coupled ocean-atmosphere model of relevance to the ITCZ in the eastern Pacific. *Tellus A*, **46**, 340–350, doi:10.1034/j.1600-0870.1994.t01-1-00001.x.

——, and Y. Kosaka, 2017: What Caused the Global Surface Warming Hiatus of 1998-2013? *Curr. Clim. Chang. Reports*, **3**, 128–140, doi:10.1007/s40641-017-0063-0.

Xie, S. P., 1999: A dynamic ocean-atmosphere model of the tropical Atlantic decadal variability. *J. Clim.*, **12**, 64–70, doi:10.1175/1520-0442-12.1.64.

——, and J. A. Carton, 2004: Tropical atlantic variability: Patterns, mechanisms, and impacts. *Geophysical Monograph Series*.

Yang, C., B. S. Giese, and L. Wu, 2014: Ocean dynamics and tropical Pacific climate change in ocean reanalyses and coupled climate models. *J. Geophys. Res. Ocean.*, **119**, 7066–7077, doi:10.1002/2014JC009979.

Ye, J. S., 2014: Trend and variability of China's summer precipitation during 1955-2008. *Int. J. Climatol.*, **34**, 559–566, doi:10.1002/joc.3705.

You, Y., and J. C. Furtado, 2017: The role of South Pacific atmospheric variability in the

development of different types of ENSO. *Geophys. Res. Lett.*, **44**, 7438–7446, doi:10.1002/2017GL073475.

——, and ——, 2018: The South Pacific meridional mode and its role in tropical Pacific climate variability. *J. Clim.*, **31**, 10141–10163, doi:10.1175/JCLI-D-17-0860.1.

Yu, J. Y., and S. W. Fang, 2018: The Distinct Contributions of the Seasonal Footprinting and Charged-Discharged Mechanisms to ENSO Complexity. *Geophys. Res. Lett.*, **45**, 6611–6618, doi:10.1029/2018GL077664.

Zebiak, S. E., 1993: Air–Sea Interaction in the Equatorial Atlantic Region. *J. Clim.*, **6**, 1567–1586, doi:10.1175/1520-0442(1993)006<1567:AIITEA>2.0.CO;2.

Zhang, H., A. Clement, and P. N. DiNezio, 2014a: The south pacific meridional mode: A mechanism for ENSO-like variability. *J. Clim.*, **27**, 769–783, doi:10.1175/JCLI-D-13-00082.1.

——, C. Deser, A. Clement, and R. Tomas, 2014b: Equatorial signatures of the Pacific Meridional Modes: Dependence on mean climate state. *Geophys. Res. Lett.*, **41**, 568–574, doi:10.1002/2013GL058842.

Zhang, L., P. Chang, and L. Ji, 2009: Linking the Pacific meridional mode to ENSO: Coupled model analysis. *J. Clim.*, **22**, 3488–3505, doi:10.1175/2008JCLI2473.1.

Zhang, Y., S. P. Xie, Y. Kosaka, and J. C. Yang, 2018: Pacific decadal oscillation: Tropical Pacific forcing versus internal variability. *J. Clim.*, **31**, 8265–8279, doi:10.1175/JCLI-D-18-0164.1.